Y-branch Optical Wavelength Multi/Demultiplexers by Ion-exchange in Glass

by

Feng Xiang, M. Sc.

Electrical Engineering Department

McGill University, Montreal

February 1995

A thesis submitted to the Faculty of Graduate Studies and Research in partial fulfillment of the requirements for the degree of Doctor of Philosophy

National Library
of Canada

Acquisitions and
Bibliographic Services Branch

395 Wellington Street
Ottawa, Ontario
K1A 0N4

Bibliothèque nationale
du Canada

Direction des acquisitions et
des services bibliographiques

395, rue Wellington
Ottawa (Ontario)
K1A 0N4

Your file   Votre référence

Our file   Notre référence

ISBN 0-612-19697-6

To my wife, Minre Ba,
with love and gratitude

Abstract

A simple and accurate multisheet Brewster angle measurement technique has been developed to measure substrate indices. Both K$^+$ and Ag$^+$ ion-exchanged optical waveguides in glass substrates were characterized for infrared wavelengths $\lambda = 1.152$ and $1.523\mu m$. For the characterization of Ag$^+$ ion-exchange waveguide, the WKB method has been modified to handle the index truncation point at the waveguide boundary inside the substrate accurately. An explicit and stable finite-difference vector beam propagation method has also been developed for efficient numerical simulations of the guided-wave optical devices.

A modified Y-branch wavelength multi/demultiplexer (abbreviated as WDM) for $\lambda = 1.31$ and $1.55\mu m$ was designed and optimized by the beam propagation method (abbreviated as BPM). The device, made by K$^+$ ion-exchange in glass with a sputtered Al_2O_3 strip on one branch, can provide high extinction ratios and wide bandwidth. It was successfully fabricated. The measured results of over 20db extinction ratio agree well with the BPM design simulations. A new Y-branch WDM made by K$^+$ and Ag$^+$ ion-exchanges was proposed and fabricated. It eliminates a difficult fabrication process, involving an Al_2O_3 strip waveguide, and still provides the other merits of the first device. Its feasibility has been experimentally established. To simplify the fabrication process further, an asymmetric Mach-Zehnder WDM by one step ion-exchange for both two-wavelength and three-wavelength ($\lambda = 0.98\mu$m being the third wavelength) was proposed. The BPM simulations show some improvements in several aspects over other types of demultiplexers.

Résumé

Une technique simple et précise utilisant des angles Brewster "multisheet" a été dévelopée pour mesurer les indices des substrats. Des guides optiques fabriqués par l'échange-ionique de K^+ (potassium) ou Ag^+ (argent) dans un substrat de verre ont été caraterisés aux longueurs d'ondes 1.152μm et 1.523μm. Pour la caractérisation des guides optiques fabriqués par l'échange-ionique d'argent, la méthode WKB a été modifiée pour proprement rendre compte le point tronqué de l'indice à la limite du guide à l'intérieur du substrat. De plus, un version explicite et stable de la méthode FD-BPM ("Finite Difference Beam Propagation Method") a été employé pour les simulations efficaces et numériques des guides optiques.

Un guide d'onde du type "Y-branch" (abrégé WDM) a été utilisé et modifié pour réaliser un multi/démultiplexeur pour les longueurs d'ondes λ=1.31 et 1.55μm. Les multi/démultiplexeurs ont été conçus et optimisés utilisant la méthode BPM. L'appareil, qui a été fabriqué avec succès par l'échange-ionique K^+ dans un substrat de verre avec une bande de Al_2O_3 (oxide d'aluminum) postillonée sur une branche, peut donner des taux d'extinctions très hauts et des bandes de fréquences larges. Des nouveaux Y-branch WDM fabriqués par plusieurs échanges-ioniques de K^+ et Ag^+ ont été propsés. Le nouvel appareil possède un procéssus de fabrication facile, impliquant un guide optique de bandes Al_2O_3, et fournit les avantages et mérites de l'appareil précédant. Sa faisabilité a été établie expérimentalement. Pour simplifier le processus de fabrication d'avantage, un Mach-Zehnder WDM asymétrique fabriqué par échange-ionique d'une étape pour deux longueurs d'ondes et trois longueurs d'ondes (λ=0.98μm a été la troisiëime longueur d'onde) a été proposé. Les simulations BPM démontrent des améliorations dans plusieurs aspects par rappart aux autres types des démultiplexeurs.

Acknowledgements

I would like to thank my supervisor, Dr. Gar Lam Yip for his guidance and encouragement during the course of this research work.

I am also very grateful to Peter Noutsios who is currently proceeding toward his Ph. D degree. Fruitful discussions with him and his technical expertise greatly helped me to complete this work.

I would like to express my gratitude to the former postdoctoral fellows and graduate students of our Guided-Wave Photonics Laboratory, Dr. K. Kishioka, Dr. N. Goto, Messrs L. Babin, D. Ken, P. Allard, J.Y. Chen, J. Nikolopoulos, M.A. Sekerka-Bajbus, and L. Chen for their assistances and encouragement.

Finally, I would also like to thank Mr. Joseph Mui, our electronics technician for taking the pictures presented in this work, for me.

This research was supported by NSERC and McGill university through a strategic grant, operating grants, a McGill major fellowship, and a Principal's Dissertation fellowship.

List of Symbols

λ	wavelength
$\mathcal{E}$	time dependent vector of electric field
$\mathcal{H}$	time dependent vector of magnetic field
E	time independent vector of electric field
H	time independent vector of magnetic field
n(x,y,z)	refractive index
n_0	refractive index in free space
μ_0	permeability of vacuum
ε_0	permittivity of vacuum
ω	angular frequency
k_0	wave number in free space
β	propagation constant
n_e	effective index β/k_0
γ	transverse wave number
n_r	reference refractive index
k_r	reference wave number
Ψ	field component
ψ	field component after term $\exp(-j\beta z)$ (or $\exp(-jk_r z)$) dropped from Ψ
n_s	surface refractive index
n_b	substrate refractive index
n_c	cladding film refractive index
x_t	turning point in WKB method
f	cladding film thickness
A_i, B_i	Airy functions
Ω	phase integral
V	normalized freqency
b	normalized propagation constant
W	waveguide width
d, D	waveguide depths
s	waveguide (or branch) separation
θ	branch angle
D_e	diffusion coefficient
ER	extinction ratio
WDM	wavelength division multi/demultiplexer
DM	demultiplexer

WKB	Wentzel, Kramers, Brillouin, and Jeffrey method
MWKB	modified WKB method
EIM	effective index method
BPM	beam propagation method
D-F	Dufort-Frankel
FD	finite-difference
FD-BPM	finite-difference BPM
FFT-BPM	fast Fourier transform BPM
TBC	transparent boundary condition
M-Z	Mach-Zehnder interferometer

Contents

List of Figures

List of Tables

Chapter 1

Introduction

1.1 Historical Overview

In the early 1980's, the progress of single-mode optical fibers made a significant impact on lightwave communication systems due to their lower loss and dispersion than multi-mode fibers. There are two low loss wavelength windows of a glass fiber around $\lambda = 1.31\mu m$ and $1.55\mu m$ [1]. Before dispersion-shifted and dispersion-flattened fibers were developed in the middle of 1980's, most optical communication systems were designed for operation at $\lambda = 1.31\mu m$ window to take advantage of the zero dispersion of the standard step-index single-mode fibers at $\lambda = 1.3\mu m$ [2]. It was found out lately that the zero dispersion can be shifted to $\lambda = 1.55\mu m$ [3] if the core index profile of a single-mode fiber is properly designed. Further, with the development of dispersion-flattened single-mode fibers [4] the near-zero dispersion region covers both the low loss wavelength windows, which then permits the use of the wavelength-division multiplexing (WDM) technique for these two windows to effect wide band optical fiber communication systems.

Based on thin film technologies, integrated optics has been an active and rapidly progressing area of research since 1969 [5]. Like integrated electronics, integrated optics promises to provide miniaturized and interconnected signal-processing optical devices on a single substrate and has the potential to be mass produced. Usage of different kind of substrate determines the different technologies used in integrated optics (which can also be called "Guided-Wave Photonics", using the current terminology). One of such technologies is based on the use of glass as the substrate material. The importance of the glass based components is borne out by their compatibility with optical fibers, potentially low cost, low propagation losses, and the ease of their integration into an optical fiber communication system or sensor [6] [7].

Ion-exchange technique, which has been used for more than a century to produce tinted glass, has received increased attention in recent years as it improves surface-mechanical properties of glass and, more importantly, creates a waveguiding region in the glass. Since 1972 when Izawa and Nakagome [8] reported the first ion-exchanged waveguides by exchange of Tl^+ ions in a silicate glass containing oxides of sodium and potassium, significant progress has been made towards understanding the ion-exchange process and the role of the processing conditions on the propagation characteristics of the resulting waveguides. Various cation pairs and several different glass compositions and cation sources have been studied in the past two decades. Among them Ag^+-Na^+ [9] [10] and K^+-Na^+ [11] are considered to be prime candidates for making glass waveguides and devices. Findakly [12] and Ramaswamy [13] summarized most of the developments which occurred until 1983 and 1988 respectively. After the glass waveguide fabrication techniques (ion-beam milling, sputtering [14], photolithography, etc., besides the ion-exchange) become mature, many useful glass waveguide devices were proposed, designed, and implemented. Among them, the wavelength division multiplex (WDM) devices made on a glass substrate have been receiving considerable attention and much progress has been made.

1.2 Wavelength Division Multi/Demultiplexing Technique

In principle, optical wavelength multiplexing is quite similar to electrical multiplexing. However, much higher frequencies are employed in optical multiplexing. Wavelength division multi/demultiplexing (WDM) allows a fiber optical communication system to greatly enhance its channel capacity, by using several working wavelengths, each capable of carrying multiple channels. It increases the system capacity without much increase in cost [15]. The important performance figures of a WDM are extinction ratios (ER) which are the ratios between the power from a designed waveguide to the power leaked into the other waveguides, power loss, and channel separation. Several kinds of WDM devices have been proposed for different applications. Optical interference filters [16] provide high extinction ratios, low loss, and medium channel separation (30-100nm). Optical diffraction gratings [17] have high extinction ratios and small channel separation (1-40nm). Wavelength selective directional couplers [18] [19] [20] have low loss and large channel separation (40-200nm). X-branch two-mode interference WDMs [21] and [22] have high extinction ratios, large channel separation (40-200nm), and low loss. Asymmetric Y-branches which will be the main topic of this thesis promise to have high extinction ratios, large channel separation (>100nm), low loss, and short in length. The asymmetric Y-branch WDM made by K^+-ion exchange with one branch cladded by an Al_2O_3 strip was first proposed by Goto and Yip in [23] for $\lambda = 1.31\mu m$ and $\lambda = 1.55\mu m$. The measured extinction ratios of the first few fabricated devices were about 10db, far below the theoretical predictions.

The Y-branch is a very important structure in integrated optics. It can be either a power divider or a mode splitter depending on the branch angle and the branch asymmetry [24]. A wavelength multi/demultiplexer made by a Y-branch functions as a mode splitter. On the other hand, for a mode splitter to work as a wavelength multi/demultiplexer, not only the large branch asymmetry and small branch angle but also the branch waveguide mode dispersion and the waveguide material dispersion are the important facts that affect the device quality. To improve the initial design, a detailed study of this new kind of device is necessary, which has not been done, or at least has not been reported, according to our knowledge. From the basic device concept, the initial goal of this work is to modify the initial design, optimize, and fabricate the device.

Since the demultiplexers to be discussed in this work can intrinsically work also as multiplexers after the input and output of each individual are simply exchanged and the demultiplexing with high extinction ratios is more difficult to achieve, we will drop "multi" from "mutli/demultiplexer" and keep "demultiplexer" (DM) later on to emphasize our efforts in the optimum design and implementation of demultiplexers.

1.3 Original Contributions

The contributions of this work can be summarized as follows:

- characterizations of K^+ and Ag^+ ion-exchanged waveguides at infrared wavelengths [25] [26]
- development of a simple and accurate substrate index measurement method [27]
- modification in the WKB method for handling a waveguide index profile with truncation or discontinuities more accurately [28]
- development of an explicit and stable FD-BPM [29]
- modifications in the asymmetric Y-branch WDM with an Al_2O_3 strip load and also in its fabrication process which leads to much improved measured extinction

ratios [30] [31]

- proposal and fabrication of a new asymmetric Y-branch WDM made by a two-step (K^+ and Ag^+) ion-exchange in glass for $\lambda = 1.31\mu m$ and $\lambda = 1.55\mu m$ which offers an alternative fabrication process [32] [33]
- proposal and design of a two-wavelength WDM by cascading an asymmetric Y-branch with a Mach-Zehnder interferometer which requires only one-step ion-exchange and yet provides high extinction ratios [34]
- proposal and design of a three-wavelength (0.98, 1.31, 1.55 μ m) WDM by cascading two of the above proposed two-wavelength demultiplexers [35].

Bibliography

[1] S.S. Walker, "Rapid modeling and estimation of total spectral loss in optical fibers", J. Lightwave Technol. vol. LT-4, p.1126, 1986.

[2] F.P. Kapron and T.C. Olson, "Accurate specification of single-mode dispersion measurements", Tech. Digist, Symp. Opt. Fiber Measurements, NBC Special Publication 683 (Boulder, CO, October 1984), p.111.

[3] L.G. Cohen, C. Lin, and W.G. French, " Tailoring zero chromatic dispersion into the 1.5-1.6 μm low-loss spectral region of single-mode fibers", Electron. Lett., vol. 15, pp.334-335, 1979.

[4] L.G. Cohen, W.L. Mammel, and S.J. Jang, "Low-loss quadruple-clad single-mode lightguides with dispersion below 2ps/km-nm over the 1.28μm-1.65μm wavelength range", Electron. Lett., vol. 18, pp.1023-1024, 1982.

[5] S.E. Miller, "Integrated Optics: an introduction", Bell Sys. Tech. Journ., 48, pp.2059-2069, 1969.

[6] W.J. Tomlinson and C.A. Brackett, "Telecommunication applications of integrated optics and optoelectronics", Proc. IEEE, vol. 75, pp15 12-1523, 1987.

[7] S.R. Forrest, "Optoelectronic integrated circuits", Proc. IEEE, vol.75, pp.122-125, 1987.

[8] T. Izawa and H. Nakagome,"Optical waveguide formed by electrically induced migration of ions in glass plates", App. Phys. Lett., vol.21, p.584, 1972.

[9] G. Stewart, C.A. Millar, P.J.R. Laybourn, C.D.W. Wilkinson, and R.M. Delarue,"Planar optical waveguides formed by silver-ion migration in glass", IEEE J. of Quantum Electron., vol. QE-13, No.4, pp.192-200, 1977.

[10] G. Stewart and P.J.R. Laybourn, "Fabrication of ion-exchanged optical waveguides from dilute silver nitrate melts", IEEE J. of Quantum Electron., vol. QE-14, No.12, pp.930-934, 1978.

[11] G.L. Yip and J. Albert,"Characterization of planar optical waveguides by K^+-ion exchange in glass", Optics Lett., vol.10, No.3, pp.151-153, 1985.

[12] T. Finkadly,"Glass waveguides by ion exchange: a review", Opt. Eng., vol.24, pp.244-250, 1985.

[13] R.V. Ramaswamy and R. Srivastava,"Ion-exchanged glass waveguides: a review", IEEE J. of Lightwave Tech., vol. 6, No.6, pp.984-1001, 1988.

[14] H. Nishihara, M. Haruna, and T. Suhara,"Optical integrated circuits", New York, McGraw Hill, 1989.

[15] O.E. Delange,"Wideband optical communication systems: part 2-frequency division multiplexing", Proc. IEEE, vol.58, pp.1683-1690, 1970.

[16] H. Nishihara, M. Haruna, and T. Suhara,"Optical integrated circuits", New York, McGraw Hill, pp.265-273, 1989.

[17] T. Suhara and H. Nishihara,"Integrated optics components and devices using periodic structures", IEEE J. of Quantum Electron., vol.22, pp.847-865, 1986.

[18] M. Digonnet and H.J. Shaw,"Wavelength multiplexing in single-mode fiber couplers", Appl. Opt., vol.22, pp.484-491, 1983.

[19] R.C. Alferness and R.V. Schmidt, "Tunable optical waveguide directional coupler filter", Appl. Phys. Lett., vol.33, pp.161-163, 1978.

[20] H.C. Cheng and R.V. Ramaswamy, "A dual wavelength 1.3-1.55μm directional coupler wavelength division multi- demultiplexer", IEEE J. of Lightwave Tech., vol. 7 pp.766-776, 1989.

[21] Y Chung, J.Y. Yi, S.H. Kim, and S.S. Choi, "Analysis of a tunable multichannel two mode interference wavelength division multiplexer-demultiplexer", IEEE J. of Lightwave Tech., pp.766-776, vol. LT-7, 1989.

[22] L. J. M. Babin and G.L. Yip, "Design and realization of a widened X-branch demultiplexer at 1.31 and 1.55μm by K^+- Na^+ ion exchange in a glass substrate", IPR technical digest vol.3, pp. , 1994.

[23] N. Goto and G.L. Yip, "Y-branch wavelength multi- demultiplexer for $\lambda = 1.30\mu$m and $\lambda = 1.55\mu$m", Electronics Lett., vol.26, pp.102-103, 1990.

[24] W. K. Burns and A. F. Milton, "Mode conversion in planar dielectric separating waveguides", IEEE J. Quantum Electon., vol. QE-11, pp.32-39, 1975.

[25] G.L. Yip, K. Kishioka, F. Xiang, and J.Y. Chen, "Characterization of planar optical waveguides by K^+-ion exchange in glass at 1.152 and 1.523μm", SPIE conference proceedings, vol.1583 pp.14-18, 1991.

[26] F. Xiang, K.H. Chen, and G.L. Yip, "The application of an improved WKB method to the characterization of diluted silver ion-exchanged glass waveguides in the near infrared", SPIE conference proceedings, vol.1794, pp.40-47, 1992.

[27] F. Xiang and G.L. Yip, "Simple technique for determining substrate indices of isotropic materials by a multisheet Brewster angle measurement", Applied Optics, vol. 31, No. 36, pp.7570-7574, December 1992.

[28] F. Xiang and G.L. Yip,"A modified WKB method for the improved phase shift at a turning point", IEEE Journal of Lightwave Technology, vol. 12, pp.443-452, March, 1994.

[29] F. Xiang and G.L. Yip,"An Explicit and stable finite difference 2-D beam propagation method", IEEE Photon. Technol. Lett., vol.6, No.10, pp.1248-1250, 1994.

[30] F. Xiang, G.L. Yip, and N. Goto,"The analysis and design optimization of a Y-branch wavelength multi/demultiplexer for $\lambda = 1.31$ and $1.55\mu m$ by BPM", IOOC conference proceedings, paper Tu.PS1.6, 1991.

[31] F. Xiang and G.L. Yip,"An Al_2O_3 strip loaded Y-branch wavelength multi/ demultiplexer for $\lambda = 1.55$ and 1.31μm by K^+-Na^+ ion-exchange in glass", IPR technical digest, vol.3, pp.130-132, 1994.

[32] F. Xiang and G.L. Yip,"New Y-branch wavelength multi/demultiplexer by K^+ and Ag^+ ion exchange for $\lambda = 1.31$ and $1.55\mu m$", Electron. Lett., vol. 28, No. 24, pp.2262-2263, Nov. 1992.

[33] F. Xiang and G.L. Yip,"A Y-branch wavelength multi/demultiplexer by K^+ and Ag^+ ion-exchange for $\lambda = 1.31$ and 1.55μm -device fabrication and measurement results", GRIN conference proceedings, pp., 1994,

[34] F. Xiang and G.L. Yip,"Asymmetric Mach-Zehnder type wavelength demultiplexers", GRIN'93 conference proceedings, Paper C4, 1993.

[35] F. Xiang and G.L. Yip,"Three-Wavelength Mach-Zehnder demultiplexer", SPIE conference proceedings, 1994.

Chapter 2

Wave Theory and Numerical Methods for Optical Waveguides

The theory of guided-wave optics is based on the Maxwell's equations. Waveguides and devices made by ion-exchange in a glass substrate are mostly weakly guiding [1]. Some approximations can be applied which simplify the wave equations. In this Chapter, some powerful numerical methods will be presented to solve the wave equation, especially, the beam propagation method (abbreviated as BPM later) and the finite-difference beam propagation method (abbreviated as FD-BPM later). All the device designs and optimizations in this thesis work are mainly based on the methods and schemes presented here.

2.1 General Wave Equations

Maxwell's equations for source free, time dependent fields are

$$\nabla \times \mathcal{E} = -\mu_0 \frac{\partial \mathcal{H}}{\partial t} \tag{2.1}$$

$$\nabla \times \mathcal{H} = n^2 \varepsilon_0 \frac{\partial \mathcal{E}}{\partial t} \tag{2.2}$$

$$\nabla \cdot (n^2 \varepsilon_0 \mathcal{E}) = 0 \tag{2.3}$$

$$\nabla \cdot \mathcal{H} = 0 \tag{2.4}$$

where $\mathcal{E}$ and $\mathcal{H}$ are the time dependent vectors of electric and magnetic fields and n(x,y,z) is the medium refractive index. Representing both the field vectors in $\mathcal{E} = \mathbf{E}exp(j\omega t)$ and $\mathcal{H} = \mathbf{H}exp(j\omega t)$, the vector wave equations can be written as

$$\nabla^2 \mathbf{E} + \nabla[\frac{\mathbf{E} \cdot \nabla n^2(x,y,z)}{n^2(x,y,z)}] + k_0^2 n^2(x,y,z)\mathbf{E} = 0 \tag{2.5}$$

and

$$\nabla^2 \mathbf{H} + \frac{\nabla^2 n^2(x,y,z)}{n^2(x,y,z)} \times (\nabla \times \mathbf{H}) + k_0^2 n^2(x,y,z)\mathbf{H} = 0 \tag{2.6}$$

for both the electric field **E** and magnetic field **H**, respectively, where $k_0 = \omega\sqrt{\mu_0\varepsilon_0}$ the free space wavenumber. If the refractive index n(x,y,z) varies piecewise slowly with x, y, and z, the second terms in both Eqs.(2.5) and (2.6) can be neglected yielding the Helmholtz scalar wave equation

$$\nabla^2 \Psi + k_0^2 n^2(x,y,z)\Psi = 0. \tag{2.7}$$

where Ψ can be any of the six field components. The resulting fields will satisfy the boundary conditions for any index discontinuity.

2.1.1 The wave equation for a waveguide

For a waveguide, the index n is uniform along z and the travelling wave term exp(-jβz) is understood and can be dropped from the fields. The wave equation (2.7) can be reduced

$$\nabla_\perp^2 \psi + [k_0^2 n^2(x,y) - \beta^2]\psi = 0 \tag{2.8}$$

where $\nabla_\perp = \partial^2/\partial x^2 + \partial^2/\partial y^2$.

Consider a slab waveguide and assume that its index profile only varies in the x direction ($\partial/\partial y = 0$). We can classify into two kinds of mode solutions. One is the TE mode with

$$E_x = H_y = E_z = 0, \tag{2.9}$$

$$H_x = -\frac{\beta}{\omega\mu_0}E_y. \tag{2.10}$$

$$H_z = -\frac{j}{\omega\mu_0}\frac{\partial E_y}{\partial x} \tag{2.11}$$

and the other is the TM mode with

$$E_y = H_x = H_z = 0. \tag{2.12}$$

$$E_x = \frac{\beta^2}{\omega\varepsilon_0 n^2(x)}H_y. \tag{2.13}$$

$$E_z = \frac{j}{\omega\varepsilon_0 n^2(x)}\frac{\partial H_y}{\partial x}. \tag{2.14}$$

Eq.(2.8) is now simplified into

$$\frac{\partial^2\psi}{\partial x^2} + [k_0^2 n^2(x) - \beta^2]\psi = 0. \tag{2.15}$$

As shown in Eqs.(2.9-2.14), all the field components can be expressed by E_y for TE modes and by H_y for TM modes. Therefore, only one field component needs to be solved in Eq.(2.15). It is assumed in Eq.(2.15) that $\psi = E_y$ for TE modes or $\psi = H_y$ for TM modes.

2.1.2 The Fresnel wave equation

In most of guided-wave optical devices, the refractive index profiles of the waveguides are dependent on z. Here, we assume that the index n(y,z) be independent of x and slowly varies with y and z. This situation would correspond to the region inside a slab waveguide, infinite along the x-direction but bound along the y-direction (e.g. $y = \pm a$, a being a constant). If we express the field component Ψ in Eq.(2.7) as

$$\Psi(y,z) = \psi(y,z)exp(-jk_0 n_r z), \tag{2.16}$$

where n_r is a reference refractive index, substitution of Eq.(2.16) into Eq.(2.7) and use of $\partial/\partial x = 0$ lead to the following equation for the complex field amplitude

$$\frac{\partial^2\psi}{\partial z^2} - 2jk_0 n_r\frac{\partial\psi}{\partial z} + \frac{\partial^2\psi}{\partial y^2} + k_0^2(n^2 - n_r^2)\psi = 0. \tag{2.17}$$

Neglecting the first term in Eq.(2.17) gives the paraxial or Fresnel wave equation

$$-2jk_0 n_r \frac{\partial \psi}{\partial z} + \frac{\partial^2 \psi}{\partial y^2} + k_0^2(n^2 - n_r^2)\psi = 0. \tag{2.18}$$

Eq.(2.18) will be used in the beam propagation method (BPM) simulations of waveguide devices, employing the effective index method (EIM).

2.2 The WKB Approximation

This approximation, usually, associated with the names of Wentzel, Kramers, Brillouin, and Jeffrey (WKB, or WKBJ) is sometimes also known as the phase-integral method. A general discussion can be found in the book by Heading [2]. This method has been extensively used for calculating propagation constants of guided modes in optical waveguides [3]. Under the condition of slow index variations across the waveguide with the transverse waveguide dimensions much larger than a wavelength, this method gives a reasonable accuracy. The simplicity of this method is also an important fact and responsible for its wide use.

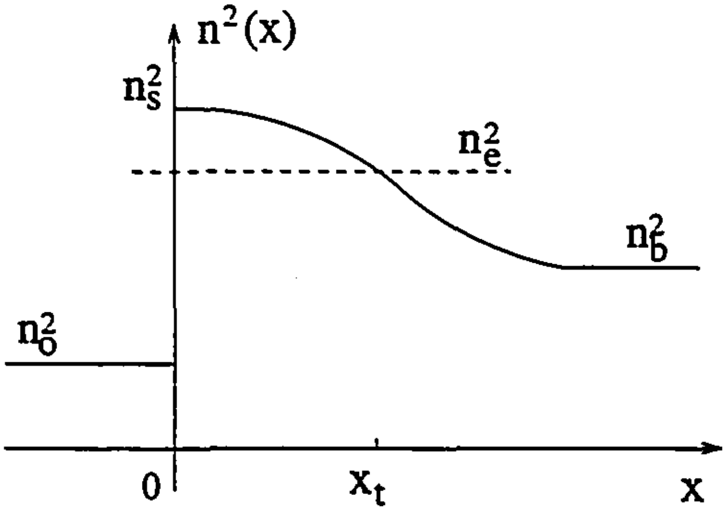

Figure 2.1: A refractive index profile $n^2(x)$ of a slab waveguide.

An ion-exchanged waveguide usually has a slow varying refractive index profile. Thus, for a piecewise slowly varying index profile, the Helmholtz scalar wave equation

(2.7) together with the boundary conditions at any index discontinuity is the equation to solve.

For an index profile such as that of a surface slab waveguide as shown in Fig.2.1, the WKB field solutions are given by [4]

$$\psi = A\ exp(xk_0P_{0^-}) \qquad (x < 0) \tag{2.19}$$

$$\psi \cong \frac{B}{\sqrt{Q}} cos[\int_x^{x_t} Qdx - \pi/4] \qquad (0 < x < x_t) \tag{2.20}$$

$$\psi \cong \frac{B}{2\sqrt{P}} exp[-\int_{x_t}^{x} Pdx] \qquad (x > x_t) \tag{2.21}$$

where A and B are both constants.

$$Q^2 = -P^2 = k_0^2(n^2(x) - n_e^2). \tag{2.22}$$

$$n_e = \beta/k_0 \tag{2.23}$$

is known as the effective index, and x_t is the turning point. At $x = x_t$, the Airy functions, A_i and B_i, solution of the scalar wave equation for a linear index profile [3], connect the fields given by Eq.(2.20) and Eq.(2.21) [4]. Matching the fields and their derivatives at x=0 leads to

$$A = \frac{B}{\sqrt{Q}} cos[\Omega - \pi/4], \tag{2.24}$$

and

$$\eta_1 Ak_0P_{0^-} = B\sqrt{Q} sin[\Omega - \pi/4], \tag{2.25}$$

where

$$\eta_1 = \begin{cases} 1 & \text{for TE modes} \\ n^2(0^+)/n^2(0^-) & \text{for TM modes,} \end{cases} \tag{2.26}$$

and

$$\Omega = \int_0^{x_t} Qdx. \tag{2.27}$$

The eigenvalue (or dispersion) equation for a surface waveguide is then given by

$$\int_0^{x_t} Qdx = M\pi + \pi/4 + tan^{-1}[\eta_1 \sqrt{\frac{n_e^2 - n_{0^-}^2}{n_{0^+}^2 - n_e^2}}]. \tag{2.28}$$

where Eq.(2.22) has been applied for P_0- and Q_0-, and the differentiation was not applied to Q in the denominator of Eq.(2.20) because $1/\sqrt{Q}$ is approximately constant near x=0. Eq.(2.28) is the same as that obtained by a rigorous application of the geometrical optics [5]. It will be used very frequently later on for K^+ ion-exchange surface waveguides.

2.3 The Dispersion Relation of a Cladded Surface Waveguide

Fig.2.2 shows an ion-exchanged surface slab waveguide with a cladded thin layer. The thin layer has a uniform refractive index $n_c > n_s$ and thickness f. For $n_c > n_s$, the waveguide can be approximately treated as a three-layer structure with a piece-wise uniform index profile (i.e. assume $n(x > 0) = n_s$. A more accurate representation can be found in [6]). For $n_c < n_s$, as is often the case in this thesis work, the dispersion equation (2.28) is no longer valid.

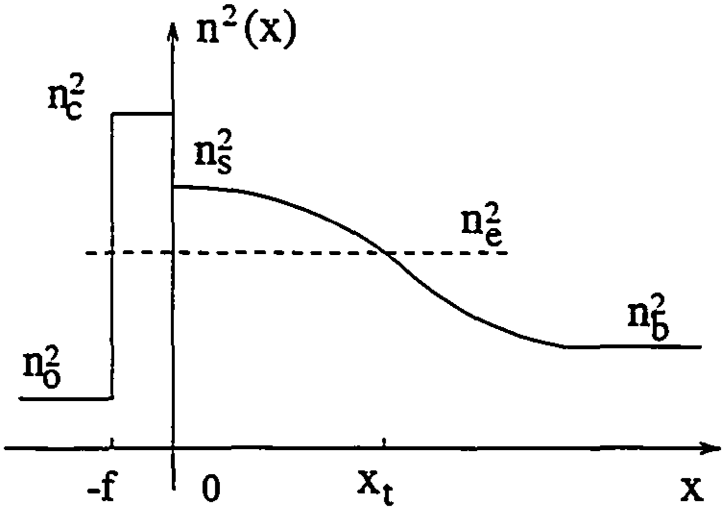

Figure 2.2: A refractive index profile $n^2(x)$ of a slab waveguide with a cladded thin layer.

There are two index discontinuities, at x=-f and x=0. Keeping the WKB field solution for the region with a graded index and sine and cosine functions for the cladding layer, we have the field solution of the Helmholtz wave equation (2.15) given by

$$v = A\ exp[k_0\sqrt{n_e^2 - n_0^2}(x - f)] \qquad (x < -f) \tag{2.29}$$

$$v = B\ sin(Q_c x) - C cos(Q_c x) \qquad (-f < x < 0) \tag{2.30}$$

$$v \cong \frac{B}{\sqrt{Q}} cos[\int_x^{x_t} Q dx - \pi/4] \qquad (0 < x < x_t) \tag{2.31}$$

$$v \cong \frac{B}{2\sqrt{P}} exp[-\int_{x_t}^{x} P dx] \qquad (x > x_t) \tag{2.32}$$

where $Q_c = k_0\sqrt{n_c^2 - n_e^2}$. Matching the fields and their derivatives at x=0 leads to

$$tan(\Omega - \pi/4) = \eta_1 \frac{Q_c}{Q_{0^-}} \frac{B}{C}. \tag{2.33}$$

Using the boundary conditions at x=-f, we have

$$\eta_2 \frac{k_0\sqrt{n_e^2 - n_0^2}}{Q_c} = \frac{B cos Q_c f + C sin Q_c f}{C cos Q_c f - B sin Q_c f} \tag{2.34}$$

where

$$\eta_2 = \begin{cases} 1 & \text{for TE modes} \\ n_c^2/n_0^2 & \text{for TM modes.} \end{cases} \tag{2.35}$$

Solving the ratio (B/C) from Eq.(2.34) and substituting it into Eq.(2.33) yield the dispersion relation for the waveguide as

$$tan(\Omega - \pi/4) = \eta_1 \sqrt{\frac{n_c^2 - n_e^2}{n_{0^-}^2 - n_e^2}} tan(\phi_c - k_0\sqrt{n_c^2 - n_e^2} f), \tag{2.36}$$

where

$$\phi_c = tan^{-1}[\eta_2 \sqrt{\frac{n_e^2 - n_0^2}{n_c^2 - n_e^2}}]. \tag{2.37}$$

ϕ_c is known as the half phase shift on the interface of air and cladding layer and Ω is given by Eq.(2.27). As we can see in Eq.(2.36), the dispersion relation can be simplified into a WKB eigenvalue equation if $n_c = n_{0^+} (= n_s)$.

2.4 A Modified WKB Method for a Truncated Index Profile

The refractive index profile of a Ag^+ ion-exchanged waveguide is mostly like the one shown in Fig. 2.3 with an index truncation at the internal edge of the waveguide due to the high mobility of Ag^+. This index truncation presents an index slope discontinuity at x=d. The half phase shift is no longer $\pi/4$ as it is for the index profile shown in Fig. 2.1 at the turning point x_t when x_t is near or at the truncation. Hence, the error in finding the effective index from the conventional WKB dispersion equation is large. It is desirable that the correction is made only in the phase shift while keeping the simplicity of the conventional WKB method.

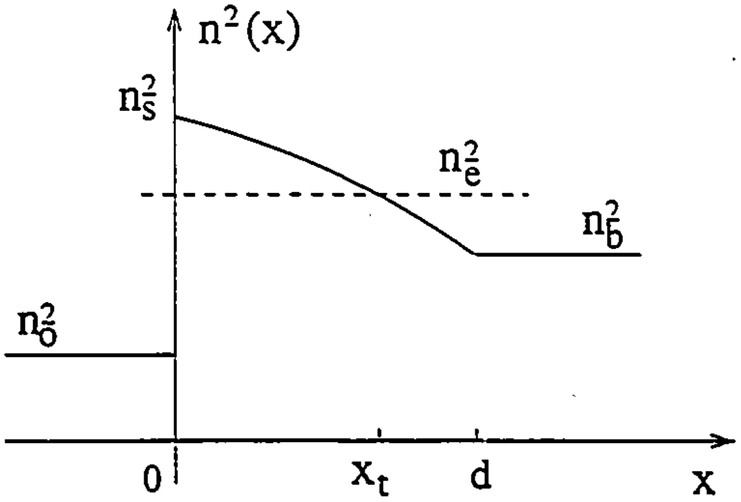

Figure 2.3: A refractive index profile $n^2(x)$ of a Ag^+ ion-exchanged slab waveguide with an index truncation at x=d and a turning point at x_t. The dashed line indicates the n_e^2 line.

A simple examination will show that the field solutions given by Eqs.(2.20) and (2.21) blow up at $x=x_t$ due to $Q^2=-P^2=0$. These expressions are actually the asymptotic forms of the Airy functions A_i and B_i [3], which are the solutions of the scalar wave equation for a linear index profile. At the turning point x_t, they act as connecting functions between the guided and evanescent regions. With the presence of an index slope discontinuity at x=d, the boundary conditions must still be satisfied. Thus, a field solution behaving well at the turning point has to be found.

By intuition, the Airy functions can be used as the field solution between (x_t, d) which connect the field solution in region (0, x_t) and behave well at x_t. Thus, an index profile linearization is needed as follows. A straight line, connecting $n^2(x_t)$ and $n^2(d^-)$, is used to approximate the true index profile, given by

$$n^2(x) = n^2(x_t) + (x - x_t)G/k_0^2, \quad x_t \leq x \leq d \tag{2.38}$$

where

$$G = k_0^2(n_e^2 - n^2(d^-))/(x_t - d). \tag{2.39}$$

It can be seen that the closer the turning point x_t is to the truncation, the closer the approximate linear index profile is to the true index profile. A good result can then be expected when x_t is close to the truncation. On the other hand, if x_t is away from the truncation, the field solutions outside of x_t will be less important to the phase shift at x_t. Thus, although the approximately linearized index profile deviates from the true index profile as x_t moves away from the truncation, the results on the propagation constant will still be good. The field solution of this linearized index profile is given by

$$\begin{aligned}
\psi &= A\ exp[k_0\sqrt{n_e^2 - n^2(0^-)}x], \qquad (x < 0) && (2.40)\\
\psi &\cong \frac{|G|^{1/6}}{\sqrt{\pi Q}}\{B sin[\int_x^{x_t} Q dx + \pi/4] \\
&\quad + C cos[\int_x^{x_t} Q dx + \pi/4]\}, \qquad (0 < x < x_t) && (2.41)\\
\psi &= BAi(\xi) + CBi(\xi), \qquad (x_t \leq x \leq d) && (2.42)\\
\psi &= E\ exp[-xk_0\sqrt{n_e^2 - n^2(d^+)}], \qquad (x > d) && (2.43)
\end{aligned}$$

where

$$\xi = -G^{1/3}(x - x_t), \tag{2.44}$$

A,B,C, and E are constants, G is given in Eq.(2.39), and Ai and Bi are the Airy functions [7]. If the Airy functions in Eq.(2.42) are replaced by their asymptotic forms, Eq.(2.41) can be deduced from Eq.(2.42) [Appendix 1]. Matching the fields and their derivatives at x=0 and x=d leads to the dispersion equation [Appendix 2]

$$\int_0^{x_t} Q dx = M\pi + tan^{-1}[\eta_1 \sqrt{\frac{n_e^2 - n^2(0^-)}{n^2(0^+) - n_e^2}}] + \phi_t \tag{2.45}$$

where the half phase shift at x_t is given by

$$\phi_t = \pi/4 + tan^{-1}[\frac{P_d A_i(\xi_d) - G^{1/3}A_i'(\xi_d)}{P_d B_i(\xi_d) - G^{1/3}B_i'(\xi_d)}], \tag{2.46}$$

and $P_d = P(x = d)$, and $\xi_d = \xi(x = d)$.

To demonstrate the improvement of this modified WKB method, a waveguide will be taken as an example which index profile is linear given by

$$n^2(x) = \begin{cases} n_0^2 & x < 0 \\ n_b^2 + (n_s^2 - n_b^2)(1 - x/d) & 0 < x \leq d \\ n_b^2 & d \leq x \end{cases} \tag{2.47}$$

The profile is truncated at x=d. Assume the index discontinuity at x=0 is large (strongly asymmetric). Then, the half-phase change at x=0 is $\pi/2$. Defining the normalized frequency V and the normalized propagation constant b as

$$V = kd\sqrt{n_s^2 - n_b^2} \qquad b = (n_e^2 - n_b^2)/(n_s^2 - n_b^2), \tag{2.48}$$

Since the index profile is strongly asymmetric and linear, the exact dispersion equation (the field vanishes at x=0) can be found in Eq.(4.42) in [3]. The curves of b-V and ϕ_t-b are presented in Figs.2.4 and 2.5 respectively for TE polarization.

The plots show substantial improvements especially in the single mode region and the modes near their cutoffs after the modified phase shift (2.46) has been adopted.

As shown in Fig.2.5, the differences of ϕ_t from $\pi/4$ are not negligible especially for lower order modes when the modes are near their cutoffs (b→ 0). Similar results can also be found in Fig.2 of [8].

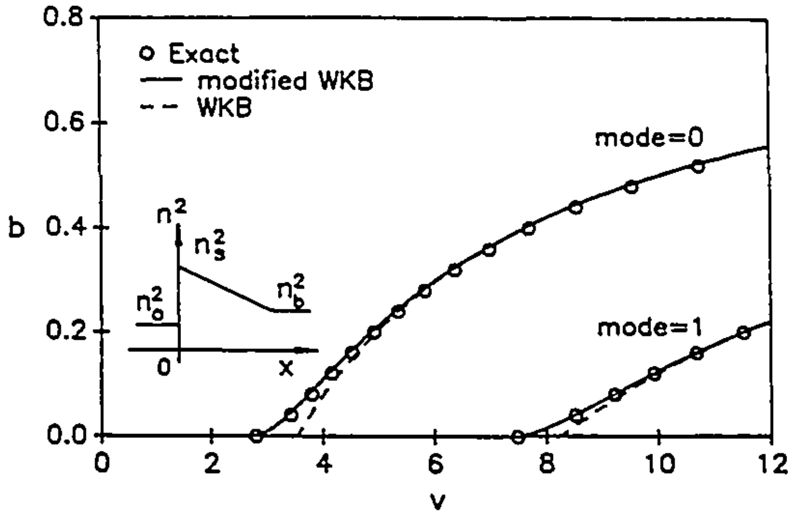

Figure 2.4: Normalized b-V plots for a strongly asymmetric linear profile.

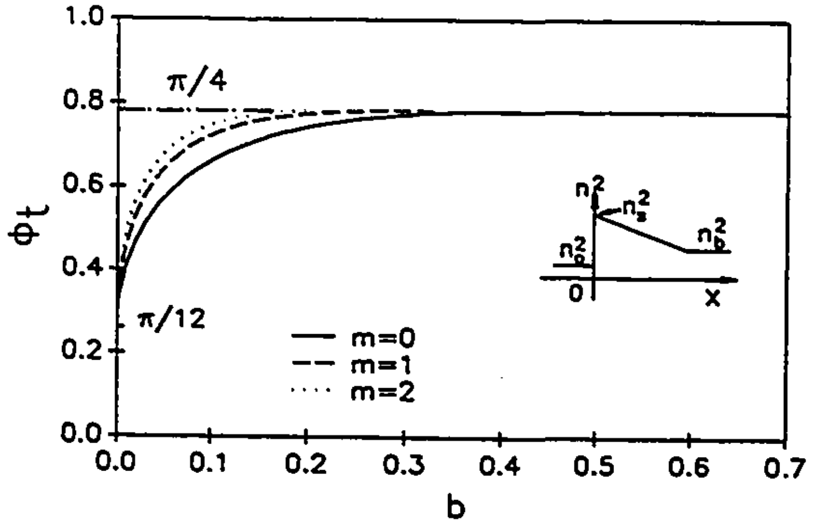

Figure 2.5: Phase shift dependence on the propagation constant. ϕ_t is one half of the phase shift at x_t.

The detail of MWKB method is presented in [4]. The modified half phase shift given in Eq.(2.46) is the special case of a truncated surface waveguide which will be applied to Ag^+ ion-exchanged waveguide in our devices later on.

2.5 Beam Propagation Method

The beam propagation method (BPM) basically consists of propagating the input beam over a small distance through a homogenous space and then correcting for the refractive-index variations seen by this beam during the propagation step [9]. The correction simply amounts to the application of the lens law. The result provides a detailed and accurate description of the propagation field. The method is suitable for a device with a complicated refractive-index profile and yields solutions including not only high-order guided modes but also radiation modes (loss).

The method is applicable to the case of weak guidance governed by the scalar Helmholtz wave equation. Numerically, it is based on the split operator and discrete Fourier transform techniques. Although the method generally also works for three-dimensional problems, it will be only used to solve two-dimensional problem ($\partial/\partial x = 0$) in this thesis work to save the computing time.

2.5.1 Theory and formula

Taking the Fresnel wave equation (2.18) as an ordinary differential equation with respect to z and letting ψ_n be the complete solution to the wave equation at $z = z_n$, we can have the solution at $z_{n+1} = z_n + \Delta z$ in terms of ψ_n given by [10]

$$\psi_{n+1} = exp[-\frac{j}{2k_r}\Delta z(\frac{\partial^2}{\partial y^2} + \chi)]\psi_n \tag{2.49}$$

where

$$\chi = \frac{k_r^2}{\Delta z}\int_{z_n}^{z_{n+1}}[\frac{n^2(y,z)}{n_r^2} - 1]dz, \tag{2.50}$$

$k_r = k_0 n_r$, and n_r is a reference index. In general, the operator $\partial^2/\partial y^2$ and χ do not commute. It is clearly shown in [10], however, that for any analytic function χ i.e. one that can be represented as a Taylor series in z, the solution (2.49) can be replaced with a second-order accuracy by one involving the symmetrized split operator form

$$\psi_{n+1} = exp(-\frac{j}{4k_r}\Delta z\frac{\partial^2}{\partial y^2})exp(-\frac{j}{2k_r}\Delta z\chi)exp(-\frac{j}{4k_r}\Delta z\frac{\partial^2}{\partial y^2})\psi_n \qquad (2.51)$$

The algorithm for propagating the field over a distance Δz thus consists of incrementing the phase in accordance with a non-uniform medium index changes, followed by a uniform medium (n_r) propagation of the resulting field over a distance Δz, i.e. solving the equation

$$2jk_r\frac{\partial\psi}{\partial z} = \frac{\partial^2\psi}{\partial y^2}. \qquad (2.52)$$

In order to introduce the symmetrization, it is only necessary to introduce the procedure by a step of propagation over a uniform medium (n_r) from z=0 to z=$\Delta z/2$.

In the phase correction term given by $-\Delta z\chi/2k_r$ through a distance Δz, n=n(y,z) can be a complicated index profile for which the accuracy still holds as long as n changes slowly. This is one of the reasons why the BPM is powerful.

The numerical solution of Eq.(2.52) is obtained by expanding $\psi(y,z)$ in a finite Fourier series

$$\psi(y,z) = \sum_{m=1-M/2}^{M/2} \psi_m(z)exp[j2\pi\frac{my}{L}] \qquad (2.53)$$

which exhibits periodicity over a span of $L = M\Delta y$ in the y-direction. On substituting expression (2.53) into Eq.(2.52), the following expression for $\psi_m(\Delta z)$ is obtained [10].

$$\psi_m(\Delta z) = \psi_m(0)exp[\frac{j}{2k_r}(\frac{2\pi}{L})^2 m^2\Delta z]. \qquad (2.54)$$

The initial values $\psi_m(0)$ are evaluated numerically by an application of the discrete Fourier transform (DFT)

$$\psi_m(0) = \sum_{u=0}^{M-1} \psi_m(m\Delta y, z=0)exp[-j2\pi u\frac{m}{M}]. \qquad (2.55)$$

The numerical evaluation of Eq.(2.55) is done with the fast Fourier transform (FFT) algorithm.

Eq.(2.53) in conjunction with Eqs.(2.54) and (2.55) provides an exact solution to Eq.(2.52) for an initial field of limited spectral bandwidth. In accordance with Eq.(2.49) the propagation step is followed by multiplication of ψ by the phase correcting factor $exp(-j\Delta z\chi/2k_r)$, hence

$$\tilde{\psi}(y, \Delta z) = exp[-j\Delta z\chi/2k_r]\psi(y, \Delta z). \tag{2.56}$$

If the spectrum of $\tilde{\psi}$ remains finite and is bounded by that of ψ before the phase correction, the Fourier coefficients $\psi_m^D(\Delta z)$ of ψ in Eq.(2.53) can be evaluated exactly in terms of the sampled values on the computation grid points. Then, the next Δz propagation can be similarly followed. In the computation, every propagation by Δz consists of a FFT converting the field $\psi(y, z)$ into its space spectrum $\psi_m(z)$ governed by Eq.(2.55), Δz propagation through a uniform medium (n_r) governed by Eq.(2.54), and an inverse FFT converting the space spectrum back to the field $\psi(y, z + \Delta z)$. However, to start the computation, the first step is a half-step propagation ($\Delta z/2$). Then, it is followed by a lens operator (multiplied by a factor $exp(-j\Delta z\chi/2k_r)$). To get the true field values at $z = \Delta z$, a half propagation step is required after the phase correction. Then, another half-step propagation is needed to continue the computation. These two half-steps can be put together as one step (Δz) to save the computation time if there is no need of comuputing the true field at that point (Δz here) which is often the case unless where the field values are needed for plotting and monitary purposes.

2.5.2 Absorber boundary

If there exists a radiation loss in the problem we are studying, the radiation field will pass through the edges of the computational window along the y-axis. Since we have used the finite Fourier transform, this radiation field will, in the succeeding steps, be folded back to the opposite edges of the window, causing high- frequency numerical instabilities. In order to avoid this problem, we must absorb the field at the edges of the window, for example, by setting the electric field at the first and last few window grid points to zero or by inserting a large negative imaginary component in the refractive index at these points. But it is found that a large amplitude high-frequency ripple is implanted on the electric field inside the window [10]. A suitable absorber in the computation can be obtained if the electric field is multiplied by the following function

$$Absorb(y) = \begin{cases} 1, & \mid y \mid < \mid y_a \mid \\ \frac{1}{2}\{1 + cos^{\gamma}[\pi(y - y_b)/(y_a - y_b)]\}, & \mid y_a \mid < \mid y \mid < \mid y_b \mid \\ 0, & \mid y_b \mid < \mid y \mid < \mid y_R \mid \end{cases} \tag{2.57}$$

where y_R is the coordinate of the grid boundary, y_a denotes the inner edge of the absorber, y_b is the outer edge. The parameters γ, y_a, and y_b are chosen empirically for each problem's configuration and step size to ensure that the field is absorbed gradually over a sufficiently wide region $\mid y_a \mid < \mid y \mid < \mid y_b \mid$.

The step size Δz is an important parameter in the BPM. An exclusive discussion is given in [10]. The choice of Δz is dependent on the refractive index profile. Here, we give the range of Δz which is often used in integrated optics

$$0.1\mu m < \Delta z < 10\mu m. \tag{2.58}$$

2.6 Explicit and Stable Finite-Difference Beam Propagation Method

Recently, the beam propagation method (BPM) has been significantly improved after finite-difference (FD) schemes replaced the FFT scheme. There are two kinds of commonly used finite-difference schemes. One is the Crank-Nicolson method [11] in which a tridiagonal matrix has to be found followed by finding its inverse matrix for each propagation step. This scheme is stable and accurate. For a weakly guiding structure, a large step-size can be used with a reasonable accuracy. However, for a three-dimensional problem, the matrix becomes complicated. It will not be easy to find the inverse matrix. The other is simply based on an explicit (centered forward-difference) method [12]. The latter method gives a very simple formulation for each propagation step, which is good for solving a three-dimensional problem. However, its stability is critical. In order to keep the scheme stable, the propagation step has to be less than a certain size which usually must be very small and, in some cases, too small to be applicable.

In this section, we will present a different finite-difference scheme, based on the DuFort-Frankel method [13] which is explicit and stable [14]. It has the merits of both the above-mentioned methods. The scheme is not yet popular and not even mentioned in some mathematical books because it introduces an extra error proportional to the second-order derivative of the field with respect to the propagation direction. If the structure is weakly guiding as most cases are in integrated optical devices, this second-order derivative is small and can be neglected as usually done in deriving the paraxial wave equation. Since the scheme is explicit, it is particularly useful for three-dimensional problems. The new scheme will be discussed only for a two-dimensional structure in this section, assuming $\partial/\partial x = 0$. Please see [15] for solving a three-dimensional problem by the new scheme.

2.6.1 Conventional explicit FD-BPM

Expressing the Eq.(2.17) in finite difference by [16]

$$\frac{\partial \psi_{m,n}}{\partial z} \approx \frac{\psi_{m,n+1} - \psi_{m,n-1}}{2\Delta z} - \frac{\Delta z^2}{6}\frac{\partial^3 \psi_{m,n}}{\partial z^3}, \tag{2.59}$$

and

$$\frac{\partial^2 \psi_{m,n}}{\partial y^2} \approx \frac{\psi_{m+1,n} - 2\psi_{m,n} + \psi_{m-1,n}}{\Delta y^2} - \frac{\Delta y^2}{12}\frac{\partial^4 \psi_{m,n}}{\partial y^4}, \tag{2.60}$$

we have the finite-difference wave equation for TE modes given by [Appendix 3]

$$\psi_{m,n+1} = \psi_{m,n-1} + r(\psi_{m+1,n} + \psi_{m-1,n}) - (1-\alpha)r(2\psi_{m,n}) + Er1, \tag{2.61}$$

where

$$r = \frac{-j\Delta z}{n_r k_0 \Delta y^2}, \tag{2.62}$$

$$\alpha = \frac{1}{2}\Delta y^2 k_0^2 (n^2 - n_r^2) \tag{2.63}$$

and

$$Er1 = r\Delta y^2 \frac{\partial^2 \psi_{m,n}}{\partial z^2} + \text{higher order terms.} \tag{2.64}$$

$\psi_{m,n}$ represents the field value $\psi(y = m\Delta y, z = n\Delta z)$. Thus, knowing ψ at z_{n-1} and z_n, $\psi(z_{n+1})$ can be obtained by Eq.(2.61), which is like a beam propagating along z. For TM modes, Eq.(2.60) should be replaced by

$$\frac{\partial^2 \psi_{m,n}}{\partial y^2} \approx \frac{T_{m+1,n}\psi_{m+1,n} - \xi_{m,n} 2\psi_{m,n} + T_{m-1,n}\psi_{m-1,n}}{\Delta y^2} - \frac{\Delta y^2}{12}\frac{\partial^4 \psi_{m,n}}{\partial y^4}, \tag{2.65}$$

where

$$\xi_{m,n} = 1 - \frac{1}{2}R_{m+1,n} - \frac{1}{2}R_{m-1,n}, \tag{2.66}$$

$$T_{m\pm 1,n} = \frac{2n_{m\pm 1,n}^2}{n_{m\pm 1,n}^2 + n_{m,n}^2}, \tag{2.67}$$

and

$$R_{m\pm 1,n} = \frac{n_{m\pm 1,n}^2 - n_{m,n}^2}{n_{m\pm 1,n}^2 + n_{m,n}^2}, \tag{2.68}$$

after the boundary conditions are enforced at index discontinuities [17] [18]. Then, the finite-difference wave equation for TM modes is given by

$$\psi_{m,n+1} = \psi_{m,n-1} + r(T_{m+1,n}\psi_{m+1,n} + T_{m-1,n}\psi_{m-1,n}) - (\xi_{m,n} - \alpha)r(2\psi_{m,n}) + Er1. \tag{2.69}$$

The derivation of the above equation is similar to that of Eq.(2.61). Neglecting the error term Er1 in Eqs.(2.61) and (2.69) leads to the conventional explicit FD-BPM. The condition of numerical stability of the scheme is given by [12]

$$\Delta z < n_r k_0 \Delta y^2/(2 - \alpha) \tag{2.70}$$

which is usually very small. For the example of a directional coupler as shown in Fig.2.7, where $n_1 = 1.5$, $n_2 = 1.3$, $W = 0.5\mu m$, and $S = 1.0\mu m$, the step size

$\Delta z < 0.0072\mu m$ is the condition for the numerical stability when $\Delta y = 0.05\mu m$, wavelength $\lambda = 1.5\mu$m, and the reference index $n_r = 1.372$ are chosen from the average effective index of the first and second order local modes. Since Eq.(2.61) or (2.69) is explicit, it is known as the conventional explicit FD-BPM.

2.6.2 Dufort-Frankel FD solutions

The relation between the second-order derivative of field ψ and its centered finite-difference expression with respect to the propagation direction z is given by

$$\frac{\partial^2 \psi_{m,n}}{\partial z^2} \approx \frac{\psi_{m,n+1} - 2\psi_{m,n} + \psi_{m,n-1}}{\Delta z^2} - \frac{\Delta z^2}{12}\frac{\partial^4 \psi_{m,n}}{\partial z^4} \tag{2.71}$$

Solving for $2\psi_{m,n}$ in Eq.(2.71) we have

$$2\psi_{m,n} \approx \psi_{m,n+1} + \psi_{m,n-1} - \Delta z^2 \frac{\partial^2 \psi_{m,n}}{\partial z^2} - \frac{\Delta z^4}{12}\frac{\partial^4 \psi_{m,n}}{\partial z^4} \tag{2.72}$$

Neglecting terms with orders higher than Δz^2, we have

$$\psi_{m,n} \approx \frac{1}{2}(\psi_{m,n+1} + \psi_{m,n-1}). \tag{2.73}$$

This is the so-called Dufort-Frankel approximation. Replacing $2\psi_{m,n}$ in Eqs.(2.61) and (2.69) and solving for field $\psi_{m,n+1}$, we obtain

$$\psi_{m,n+1} = \frac{1 - r(1-\alpha)}{1 + r(1-\alpha)}\psi_{m,n-1} + \frac{r}{1 + r(1-\alpha)}(\psi_{m+1,n} + \psi_{m-1,n}) + Er2 \tag{2.74}$$

for TE modes and

$$\psi_{m,n+1} = \frac{1 - r(\xi_{m,n}-\alpha)}{1 + r(\xi_{m,n}-\alpha)}\psi_{m,n-1} + \frac{r(T_{m+1,n}\psi_{m+1,n} + T_{m-1,n}\psi_{m-1,n})}{1 + r(\xi_{m,n}-\alpha)} + Er2 \tag{2.75}$$

for TM modes, where

$$Er2 \approx \frac{r\Delta y^2}{1 + r(1-\alpha)}\frac{\partial^2 \psi_{m,n}}{\partial z^2}[1 + (1-\alpha)\frac{\Delta z^2}{\Delta y^2}] + \text{ higher order terms,} \tag{2.76}$$

where the differences in Er2 due to the polarizations have been neglected in Eq.(2.76). Neglecting the error term Er2 in Eqs.(2.74) and (2.75) results in the Dufort-Frankel FD-BPM solutions. In comparing with Er1 in Eq.(2.64), the Dufort-Frankel

(D-F) solution has an error not only due to the Fresnel approximation (the first term in the square bracket of Eq.(2.76) but also due to the neglect of the term in the order of $(\Delta z/\Delta y)^2\partial^2\phi_{m,n}/\partial z^2$ (the second term in the square bracket of Eq.(2.76) and α assumed small). It can be seen that if $\Delta z \le \Delta y$, this extra error will be equivalent to the error of neglecting $\partial^2\phi/\partial z^2$ in deriving the Fresnel equation or less.

It can be shown that the D-F solutions are von Neumann stable [Appendix 4] if the refractive index n(y,z) is real and

$$\Delta z \le \frac{n_r}{\sqrt{n^2 - n_r^2}}\Delta y \quad \text{where } n(y,z) > n_r \quad . \tag{2.77}$$

For $n(y,z) \le n_r$, the scheme is unconditionally stable provided that n(y,z) is real. It is worth to point out that the condition of (2.77) can always be satisfied if the reference index n_r is chosen to be or close to the maximum of $n(y,z)$.

2.6.3 Leap-frog ordering of calculation

Taking a close look at Eqs.(2.74) and (2.75), it is not difficult to find that $\psi_{m,n}$ with an even number $m = 2,4,\cdots$, are independent of the previous field values $\psi_{m,n-1}$ with an even number $m = 2,4,\cdots$, and the next previous field values $\psi_{m,n-2}$ with an odd number $m = 1,3,\cdots$. Thus, we can have two independent sets of solutions indicated by circles and solid dots respectively in Fig.2.6. Usually, one set is enough, for example, the circles. Thus, the field values at the solid dots are not needed and the amount of computation time can be reduced by half without decreasing the accuracy. This is called the leap-frog ordering of calculation [13].

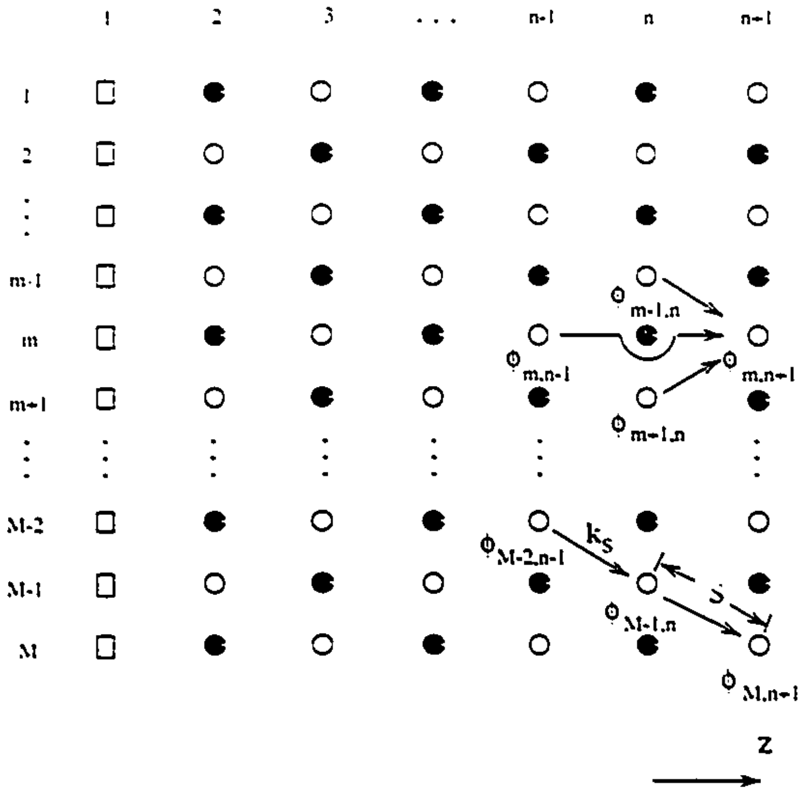

Figure 2.6: Leap-frog ordering of calculation, where the squares indicate the points having initial input field values.

2.6.4 Transparent boundary condition

The transparent boundary condition(TBC) can still be used in the present new scheme. However, the application of the conventional TBC as given in [19] may lead to numierical instability, manifested in the occurrence of parasitic waves at the boundaries, which will spread towards the center after further propagation steps. To eliminate this problem and to adapt to the data obtained at the diagonal grid points in a leap-frog scheme as outlined above, the following modified TBC has been found, after several other trials, to yield numerical stability.

$$v_{M,n-1} = v_{M-1,n}^2 / v_{M-2,n-1}. \tag{2.78}$$

which is a modified form of the conventional TBC

$$v_{M,n+1} / v_{M-1,n} = v_{M-1,n+1} / v_{M-2,n} (\approx v_{M-1,n} / v_{M-2,n-1}). \tag{2.79}$$

To ensure outgoing waves only, the imaginary part of $log_e(v_{M-1,n}/v_{M-2,n-1})$ [N.B. $v_{M-1,n} = v_{M-2,n-1} exp(-jk_s s)$. k_s is the wavenumber along the diagonal direction.] should be negative.

2.6.5 Example and comparisons

The slab waveguide directional coupler as shown in Fig.2.7 has been taken as an example to illustrate the new scheme.

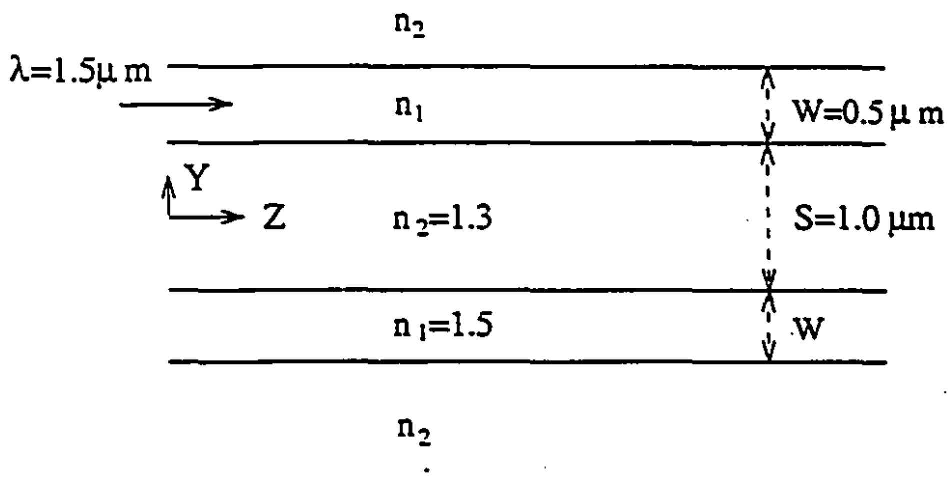

Figure 2.7: A schematic diagram of a parallel slab waveguide coupler.

The wavelength λ is $1.5\mu m$ and the window size is $10\mu m$. Thus, Eq.(2.77) gives $\Delta z \leq 2.3\Delta y$ for stability. Assume $\Delta y = 0.05\mu m$. In the new scheme, $\Delta z \leq$

$\Delta y = 0.05\mu m$ is required to keep the extra error term insignificant and hence the results equally accurate, which is about 7 times of the step-size of Eq.(2.70) in the conventional explicit scheme.

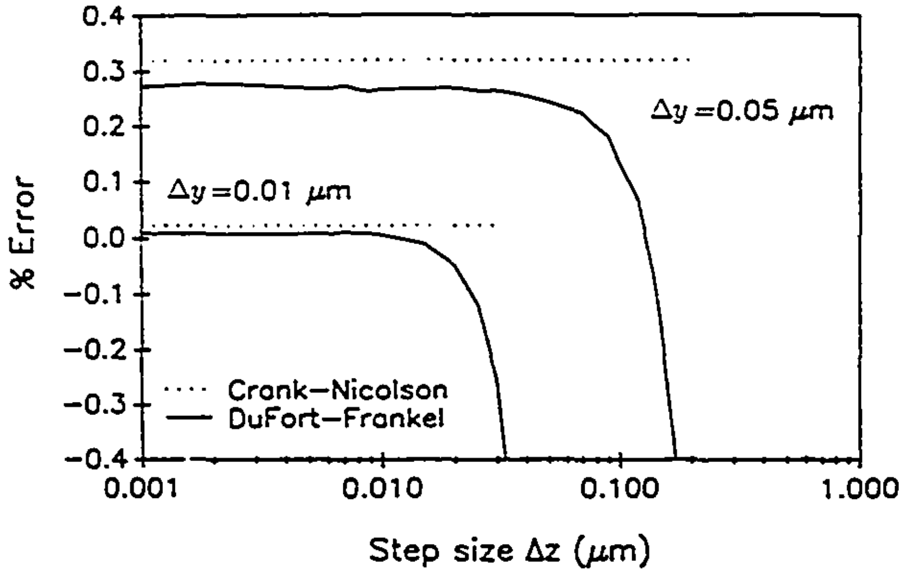

Figure 2.8: Fercentage errors in the coupling length versus the step-size Δz. The other parameters are given in the text.

Fig.2.8 shows curves of the percentage error for the coupling length versus the propagation step-size Δz for TE polarization. It can be clearly seen that the error is mainly dependent on Δy when $\Delta z \leq \Delta y$ and the error increases dramatically for $\Delta z \geq 3\Delta y$. However, it is still reasonable for $\Delta z = 2\Delta y$ which is 14 times that allowed in the conventional explicit method. Although the propagation step-size is restricted by the stability requirement Eq.(2.77), the extra error term $(\Delta z/\Delta y)^2\partial^2\phi_{m,n}/\partial z^2$ is the main reason for limiting the step-size according to our experiences. The coefficients in front of the field values on the right side of Eq.(2.74) are slightly more complicated than those in the conventional explicit scheme Eq.(2.61). Without worrying about this minor difference, the new scheme with the leap-frog ordering technique can be potentially about 27 times faster than the conventional explicit scheme in computation for this particular example if $\Delta z = 2\Delta y$ is taken as the step size. Comparing with the error in the Crank-Nicolson method, some improvement is shown in Fig.2.8 which may be due to the use of the new transparent boundary condition Eq.(2.78). Letting $\Delta y = 0.01\mu m$ and hence $\Delta z = 2\Delta y = 0.02\mu m$ in both the new scheme and the Crank-Nicolson scheme, we performed the computations for the coupler with $40\mu m$ in length on a SUN SPARC station. The CPU times are 143 seconds and 730 seconds for the new and Crank-Nicolson schemes respectively, keeping it in mind that the step-size Δz in the Crank-Nicolson scheme is not subjected to the same limitation of $\Delta z = 0.02\mu$m.

The new scheme is explicit and stable. It can be easily implemented into a three-dimension FD-BPM [15]. The propagation step-size can be at least the size of the transverse grid, which is much larger than that in the conventional explicit scheme. With the leap-frog ordering technique, the new scheme can be more efficient. The new scheme was very recently developed. Only a newly proposed three-wavelength demultiplexer (see Chapter 7) has benefited from the higher numerical efficiency. Fortunately, other devices are shorter and narrower and, hence, can be adequately treated with the FFT-BPM.

2.7 Effective Index Modeling

So far the methods we presented are all for two-dimension problems. In this section, we will present the well known effective index method to simplify a three-dimensional problem to two two-dimensional problems [20] which, in turn, can be solved by the methods introduced in previous sections. Since the refractive index profiles of ion-exchanged surface glass waveguides are slowly varying, the scalar wave equation Eq.(2.7) can be used and a reasonable assumption $\Psi(x, y, z) = X(x)\Phi(y, z)$

can be adopted. This assumption transforms the scalar wave equation into

$$\frac{1}{X(x)}\frac{\partial^2 X(x)}{\partial x^2}+\frac{1}{\Phi(y,z)}[\frac{\partial^2}{\partial y^2}+\frac{\partial^2}{\partial z^2}]\Phi(y,z)+k_0^2[n^2(x,y,z)-n_{eff}^2(y,z)]+k_0^2 n_{eff}^2(y,z)=0 \tag{2.80}$$

where $n_{eff}(y,z)$ is the lateral effective index profile function and will be discussed more later. Eq.(2.80) can be divided into two equations

$$\frac{\partial^2 X(x)}{\partial x^2}+k_0^2[n^2(x,y,z)-n_{eff}^2(y,z)]X(x)=0 \tag{2.81}$$

for the depth problem along x and

$$\frac{\partial^2\Phi(y,z)}{\partial y^2}+\frac{\partial^2\Phi(y,z)}{\partial z^2}+k_0^2 n_{eff}^2(y,z)\Phi(y,z)=0. \tag{2.82}$$

for the lateral problem along y. If a channel waveguide is considered, the refractive index is uniform along z. Then, the substitution of $\Phi(y,z)=\psi(y)exp(-j\beta z)$ into Eq.(2.82) leads to

$$\frac{\partial^2\phi(y)}{\partial y^2}++k_0^2[n_{eff}^2(y)-n_e^2]\Phi(y)=0. \tag{2.83}$$

where $n_e=\beta/k_0$ as the effective index of the propagation constant. If the index slowly varies along z, the expression $\Phi(y,z)=\psi(y,z)exp(-jn_r z)$ should be used to obtain the Fresnel wave equation after $\partial^2\phi/\partial z^2$ has been neglected

$$-2jk_0 n_r\frac{\partial\psi}{\partial z}+\frac{\partial^2\psi}{\partial y^2}+k_0^2(n_{eff}^2(y,z)-n_r^2)\psi=0. \tag{2.84}$$

where n_r is the reference index. To discuss the significance of the effective index modelling, let us take the example of an ion-exchanged channel waveguide which has an index profile shown in Fig.2.9a. The waveguide has a width of w. The index is assumed piecewise constant inside and outside the waveguide (i.e. step-index) with respect to y and is graded along x ($x>0$). Solving Eq.(2.81) for both inside and outside the waveguide by the WKB method, we can obtain the lateral effective index profile $n_{eff}(y)$ as shown in Fig.2.9c. Thus, with the new n_{eff}, solving Eq.(2.83) is equivalent to solving a three-layer slab waveguide. For a waveguide device, the

Fresnel wave equation (2.84) is to be solved by the BPM since $n_{eff}(y, z)$ obtained from Eq.(2.81) is dependent on z.

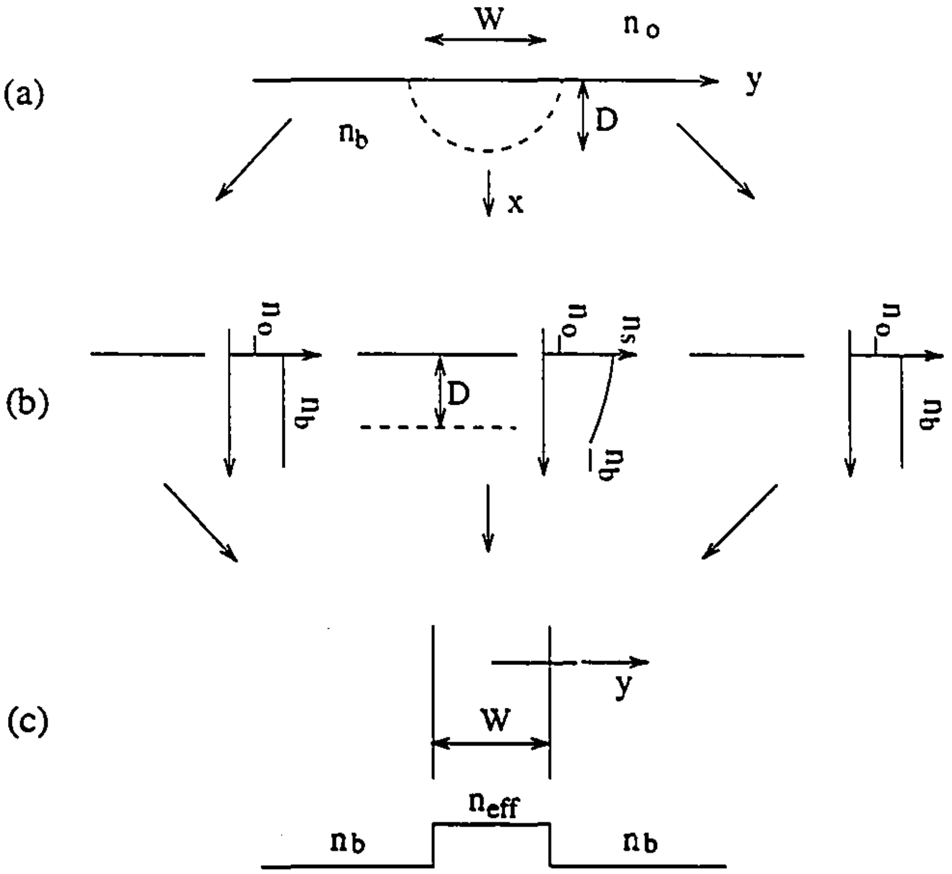

Figure 2.9: A schematic diagram of the implementation of the effective index method for an ion-exchanged channel waveguide.

Bibliography

[1] R.V. Ramaswamy and R Srivastava, "Ion-exchanged glass waveguides: a review", J. Lightwave Technol., vol. LT-6, pp.984-1001, 1988.

[2] J. Heading, *An introduction to phase-integral methods*, Methuen, London, 1962.

[3] M.J. Adams, *An Introduction to Optical Waveguides*. John Wiley and Sons, Chapter 4 and 5, 1981.

[4] F. Xiang and G.L. Yip, "A modified WKB method for the improved phase shift at a turning point", IEEE Journal of Lightwave Technology, vol. 12, pp.443-452, March, 1994.

[5] A.H. Hartog and M.J. Adams, "On the accuracy of the WKB approximation in optical dielectrical waveguides", Optical and Quantum Electron., vol.9, pp.223-232, 1977.

[6] M. Belanger and G.L. Yip, "A passive three-branch optical power divider in $LiNbO_3$", Fiber and Integrated Optics, vol.5, no.1, pp.65-79, 1984.

[7] M. Abramowitz and I. Stegun, *Handbook of Mathematical Functions*. Dover publication Inc., New York, tenth printing, Chapter 10, 1972.

[8] R. Srivastava, C.K. Kao, and R.V. Ramaswamy, "WKB analysis of planar surface waveguides with truncated index profiles", Journal of Lightwave Technology, vol. LT-5, No.11, pp.1605-1609, November 1987.

[9] M.D. Feit and J.A. Fleck, "Light propagation in graded-index optical fiber", Appl. Opt., vol.17, No.24, pp.3990- 3998, 1978.

[10] L. Thylen, "The beam propagation method: an analysis of its applicability", Opt. Quan. Electron., vol. 15, pp. 433-439, 1983.

[11] Y. Chung and N. Dagli, "A assessment of finite difference beam propagation method", IEEE J. Quautum Electron., vol. 26, no. 8, pp. 1335-1339, 1990.

[12] Y. Chung and N. Dagli, "Explicit finite difference beam propagation method: application to semiconductor rib waveguide Y-junction analysis" Electron. Lett., vol. 26, no. 11, pp. 711-713, 1990.

[13] E.C. DuFort and S.P. Frankel, "Stability conditions in the numerical treatment of parabolic differential equations", Math. and Other Aids to Comp., vol. 7, no. 41, pp. 135-153, 1953.

[14] F. Xiang and G.L. Yip, "An Explicit and stable finite difference 2-D beam propagation method", IEEE Photon. Technol. Lett., vol.6, no. 10, pp.1248-1250, 1994.

[15] F. Xiang and G.L. Yip, "An Explicit and stable finite difference BPM for applications to device analysis and design", Conference proceedings, International Symposium on Guided-Wave Optoelectronics, New York, Oct., 1994.

[16] P. Duchateau and D.W. Zachmann, "Partial differential equation", Schaum's outline series, McGraw-Hill, 1986.

[17] M.S. Stern, "Semivectorial polarised finite difference method for optical waveguides with arbitrary index profiles", IEE Proc., Pt. J, vol. 135, no. 1, pp. 56-63, 1988.

[18] W.P. Huang, C.L. Xu, S.T. Chu, and S.K. Chaudhuri, "A vector beam propagation method for guided-wave optics", IEEE Photon. Technol. Lett., vol.3, no 10, pp. 910-913, 1991.

[19] G.R. Hadley, "Transparent boundary condition for beam propagation", Optics Lett., Vol. **16**, no. 9, pp. 624-626, 1991.

[20] G.B. Hocker and W.K. Burns, "Mode dispersion in diffused channel waveguides by the Effective index method", Appl. Opt., vol. 16, pp.113-118, 1977.

2.8 Appendix

2.8.1 Deduce Eq.(2.41) from Eq.(2.42)

The asymptotic forms of Airy functions are given by

$$A_i \approx (2\sqrt{\pi}\xi^{1/4})^{-1} exp[-(2/3)\xi^{3/2}] \quad \text{for } \xi > 0 \tag{2.85}$$

$$B_i \approx (\sqrt{\pi}\xi^{1/4})^{-1} exp[(2/3)\xi^{3/2}] \quad \text{for } \xi > 0 \tag{2.86}$$

$$A_i \approx (\sqrt{\pi}|\xi|^{1/4})^{-1} sin[(2/3)|\xi|^{3/2} + \pi/4] \quad \text{for } \xi < 0 \tag{2.87}$$

$$B_i \approx (\sqrt{\pi}|\xi|^{1/4})^{-1} cos[(2/3)|\xi|^{3/2} + \pi/4] \quad \text{for } \xi < 0 \tag{2.88}$$

For $x < x_t$, $\xi < 0$ (see Eqs.(2.39) and(2.44). Replacing the Airy function in Eq.(2.42), we have

$$\phi \approx B(\sqrt{\pi}|\xi|^{1/4})^{-1} sin[(2/3)|\xi|^{3/2} + \pi/4] + C(\sqrt{\pi}|\xi|^{1/4})^{-1} cos[(2/3)|\xi|^{3/2} + \pi/4]. \tag{2.89}$$

If the index slope at x_t is approximated by G given by Eq.(2.39), we can use Eqs.(2.38) and (2.44) for $x < x_t$. Solving $(x - x_t)$ from Eq.(2.38) and using Eq.(2.22), we have

$$x - x_t = Q^2/G. \tag{2.90}$$

Then

$$|\xi|^{-1/4} = |-G^{1/3}(x - x_t)|^{-1/4} = |G|^{1/6}/\sqrt{Q} \tag{2.91}$$

and

$$(2/3)|\xi|^{3/2} = (2/3)|-G^{1/3}(x-x_t)|^{3/2} = \int_x^{x_t} |G|^{1/2}|(x_t-x)|^{1/2}dx = \int_x^{x_t} Qdx. \quad (2.92)$$

Substituting the above two equations into Eq.(2.89), we obtain Eq.(2.41), which means that Eqs.(2.41) and (2.42) satisfy the connecting condition at x_t.

2.8.2 The dispersion equation (2.45)

At x=0, letting the field and its derivative continue (see Eqs.(2.40)-(2.43)) leads

$$A = \frac{|G|^{1/6}}{\sqrt{\pi Q}}\{Bsin[\Omega+\pi/4]+Ccos[\Omega+\pi/4] \quad (2.93)$$

and

$$\frac{A}{n^2(0^-)}k_0\sqrt{n_e^2-n^2(0^+)} = \frac{|G|^{1/6}}{n^2(0^+)\sqrt{\pi Q}}\{Csin[\Omega+\pi/4]-Bcos[\Omega+\pi/4]. \quad (2.94)$$

respectively. Solving the ratio -C/B from above two equations, we have

$$-\frac{C}{B} = \frac{psin(\Omega+\pi/4)+cos(\Omega+\pi/4)}{pcos(\Omega+\pi/4)-sin(\Omega+\pi/4)} \quad (2.95)$$

where

$$p \equiv \eta_1\sqrt{\frac{n_e^2-n_{0-}^2}{n_{0+}^2-n_e^2}}. \quad (2.96)$$

At x=d, $\xi=\xi_d$, we have

$$BAi(\xi_d)+CBi(\xi_d)=E \quad (2.97)$$

and

$$-G^{1/3}[BAi'(\xi_d)+CBi'(\xi_d)] = -Ek_0\sqrt{n_e^2-n^2(d^+)}. \quad (2.98)$$

Solving -C/B from the above two equations, we have

$$-C/B = \frac{P_dA_i(\xi_d)-G^{1/3}A_i'(\xi_d)}{P_dB_i(\xi_d)-G^{1/3}B_i'(\xi_d)} \equiv q \quad (2.99)$$

Equating (2.95) and (2.99) and doing some algebra lead the following equation

$$\begin{aligned} tan(\Omega - \pi/4) &= \frac{p+q}{1-pq} \\ or &= \frac{tan(tan^{-1}p) + tan(tan^{-1}q)}{1 - tan(tan^{-1}p)tan(tan^{-1}q)} \\ or &= tan(tan^{-1}p + tan^{-1}q). \end{aligned} \tag{2.100}$$

As result, we have

$$\Omega = M\pi + tan^{-1}p + \pi/4tan^{-1}q. \tag{2.101}$$

Thus, substituting Ω, p, and q in Eq.(2.101) by Eqs.(2.27), (2.96), and (2.99), respectively, we can obtain the dispersion equation (2.45).

2.8.3 Derivation of Eq.(2.61)

Using Eq.(2.59) for $\partial\psi/\partial z$ and Eq.(2.60) for $\partial^2\psi/\partial z^2$ in Eq.(2.17) at $(y = y_m, z = z_n)$, we have

$$\begin{aligned} &\frac{\partial^2\psi_{m,n}}{\partial z^2} - 2jk_0n_r\frac{\psi_{m,n+1} - \psi_{m,n-1}}{2\Delta z} + 2jk_0n_r\frac{\Delta z^2}{6}\frac{\partial^3\psi_{m,n}}{\partial z^3} \\ &+ \frac{\psi_{m+1,n} - 2\psi_{m,n} + \psi_{m-1,n}}{\Delta y^2} - \frac{\Delta y^2}{12}\frac{\partial^4\psi_{m,n}}{\partial y^4} + k_0^2(n^2 - n_r^2)\psi_{m,n} = 0. \end{aligned} \tag{2.102}$$

Multiplying $j\Delta z/k_0n_r$ on both sides of above equation and using the notations of Eqs.(2.62) and (2.63), the above equation can be reduced to

$$\begin{aligned} &-r\Delta y^2\frac{\partial^2\psi_{m,n}}{\partial z^2} + r(\psi_{m,n+1} - \psi_{m,n-1}) - \frac{\Delta z^3}{3}\frac{\partial^3\psi_{m,n}}{\partial z^3} \\ &+ r(\psi_{m+1,n} - 2\psi_{m,n} + \psi_{m-1,n}) + \frac{\Delta y^4}{12}\frac{\partial^4\psi_{m,n}}{\partial y^4} - r\alpha 2\psi_{m,n} = 0. \end{aligned} \tag{2.103}$$

Therefore

$$\begin{aligned} \psi_{m,n+1} &= \psi_{m,n-1} + r(\psi_{m+1,n} + \psi_{m-1,n}) - (1-\alpha)r(2\psi_{m,n}) \\ &+ r\Delta y^2\frac{\partial^2\psi_{m,n}}{\Delta z^2} + \frac{1}{3}\Delta z^3\frac{\partial^3\psi_{m,n}}{\partial z^3} - \frac{r}{12}\Delta y^4\frac{\partial^4\psi_{m,n}}{\partial y^4}. \end{aligned} \tag{2.104}$$

Taking the last two terms as higher oder terms and expressing the error by Er1 given in Eq.(2.64), we derive Eq.(2.61) from the above equation.

2.8.4 Von Neumann stability condition

Let $v_{m,n} = \xi^n exp(j\eta m)$. where η is real. Substituting it into Eq.(2.74) and neglecting Er2. we have

$$\begin{aligned}\xi^{n+1}e^{j\eta m} &= \frac{1-r(1-\alpha)}{1+r(1-\alpha)}\xi^{n-1}e^{j\eta m}\\ &+\frac{r}{1+r(1-\alpha)}\xi^{n}(e^{j\eta m}e^{j\eta}+e^{j\eta m}e^{-j\eta})\end{aligned}$$

or

$$\xi^2 = \frac{1-r(1-\alpha)}{1+r(1-\alpha)} + \frac{r}{1+r(1-\alpha)}\xi 2cos\eta. \qquad (2.105)$$

Solving ξ leads

$$\xi = \frac{1}{1+r(1-\alpha)}[rcos\eta \pm \sqrt{r^2cos^2\eta + 1 - r^2(1-\alpha)^2}]. \qquad (2.106)$$

Assume the medium is lossless and define

$$t \equiv -\frac{\Delta z}{n_r k_0 \Delta y^2} \quad (\equiv \text{-jr}). \qquad (2.107)$$

Thus, t is real and the square root in Eq.(2.106) can be expressed by

$$\sqrt{1+t^2(1-\alpha)^2 - t^2cos^2\eta}.$$

Set a condition

$$1+t^2(1-\alpha)^2 - t^2cos\eta \geq 0 \quad \text{for all } \eta. \qquad (2.108)$$

It can be simplified to

$$1/t^2 \geq 2\alpha - \alpha^2. \qquad (2.109)$$

Since α is usually small, the second term on the right side of (2.109) can be neglected. Replacing t and α with Eqs.(2.107), (2.62), and (2.63) we have the condition given by

$$\frac{n_r^2\Delta y^2}{\Delta z^2} \geq (n^2 - n_r^2). \qquad (2.110)$$

Obviously, if $n(y,z) \leq n_r$, the condition can always be satisfied and if $n(y,z) > n_r$, the condition becomes

$$\Delta z \leq \frac{n_r}{\sqrt{n^2 - n_r^2}} \Delta y \quad \text{for } n(y,z) > n_r. \tag{2.111}$$

Thus, if the medium is lossless and the condition (2.111) can be satisfied, the square root in Eq.(2.106) is real. Then

$$| \xi | = \frac{t^2 cos^2 \eta + [-t^2 cos^2 \eta + 1 + t^2 (1-\alpha)^2]}{| 1 + r(1-\alpha) |^2} = 1 \quad \text{for all } \eta, \tag{2.112}$$

which means that the scheme is Von Neumann stable. The scheme is unconditionally stable for $n(y,z) \leq n_r$ and a lossless medium.

Chapter 3

Y-branch Mode Splitter

An asymmetric Y-branch as shown in Fig.3.1 has a very small branch angle. Assume that the propagation constant of the fundamental mode in branch 1 is large than that in branch 2, considering the two branches separately. Thus, an incoming fundamental mode in the main branch will travel into branch 1 while the second order-mode will go into branch 2 (see Fig.3.4). This Y-branch is known as a mode splitter.

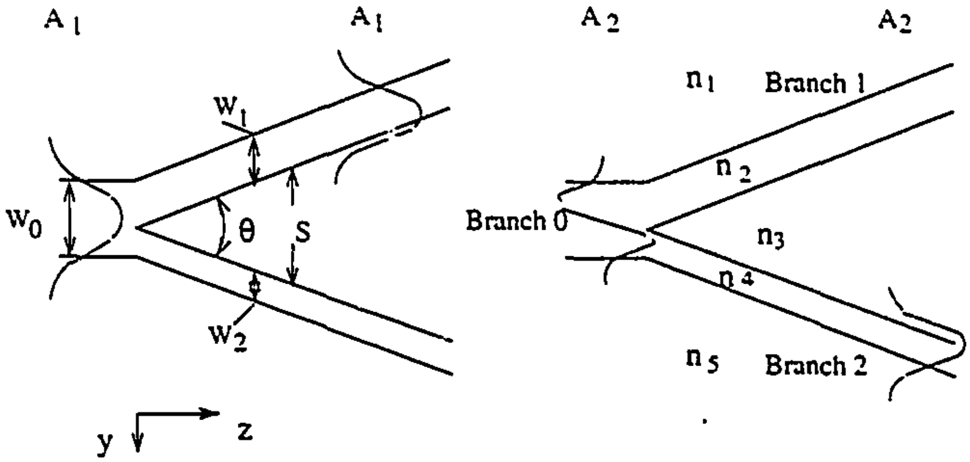

Figure 3.1: An asymmetric Y-branch with a small branch angle.

Since all the devices fabricated or proposed in this thesis are based on or related to the mode splitter, we will spend the following chapter to discuss this topic. The work was first studied by Yajima[1]. Burns[2] and Marcuse[3] also made some important contributions late on. Here, our attention is mainly directed towards understanding the principle. The details can be found in [1]- [3].

3.1 Introduction

In a two parallel waveguide structure, the local modes are orthogonal, in other words, they do not couple with each other. It will not be true if these two waveguides are not parallel, for instance, a waveguide branch. If the taper slope of a waveguide branch is infinitely small, the coupling among the local modes are negligible and the power in a mode is conserved for its propagation through the branch. This corresponds to an adiabatic passage.

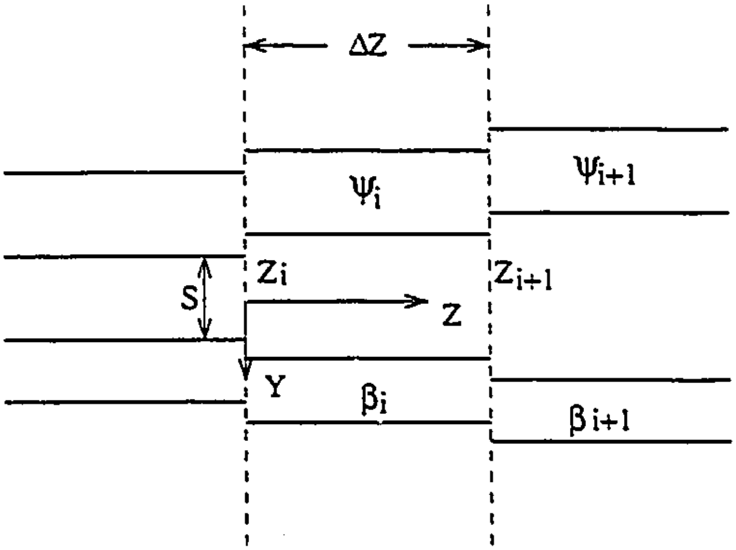

Figure 3.2: Approximated geometry for the five-layer region of branching waveguides.

However, as the taper slope is increased we expect that the adiabatic approximation will break down and a power transfer will occur from an input mode to other guided and radiation modes, both transmitted and reflected. This problem can be conveniently treated by the step approximation method of Marcuse [3]. The continuous branch taper is approximated by a series of discontinuous, abrupt steps, separated by regions of parallel five-layer waveguide after the apex (see Fig.3.2).

We assume the waveguide modes of interest to be incident on a step and compute the transmitted mode amplitudes by requiring the transverse-field components to be continuous at the step. By breaking up the taper into a large number of small steps and repeating this process at each step, a reasonable approximation to the effect of a given taper slope is obtained.

Mode propagation is assumed in the z direction. The y direction is normal to the waveguide layers, and fields and geometry are assumed unchanged in the x direction. The dispersion equation of this five-layer planar waveguide for TE modes is given by [1]

$$\begin{aligned} &\{(\gamma_1 + \gamma_3)\gamma_2 + (\gamma_1\gamma_3 - \gamma_2^2) tan\gamma_2 w_1\} \\ &\cdot\{(\gamma_3 + \gamma_5)\gamma_4 + (\gamma_3\gamma_5 - \gamma_4^2) tan\gamma_4 w_2\} \\ -exp(-2\gamma_3 s)&\{(\gamma_3 - \gamma_1)\gamma_2 + (\gamma_1\gamma_3 + \gamma_2^2) tan\gamma_2 w_1\} \\ &\cdot\{(\gamma_3 - \gamma_5)\gamma_4 + (\gamma_3\gamma_5 + \gamma_4^2) tan\gamma_4 w_2\} \quad = 0, \end{aligned} \tag{3.1}$$

where the transverse wave number

$$\gamma_l = k_0\sqrt{| n_l^2 - n_e^2 |}, \quad \text{l=1,...,5.} \tag{3.2}$$

We restrict our attention to two transverse electric guided modes, the first and second. The electric fields for the guided modes can be written as

$$e_x = E(z)\psi(y,z)exp(-j\alpha(z)) \tag{3.3}$$

where

$$\alpha(z) = \beta z + \phi. \tag{3.4}$$

E(z) is the real amplitude at a point z, $\psi(y, z)$ the real, y dependent local-normal mode field distribution, and ϕ a phase constant. Boundary conditions for TE modes require e_x and h_y to be continuous across a step at z, which leads to

$$\begin{aligned} & E_{1i}\psi_{1i}exp(-j\alpha_{1i}) + E_{2i}\psi_{2i}exp(-j\alpha_{2i}) \\ & +E^R_{1i}\psi_{1i}exp(j\alpha^R_{1i}) + E^R_{2i}\psi_{2i}exp(j\alpha^R_{2i}) + e^{ref} \\ = {} & E_{1i+1}\psi_{1i+1}exp(-j\alpha_{1i+1}) + E_{2i+1}\psi_{2i+1}exp(-j\alpha_{2i+1}) + e^{trans} \end{aligned} \tag{3.5}$$

and

$$\begin{aligned} & \beta_{1i}E_{1i}\psi_{1i}exp(-j\alpha_{1i}) + \beta_{2i}E_{2i}\psi_{2i}exp(-j\alpha_{2i}) \\ & -\beta_{1i}E^R_{1i}\psi_{1i}exp(j\alpha^R_{1i}) - \beta_{2i}E^R_{2i}\psi_{2i}exp(j\alpha^R_{2i}) + h^{ref} \\ = {} & \beta_{1i+1}E_{1i+1}\psi_{1i+1}exp(-j\alpha_{1i+1}) + \beta_{2i+1}E_{2i+1}\psi_{2i+1}exp(-j\alpha_{2i+1}) + h^{trans} \end{aligned} \tag{3.6}$$

where the first subscripts 1 and 2 are used to denote the order of the modes, the second subscripts i and i+1 are for the incident and transmitted fields across the step respectively, E^R is the amplitude of reflected guided modes, e^{ref} and h^{ref} represent reflected radiated modes, and e^{trans} and h^{trans} transmitted radiated modes. We define an overlap integral as

$$I_{pq,\xi\eta} = \int \psi_{pq}\psi_{\xi\eta}dy, \quad \text{p},\xi = 1,2 \text{ and q}.\eta = i, i+1, \tag{3.7}$$

where the integral covers the range of y where fields are not zero. A mode amplitude (E^s) is introduced for the normalization, which corresponds to a mode power of unity. At any point z, E^s is related to mode power (P) by

$$\sqrt{P_{p,q}} = 1 = E^s_{p,q}\sqrt{\frac{\beta_{p,q}}{2k_0}I_{pq,pq}}, \quad \text{p=1,2 and q=i,i+1}. \tag{3.8}$$

By using the mode orthogonality in both Eqs.(3.5) and (3.6) and keeping only the first order terms based on the assumption of a small step, we obtain the following equation

$$A_{2,i+1}exp(-j\alpha_{2,i+1}) = c_{1,2}A_{1,i}exp(-j\alpha_{1,i}) + c_{2,2}A_{2,i}exp(-j\alpha_{2,i}), \tag{3.9}$$

where

$$A_{p,q} = E_{p,q}/E^{s}_{p,q} \tag{3.10}$$

is the ratio of mode amplitude in the presence of mode conversion to that mode amplitude which corresponds to unity power. The coefficient $c_{1,2}$ is given by

$$c_{1,2} = \frac{2\sqrt{\beta_{1,i}\beta_{2,i+1}}}{(\beta_{2,i} + \beta_{2,i+1})}\left(\frac{\beta_{2,i} + \beta_{1,i+1}}{\beta_{1,i} + \beta_{1,i+1}}\right)\frac{I_{1i,2i+1}}{\sqrt{I_{1i,1i}I_{2i+1,2i+1}}}. \tag{3.11}$$

and $c_{2,2}$ can be obtained by substituting 2 for 1 in Eq.(3.11). $c_{p,\xi}$, $(p, \xi = 1, 2)$, represents the coupling of power from the mode p in "i" region to the mode ξ in "i+1" region.

The real and imaginary parts of Eq.(3.9) then completely describe the transmitted mode 2 in terms of the input modes.

$$A_{2,i+1} = c_{1,2}A_{1,i}cos(\alpha_{1,i} - \alpha_{2,i+1}) + c_{2,2}A_{2,i}cos(\alpha_{2,i} - \alpha_{2,i+1}) \tag{3.12}$$

$$tan\alpha_{2,i+1} = \frac{c_{1,2}A_{1,i}sin\alpha_{1,i} + c_{2,2}A_{2,i}sin\alpha_{2,i}}{c_{1,2}A_{1,i}cos\alpha_{1,i} + c_{2,2}A_{2,i}cos\alpha_{2,i}}. \tag{3.13}$$

Since the notation for mode 1 and 2 are symmetric, exchanging 2 with 1 in Eqs.(3.12) and (3.13) gives $A_{1,i+1}$ and $\alpha_{1,i+1}$. After obtaining the "A"s and "α"s, we let the two modes propagate over a distance $z_{i+1} - z_i$ to the next intersection at $z = z_{i+1}$ by multiplying fields of the first-mode with $exp[-j\beta_{1,i+1}(z_{i+1} - z_i)]$ and of the second-mode with $exp[-j\beta_{2,i+1}(z_{i+1} - z_i)]$ to get the fields just before the next step.

3.2 Branching Waveguides of Weak Mode Coupling

First, using the theory developed in the last section, we treat a branching waveguide with very good mode separation characteristics. Such a branch has a very small branch angle and at the same time its branch widths are largely different. In the following discussion, we assume that the wavelength $\lambda = 1.55\mu m$, TE modes, $n_1 = n_3 = n_5 = 1.498$, $n_2 = n_4 = 1.502$, $W_0 = 10.0\mu m$, $W_1 = 6.0\mu m$, $W_2 = 4.0\mu m$, and the branch angle $\theta = 0.003 rad$ (unless stated otherwise the value of an angle is in rad).

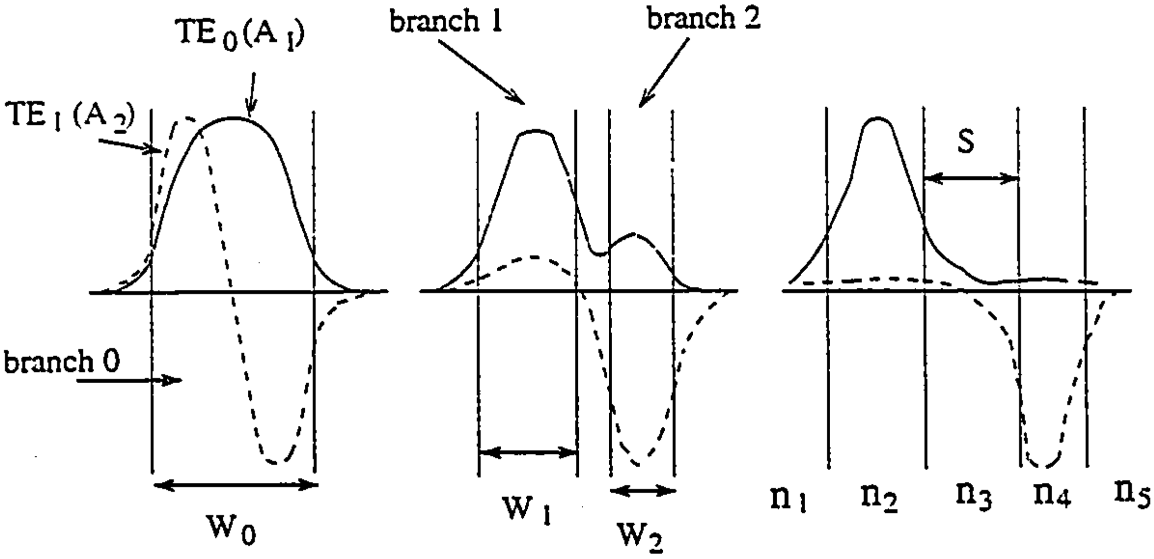

Figure 3.3: Variations of the TE mode patterns along the direction of a branching waveguide, a: zero branch separation; b: small branch separation; c: large branch separation.

Fig.3.3 shows how the mode conversions take place in the qusi-stationary electric field patterns of the TE mode in the 5-layer dielectric waveguide. As the separation s increases from 0 to ∞, the TE_0 mode of branch 0 shifts to the TE_0 mode of branch

1 through the local TE_0 mode in the branching region and the TE_1 mode shifts to the TE_0 mode of branch 2 through the local TE_1 mode in the branching region.

To clarify the manner of mode conversion and mode separation in the dielectric branching waveguide, it is helpful to compare the order of magnitude of the propagation constants for various modes in each branch.

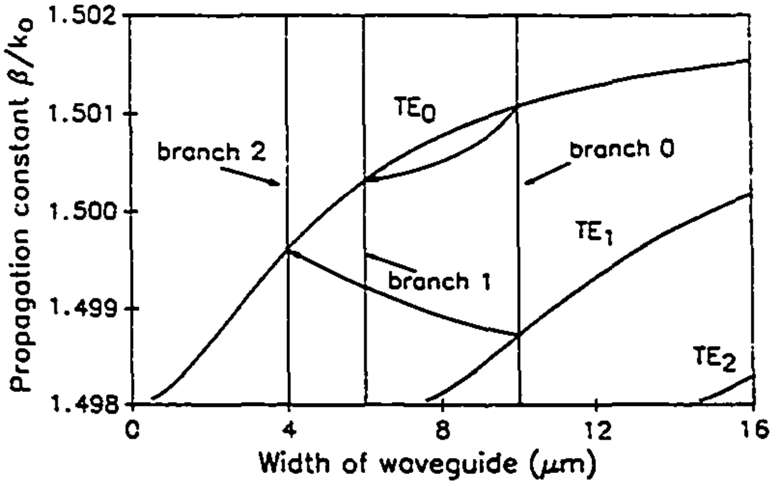

Figure 3.4: Scheme of mode conversion in the branching waveguide.

Fig.3.4 shows the dependence of the propagation constant of TE modes in a 3-layer waveguide on waveguide width. There are three straight lines. They indicate three channel guides with different widths. The propagation constants of TE modes in three different channels are given by the intersections of the dispersion curves with the corresponding straight lines. The mode conversion in the branching waveguide then takes place as indicated by the arrows in the figure.

The mode conversion process can be summarized in the following way. The TE_0 mode in branch 0 is converted into the TE mode with a larger propagation constant in the two branches, namely, in the wider branch. The TE_1 mode in the main branch is converted into the TE mode with a smaller propagation constant in the two branches,namely, in the narrower branch.

It is useful to note that the mode conversion mechanism in the branching waveguide can be explained in terms of the adiabatic theorem, which describes a motion in some dynamical state with slowly varying external parameters called adiabatic invariants. In the mode conversion process in the branching waveguide, the state is represented by a propagating wave in a particular mode through the multilayer waveguide with a slowly varying separation between the two branches being the external parameter. In this case, the adiabatic invariants are the mode number and mode energy. This means that the TE_0 mode, for instance, in branch 0 in Fig.3.1 remains, as it proceeds, to be the TE_0 mode in the multilayer waveguide to the right hand side, although the shape of mode pattern looks like the TE_0 mode associated with either branch 1 or 2.

3.3 Dependence of Branch Parameters

The discussion in the last sub-section is for an ideal Y- branch. If the branch angle is not that small, the adiabatic invariants will not be well preserved and mode conversion will not be completely in the direction as indicated by the arrows as shown in Fig.3.4. Mode coupling will occur.

As a mode splitter, we expect the normalized amplitude A_1 to be close to unity and A_2 close to zero when the TE_0 mode in branch 0 is converted into the TE_0 mode in branch 1. Two branch parameters, the branch asymmetry and the branch angle, affect the performance most as concluded in [1] and [2]. The branch asymmetry includes the branch geometry and branch index.

Taking the same parameters as given in the last section, but choosing $\theta = 0.01$ and three different branch width combinations as, (1) $W_0 = 10.0\mu m$, $W_1 = 6.5\mu m$, and

$W_2 = 3.5\mu$m; (2) $W_0 = 10.0\mu$m, $W_1 = 6.0\mu$m, and $W_2 = 4.0\mu$m; (3) $W_0 = 10.0\mu$m, $W_1 = 5.5\mu$m, and $W_2 = 4.5\mu$m, we plot A_1 and A_2 as functions of the branch separation s for these three different branch asymmetries shown in Fig.3.5. The results show that the stronger the branch asymmetry, the less A_2, and, hence, the better performance as a mode splitter.

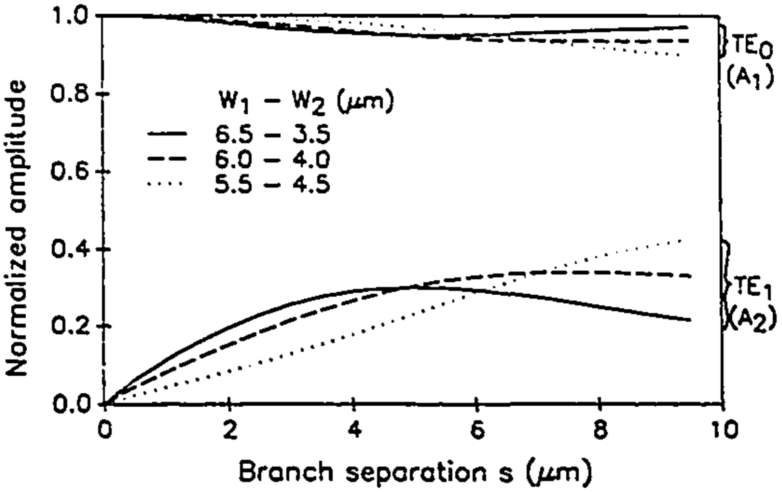

Figure 3.5: Dependence of mode amplitudes on the branch separation for different branch asymmetries.

If only the branch angle θ is changed in the example given in Fig.3.1 with $W_0 = 10\mu$m, $W_1 = 6.0\mu$m, and $W_2 = 4.0\mu$m, the normalized amplitudes A_1 and A_2 are plotted versus the branch separation s in Fig.3.6. For a small branch angle $\theta = 0.005$, the power coupled to the local TE_1 of 5-layer waveguide is very insignificant. However, when the branch angle is increased to 0.05, the branch behaves like a power divider.

A simple expression derived by Burns and Milton in [2] can be used to describe the transition boundary between a mode splitter and a power divider which is given by

$$\frac{\Delta\beta}{\theta\sqrt{\beta_0^2 - n_3^2k_0^2}} > 0.43, \tag{3.14}$$

where $\Delta\beta$ is the difference in propagation constants between branch 1 and branch 2 for infinite branch separation. Whenever the branches are symmetric ($\Delta\beta$ small) and the branch angle θ is large the structure will act as a power divider. However, when the branches are asymmetric ($\Delta\beta$ large) and the branch angle θ is small the structure will act as a mode splitter. It is expected that steeper tapers will be more loss to radiation modes so that a low-loss mode splitter will be easier to fabricate than a low-loss power divider. In this thesis work, only the mode splitter is of interest. It is expected that the left hand side of Eq.(3.14) is far less than 0.43 and the condition for mode splitting is always satisfied.

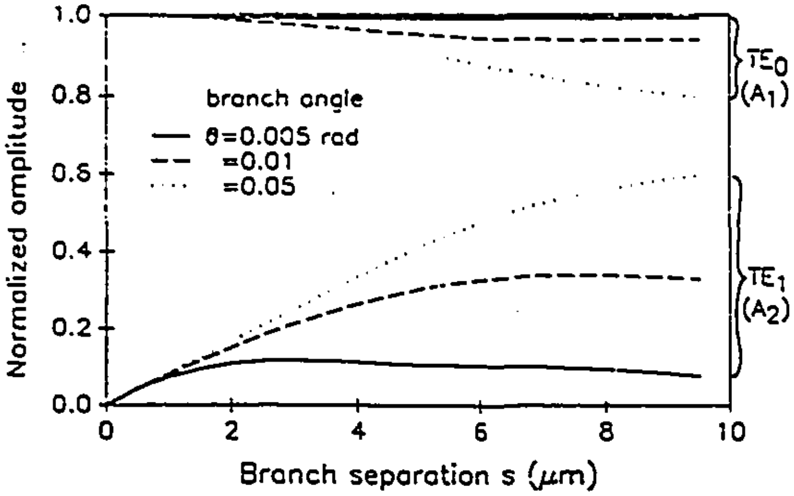

Figure 3.6: Dependence of mode amplitudes on the branch separation for different branch angles.

Bibliography

[1] H. Yajima, "Theory and applications of dielectric branching waveguides", in Proc Symp. Optical and Acoustical Micro-Elctronics, pp. 339-358, New York, 1974.

[2] W. K. Burns and A. F. Milton, "Mode conversion in planar dielectric separating waveguides", IEEE J. Quantum Electon., vol. QE-11, pp.32-39, 1975.

[3] D. Marcuse, "Radiation losses of tapered dielectric slab waveguides", Bell Syst. Tech. J., vol.49, pp.273-290, 1970.

Chapter 4

Refractive Index Measurements and Waveguide Characterizations

Before designing and fabricating the devices, many parameters have to be found, such as substrate indices, indices of sputtered Al_2O_3 layers, K^+ and Ag^+ ion-diffusion coefficients, and so on. Although some of them have been reported, there are still many of them unknown, especially those parameters at infrared wavelengths $\lambda = 1.31\mu$m and 1.55μm. Since the light at infrared wavelength is invisible, it is more difficult to measure them than those obtained at visible wavelengths. In this chapter, we will discuss the methods for the measurements and their accuracies. Those parameters measured directly or indirectly will also be presented.

4.1 Substrate Indices

The glass substrate we used is soda-lime glass mainly due to its low cost and its data availability in our Guided-Wave Photonics Laboratory. Its indices at infrared wavelengths $\lambda = 1.31\mu m$ and $\lambda = 1.55\mu m$ were still not available until we measured and established them in our laboratory.

4.1.1 Interpolation

Although, the refractive index of sodalime glass is not available in the infrared region. its value at $\lambda = 0.6328\mu m$ ($n_{sodalimeglass} = 1.5125$) is well documented in the theses produced in our lab. On the other hand, the reported refractive index for BK7 glass covers wavelengths both in visible and infrared regions given by [1]

$$n_{BK7}^2 = A_0 + A_1\lambda^2 + A_2\lambda^{-2} + A_3\lambda^{-4} + A_4\lambda^{-6} + A_5\lambda^{8} \tag{4.1}$$

where the parameters are listed in Table 4.1. Its value at $\lambda = 0.6238\mu m$ is 1.5151.

A_0	2.2718929
A_1	-1.0108077×10^{-2}
A_2	1.0592509×10^{-2}
A_3	2.0816965×10^{-4}
A_4	-7.6472538×10^{-6}
A_5	4.9240991×10^{-7}

Table 4.1: Constants of the dispersion Eq.(4.1) at 24°C

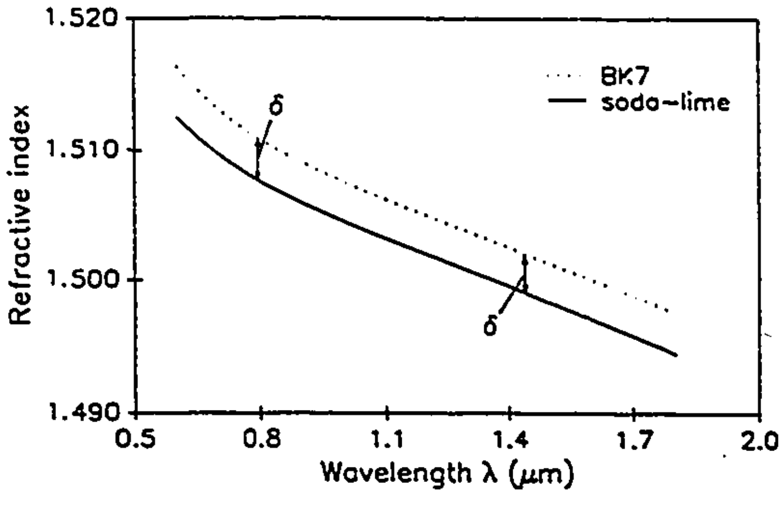

Figure 4.1: Refractive index versus wavelength, dotted line for BK7 glass and solid line for soda-lime glass. $\delta = 0.0026$.

We assume that our soda-lime glass substrates have the same dispersion character, i.e. the same index dispersion pattern versus the wavelength. Thus, the index of sodalime glass can be expressed by

$$n_{sodalime} = n_{BK7} - \delta \tag{4.2}$$

where $\delta = 0.0026$. Fig.4.1 shows the plots of both dispersion curves. Now, we have $n_{sodalime}$=1.5011 at $\lambda = 1.31\mu$m and $n_{sodalime}$=1.498 at $\lambda = 1.55\mu$m.

4.1.2 Multi-sheet Brewster angle measurement

The index values obtained in the last sub-section for the infrared wavelengths are very rough. They are guessed values. It is desirable that directly measured values can be obtained to test out the assumption made in the last sub-section.

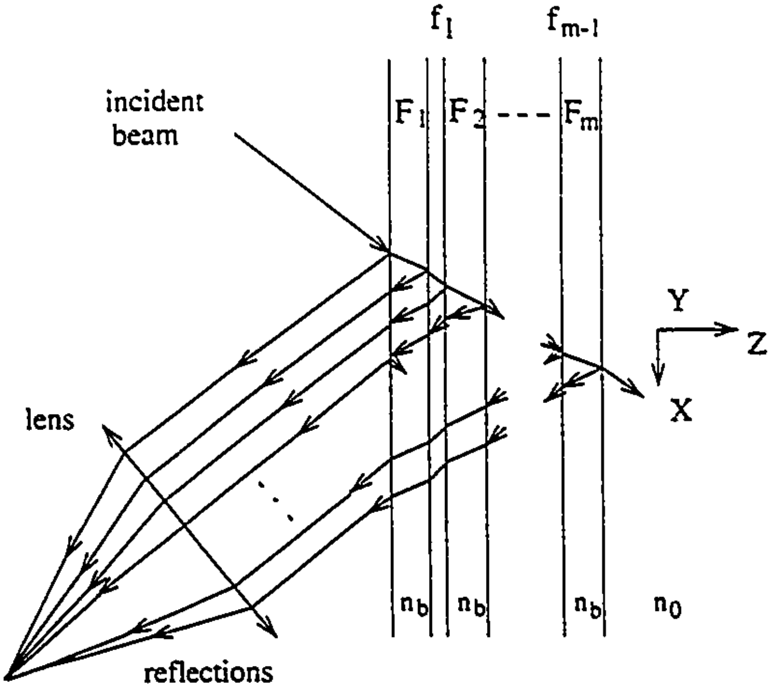

Figure 4.2: Reflection from a multi-sheet structure. n_b is the substrate index, n_0 is the index of air, F_i and f_i are thicknesses of the ith substrate and air gap, respectively, and m is the number of substrates.

Different techniques can be employed to measure the indices. However, most of them require special equipments to meet the need of high accuracy. Here, a simple, relatively accurate, and inexpensive measurement technique[2] is presented.

It is well known that the refractive index of a substrate is related to its Brewster angle φ_b via

$$n_b = n_0 tan(\varphi_b) \tag{4.3}$$

where the refractive index of air $n_0 = 1.0003$ has been assumed. The reflected light from a substrate becomes zero when a H-polarized light is incident at the Brewster angle. Stacking many identical substrates together forms a multi-sheet structure (see Fig.4.2).

The valley of this reflected intensity pattern centered at the Brewster angle becomes much narrower due to the overlapping of similar reflections from many parallel interfaces of air and substrates. Thus, measuring the Brewster angle of this multi-sheet structure can lead to a more accurate determination of the substrate index.

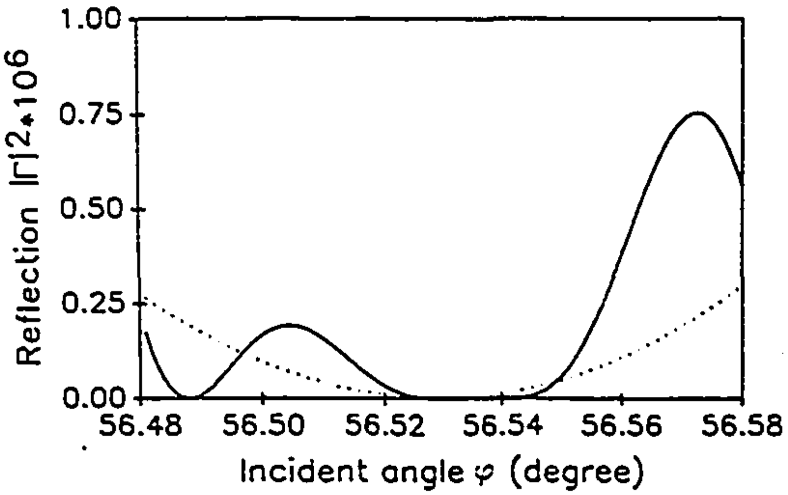

Figure 4.3: Reflections of a plane wave near the Brewster angle φ_b (= 56.529°) from one interface of air-substrate (dotted line) and from a substrate (solid line) with a thickness $F = 0.95mm$.

Considering only one interface of air and substrate, the reflected power pattern $|\Gamma|^2$ of a plane wave versus the incident angle φ is shown in Fig.4.3 (dotted line), with the substrate index $n_b = 1.5125$ and $\lambda = 0.6328\mu m$.

The pattern near the Brewster angle $\varphi_b (= 56.529°)$ is flat which results in a $\Delta\varphi_b \approx \pm 2'$ measurement error in φ_b with a corresponding error $\Delta n_b \approx \pm 0.002$ in the refractive index. The accuracy is only up to the second decimal place. The broadness of the reflection pattern is the main reason for causing this error.

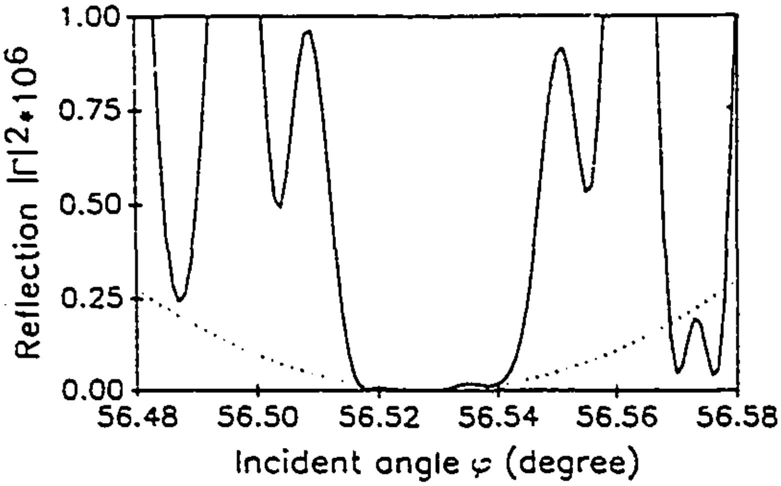

Figure 4.4: Reflections of a plane wave near the Brewster angle φ_b (= 56.529°) from a multi-sheet structure (solid line) with $m = 5$, F_i and f_i $(i = 1, 2, \cdots, m)$ are randomly chosen between (0.945mm, 0.955mm) and (0.0, 1.0μm) respectively.

In reality, the thicknesses of substrates and air gaps can not be exactly equal. They should be allowed to have certain ranges of randomness which can be easily produced by a computer program[3]. Letting F_i and f_i $(i = 1, 2, \cdots, m)$ be randomly chosen between $(0.945 - 0.955mm)$ and $(0.0 - 1.0\mu m)$ respectively, we have calculated the total reflection of a multi-sheet structure for 5 substrates as shown in Fig.4.4 (solid curve).

With an increase in the number of the substrates, the pattern becomes narrower.

A comparison with the dotted curve (reflection from a single interface) in Fig.4.5 reveals that the former is more than four times narrower near φ_b if $| \Delta\varphi_b |< 2'$ ($| \Gamma |^2 < 0.13 \times 10^{-6}$) for the dotted line is assumed. Thus, measuring φ_b of this 20-substrate structure, one can expect the error to be less than 0.4′ corresponding to $| \Delta n_b |< 0.0004$.

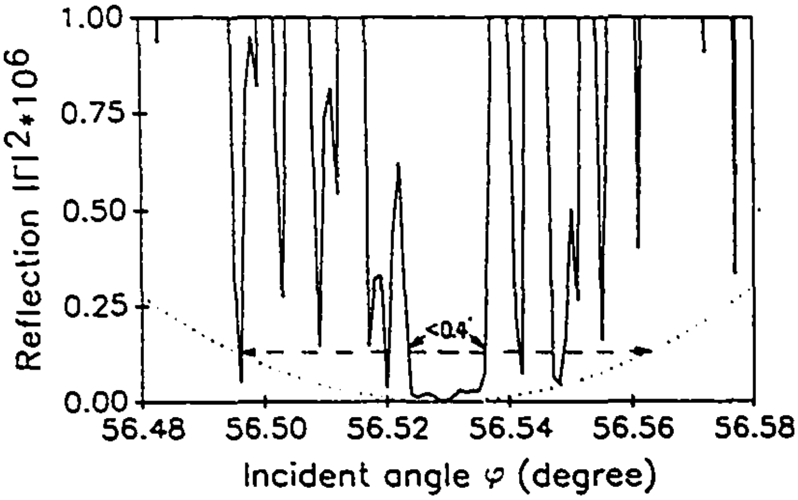

Figure 4.5: See the caption of Fig.4.4 but with m=20. The dashed line indicates the range of 2′ measurement error in φ_b for one air-substrate interface.

The analysis above is based on the assumption that the incident wave is an ideal infinite plane wave. In practice, a laser beam is used as the light source. The total reflection of a laser beam by a multi-sheet structure contains a series of beam spots. Fortunately, these reflected beams are all nearly parallel. They can be focused onto one spot by an optical lens as shown in Fig.4.2. Thus, the focused spot is the superposition of all the reflected beams and its intensity versus the incident angle behaves just like that of the reflected waves discussed under a plane wave assumption in the previous paragraphs.

The measurement setup is very simple. A rotating stage, a focusing lens, a laser source, and a sample holder are all that needed. For measuring the substrate index at infrared wavelengths one also needs a power detector which covers these wavelengths. Stacking many cleaned substrates together face to face in the sample holder forms the multi-sheet structure. It is worth noticing that the air gaps can not be controlled during the assembly. They are formed randomly and incoherently. Before the measurements, a sample alignment is necessary because of the general tapered nature of these samples, the two faces of each sample not being perfectly parallel. The detail of the alignment has been reported in [2].

The scheme was tested by measuring the indices of BK7 glass substrates at three different wavelengths $\lambda = 0.6328\mu m$, $= 1.152\mu m$, and $= 1.523\mu m$. The light sources used were all He-Ne lasers. For BK7 glass substrates (Schott), 20 pieces were used to form the multi-layer sample. The thicknesses of BK7 glass substrates were between 0.99 mm to 1.01 mm. The glasses have roughly the same width (25 mm) and length (75 mm). The measurements for each wavelength were repeated 15 times. The results are presented in Table 4.1 where the standard deviation is for fifteen separate measurements made with the same set of samples but without any additional realignments. In Table 4.2, the published index values are given in [1].

λ μm	Measured index N_b	Standard deviation σ	Published index value n_b[1]	Difference $\mid N_b - n_b \mid$
0.6328	1.515259	1.62×10^{-4}	1.515090	1.69×10^{-4}
1.152	1.506294	1.67×10^{-4}	1.505548	7.46×10^{-4}
1.523	1.501475	1.67×10^{-4}	1.501015	4.60×10^{-4}

Table 4.2: Measurement results for BK7 glass substrates (m=20)

The small standard deviations ($< 3.5 \times 10^{-4}$) and discrepancies with published results [1] ($< 7.5 \times 10^{-4}$) given in the tables show that the accuracy of this technique can be up to the third decimal place and, hence, is accurate enough for general device design purposes.

4.1.3 Measured soda-lime substrate indices

For sodalime glass substrates (Fisher), 26 pieces were used to form the multi-sheet sample. The thicknesses of sodalime glass substrate were between 0.94 mm to 0.96 mm. The sizes of the substrate were roughly the same as those of BK7 glass. The measurements were carried out in the same way as for the BK7 glass. The results are presented in Table 4.3. The result at $\lambda = 0.6328 \mu m$ shows a good agreement with the published value. The results at other two wavelengths agree well with those established from Eq.(4.2), which also establish that the estimates were reasonable. Eq.(4.2) then will be used to produce the indices for sodalime glass substrate at wavelengths between 1.2 and 1.6 μm by interpolation.

λ μm	Measured index N_b	Standard deviation σ	Index values by other methods n_b^*	Difference $\mid N_b - n_b \mid$
0.6328	1.512802	3.35×10^{-4}	1.5125	3.02×10^{-4}
1.152	1.503153	3.43×10^{-4}	1.5030	1.53×10^{-4}
1.523	1.498642	1.98×10^{-4}	1.4984	2.42×10^{-4}

Table 4.3: Measurement results for soda-lime glass substrates (m=26). *: the value obtained from Eq.(4.2)

4.2 Sputtered Al_2O_3 Layer

It is well known that the refractive index of a sputtered Al_2O_3 is different from its bulk index [4]. The index of sputtered Al_2O_3 depends on the conditions of the sputtering environment. We conducted the characterization of sputtered Al_2O_3 on a Cooks RF sputtering system for different time durations and different sputtering power levels. The characterization can be described as follows. A slab waveguide is formed after sputtering on a glass substrate. The effective indices of the guided modes in each sample were obtained by measuring the synchronous angles with a prism coupler [5] given by

$$n_e = n_p sin[\alpha_p + sin^{-1}(\frac{sin\varphi}{n_p})] \quad (4.4)$$

where n_p, α_p, and φ are the prism index, the prism base angle, and the synchronous angle, respectively.

After measuring the waveguide effective indices, several independent dispersion equations can be established based on a step-index three layer slab waveguide for the number of modes it supports. Each dispersion equation contains two unknown parameters, the film index n_c and the film thickness f. At least one pair of dispersion equations is needed for solving the two parameters. The different combinations of the pairs for one sample supporting more than two modes result in different solutions. The averages of these solutions yield the solutions for the two parameters. For a sample supporting only one mode, we sputtered again on top of the same sample under the same sputtering conditions. The sample, then, may support two modes or still one mode. If it supports one mode, two independent dispersion equations can be established for two single mode slab waveguides before and after the second sputtering. This time, the two unknown parameters are n_c and the deposited film thickness f and hence sputtering rate α (which is proportional to f) since the sputtering rates should be the same in both sputtering.

The sputtering were carried out for four different RF input power levels, P=50w, 27.5w, 18.75w, and 12.5w, corresponding to the target voltages, 1kv, 0.75kv, 0.62kv, and 0.5kv, respectively. For the layer made at P=50w input RF power for 5 hours, no modes were observed. The modes were observed only after the sample had been annealed for two hours at 400°C with a constant oxygen flow in a horizontal furnace. Since the annealing at this high temperature would affect existing ion-exchanged waveguides in future devices, the sputtering at this high input power was not studied further. For P=27.5w input RF power, a sample was sputtered for 11 hours. on a sodalime glass substrate (n_b=1.5125 at $\lambda = 0.6328\mu m$). All the data in this subsection are for TM polarization and measured at $\lambda = 0.6328\mu m$ from a He-Ne laser. However, little difference was found in our measurements between TE and TM polarizations. Three modes were measured, n_{e1}=1.615643, n_{e2}=1.586777, and n_{e3}=1.540134. Three independent pairs of dispersion equations can be formed to solve for the film index n_c and the film thickness f as shown in Table 4.4. The sputtering rate is about $0.1457\mu m$ per hour.

m	1-2	1-3	2-3	Average
n_c	1.625335	1.625374	1.625592	1.625433
f(μm)	1.605370	1.601689	1.599461	1.602173

Table 4.4: Indirectly measured Al_2O_3 film index and thickness for 0.75kv target voltage (P=27.5w), m is a mode number.

Another sample (on sodalime substrate) was at first sputtered for three hours with P=18.73. Only one mode was measured which had an effective index n_{e1}=1.53310. It was then sputtered for another three hours with the same input power. The only measured effective index was 1.58250. With these two effective indices and the times of their sputtering, two independent dispersion equation could be obtained with n_c and the sputtering rate α unknown. Solving the two equations yielded the results of n_c=1.6180 and $\alpha = 0.1183\mu m/\text{hr}$.

The last sample was also made on a soda-lime glass. It was at first sputtered for 4.5 hours with P=12.5w. Only one mode n_{e1}=1.5167 was measured. It was then sputtered for another hour under the same conditions. Again, only one mode n_{e1}=1.5259 was measured. The film index was found to be 1.5833 and the sputtering rate was 0.083/hr. The results of the above three samples are summarized in Fig.4.6. The figure shows that both the film index and sputtering rate are increased with the increasing of the target voltage, which reveals the same phenomena as reported in [4].

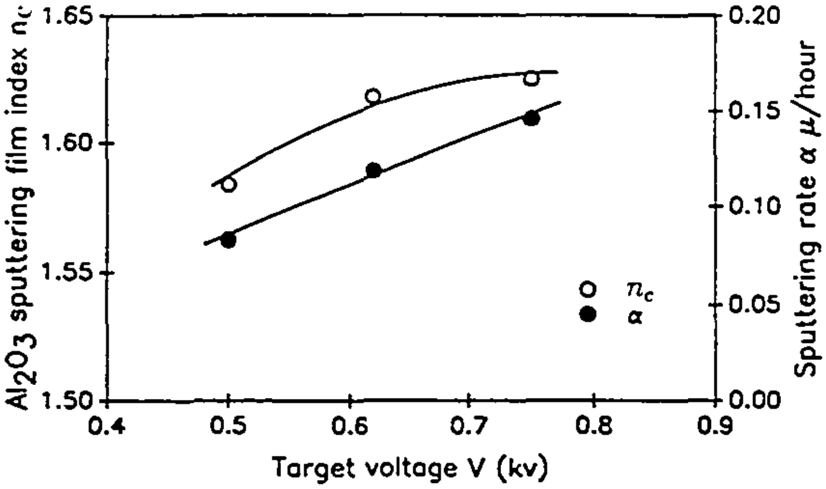

Figure 4.6: The dependences of Al_2O_3 film refractive index and its sputtering rate on the target voltage at $\lambda = 0.6328\mu m$.

To obtain the refractive indices at infrared wavelengths, the dispersion of the sputtered Al_2O_3 film index is assumed to be the same as that of the bulk index. For the bulk index, we have [6]

$$n(\lambda) = (1 + \frac{A_1\lambda^2}{\lambda^2 - \lambda_1^2} + \frac{A_2\lambda^2}{\lambda^2 - \lambda_2^2} + \frac{A_3\lambda^2}{\lambda^2 - \lambda_3^2})^{1/2} \tag{4.5}$$

where those constants are given in Table 4.5.

λ_1=0.06144821	λ_1^2=0.00377588	A_1=1.023798
λ_2=0.1106997	λ_2^2=0.0122544	A_2=1.058264
λ_3=17.92656	λ_3^2=321.3616	A_3=5.280792

Table 4.5: Constants of the dispersion Eq.(4.5) at 24°C

At $\lambda = 0.6328\mu m$ the bulk index of Al_2O_3 given by Eq.(4.5) is 1.76596. The cladding index at $\lambda = 0.6328\mu m$ can be established to be 1.6254 by mode index measurement as discussed before if the target voltage is v=0.75 kv. Thus, the film indices of Al_2O_3 at infrared wavelengths are approximately given by

$$n_c(\lambda) = n(\lambda) - \delta \tag{4.6}$$

where $\delta = 1.76596 - 1.6254 = 0.14056$. Fig.4.7 shows the dispersion curves for both the bulk and cladding film of Al_2O_3.

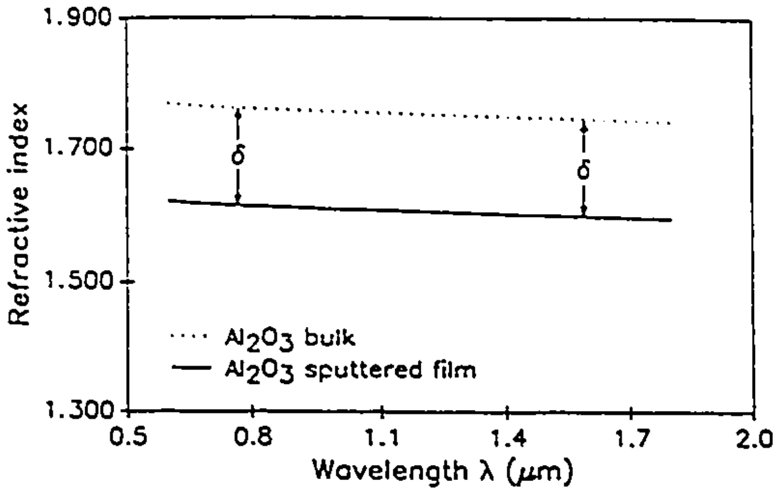

Figure 4.7: Refractive index versus wavelength, dotted line for the bulk of Al_2O_3 and solid line for the of Al_2O_3 sputtered at 0.75 kv target voltage. $\delta = 0.14056$.

4.3 Characterization of K^+ Ion-exchanged Waveguides

The K^+-ion diffused planar waveguide samples were fabricated by immersing sodalime glass substrates in molten KNO_3 at 385°C for different time durations. The waveguide effective indices were obtained by solving Eq.(4.4) after the synchronous angles have been measured with the prism coupler technique. Since at $\lambda = 1.152\mu m$ or $1.523\mu m$, the He-Ne laser beam is invisible, a He-Ne laser beam at $\lambda = 0.6328\mu m$ was used to help with the alignment as indicated in Fig.4.8 [7].

This scheme yielded an estimated accuracy of $\pm 1.0 \times 10^{-4}$ in the measured effective index n_e. The refractive indices of the prism coupler (flint glass) at $\lambda = 1.152\mu m$ and $1.523\mu m$ were obtained from the data in [1] by interpolation to be n_p=1.7523 and 1.74485 respectively. The corresponding indices for the soda-lime substrate glass, $n_b = 1.5030 \pm 1.0 \times 10^{-4}$ and $1.4984 \pm 1.0 \times 10^{-4}$ respectively, were

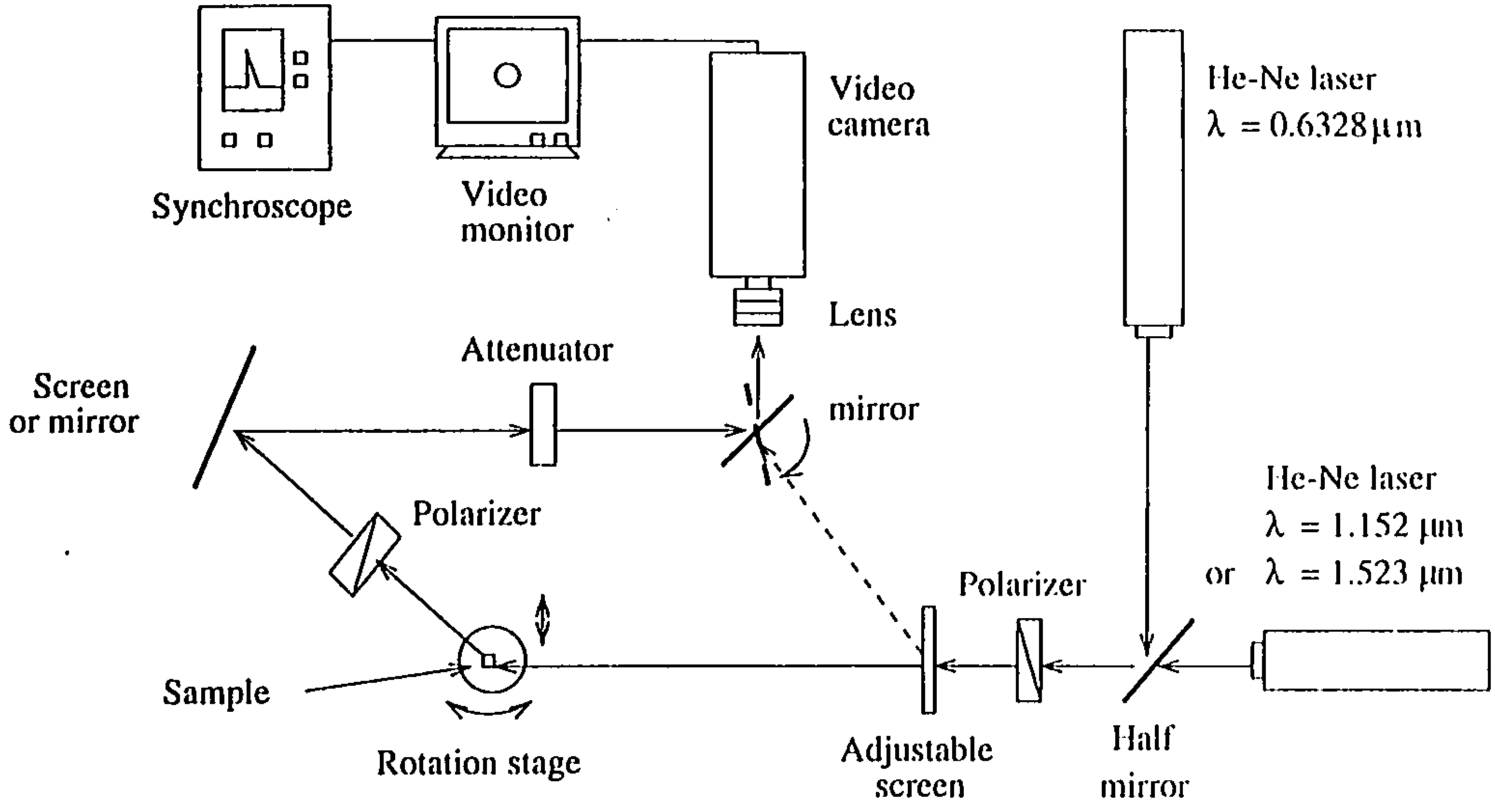

Fig.4.8 The mode indices measurement set-up.

determined by employing the multi-sheet Brewster angle measurement method discussed in Section 4.1. Assuming a gradient index distribution $f(\bar{x})$ in the diffused waveguide

$$n(\bar{x}) = n_b + \Delta n f(\bar{x}). \tag{4.7}$$

The possible functions $f(\bar{x})$ are given by

$$f(\bar{x}) = \begin{cases} exp(-\bar{x}^2) & \text{Gaussian} \\ exp(- \mid \bar{x} \mid) & \text{Exponential} \\ erfc(\bar{x}). & \end{cases}$$

where $\Delta n = n_s - n_b$, $\bar{x} = x/d$, $n_s = n(x = 0^+)$ the index on the surface, and d the effective guide depth such that $n(x = d) = n_b + \Delta n/e$.

After normalization of x-axis by the effective waveguide depth d, the WKB dispersion equation (2.28) for the guided mode M can be re-written as

$$d = \frac{(M + 1/4)\pi + tan^{-1}[\eta_1 \sqrt{(n_e^2 - n_{0-}^2)/(n_{0+}^2 - n_e^2)}]}{k_0 \int_0^{\bar{x}_t} \sqrt{n^2(\bar{x}) - n_e^2} d\bar{x}}, \text{M=0,1,2 ...,} \tag{4.8}$$

where η_1 is given by Eq.(2.26) and $\bar{x}_t$ is the normalized turning point. Employing the measured mode indices and Eq.(4.8), Δn and d can be determined.

Figs.4.9 and 4.10 [7] show the theoretical dispersion curves, using the Gaussian profile, with the measured data at $\lambda = 1.152\mu$m for TE and TM modes respectively. The results at $\lambda = 1.523\mu$m are presented in Figs.4.11 and 4.12 [7] for TE and TM modes respectively. The agreement is excellent. The other two profiles are found to produce a worse fit [7].

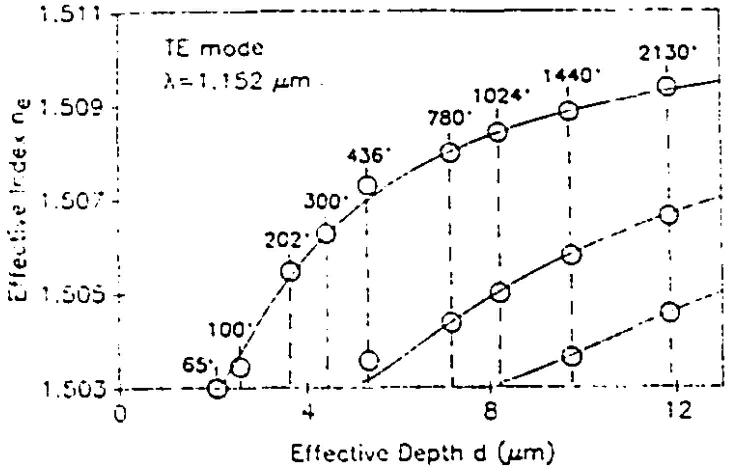

Figure 4.9: Theoretical dispersion curves (Gaussian profile) of the guided TE modes compared with measured mode indices at $\lambda = 1.153\mu m$ for samples made at 385°C. Diffusion times are indicated in minutes. After [7]

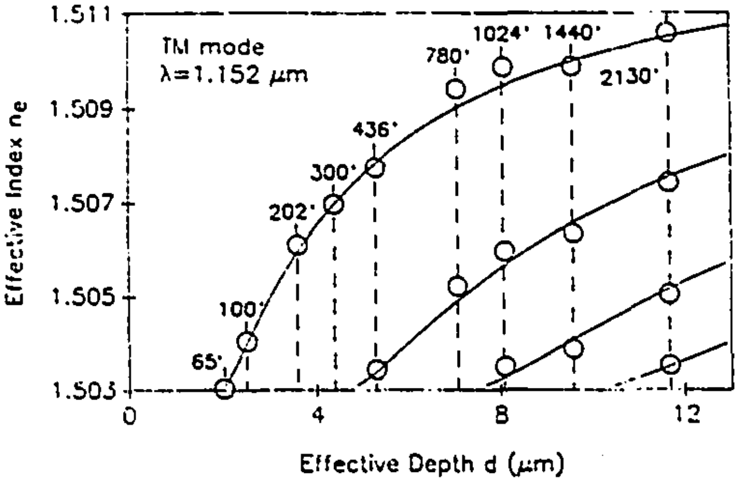

Figure 4.10: Theoretical dispersion curves (Gaussian profile) of the guided TM modes compared with measured mode indices at $\lambda = 1.153\mu m$ for samples made at 385°C. Diffusion times are indicated in minutes. After [7]

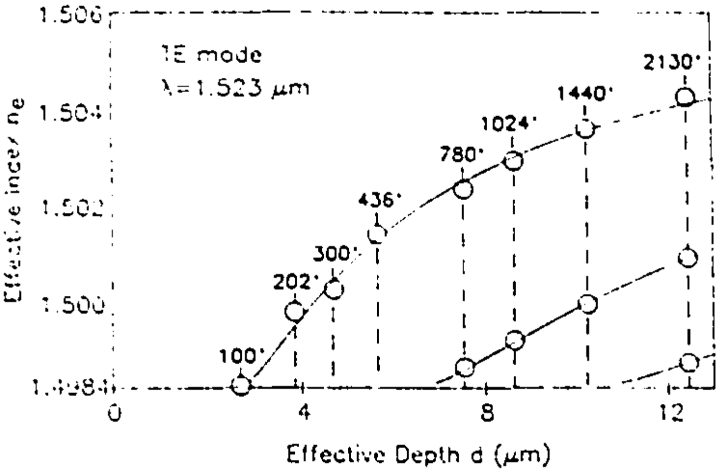

Figure 4.11: Theoretical dispersion curves (Gaussian profile) of the guided TE modes compared with measured mode indices at $\lambda = 1.523\mu m$ for samples made at 385°C. Diffusion times are indicated in minutes. After [7]

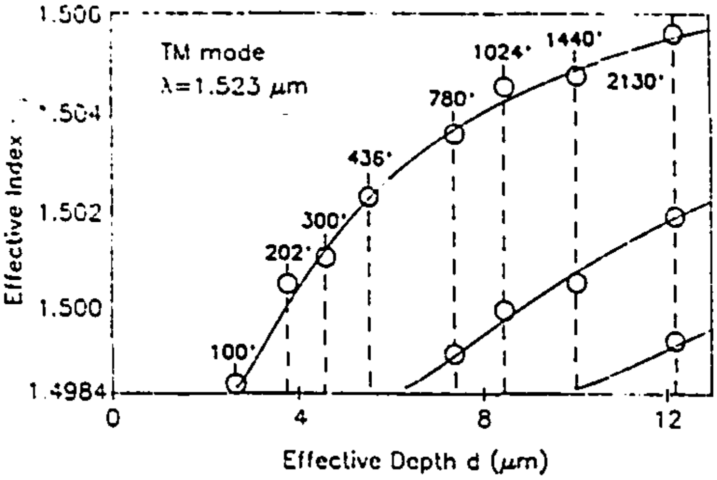

Figure 4.12: Theoretical dispersion curves (Gaussian profile) of the guided TM modes compared with measured mode indices at $\lambda = 1.523\mu m$ for samples made at 385°C. Diffusion times are indicated in minutes. After [7]

Assuming a Gaussian index distribution and plotting effective depth d of different waveguides versus the square root of diffusion time, we have Figs.4.13 and 4.14 [7] for both the TE and TM modes respectively.

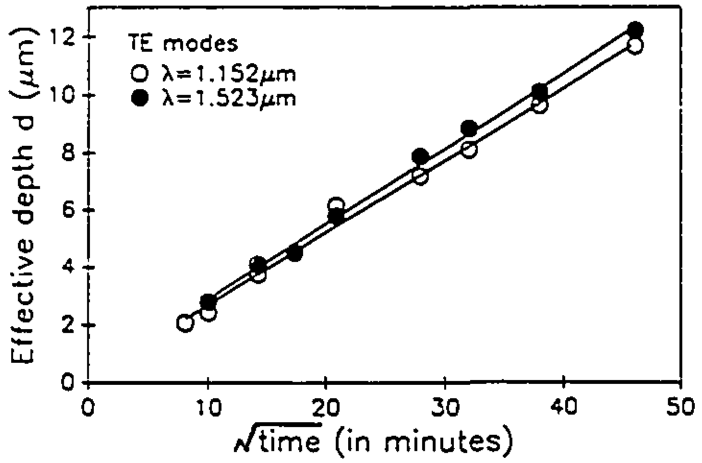

Figure 4.13: The effective guide depth d versus the square root of the diffusion time for the TE modes. After [7]

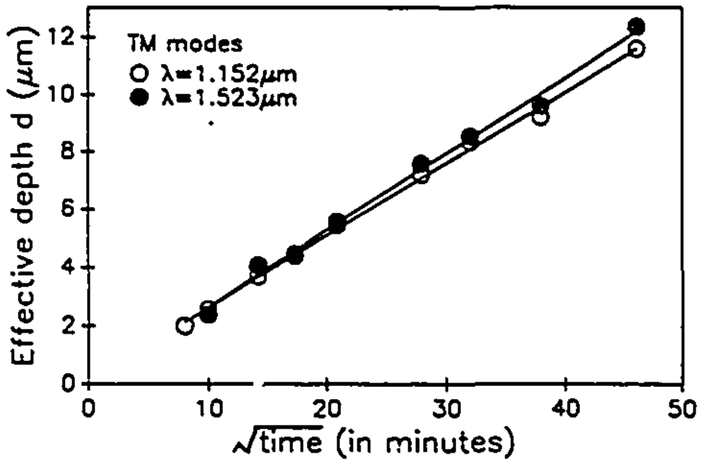

Figure 4.14: The effective guide depth d versus the square root of the diffusion time for the TM modes. After [7]

The solid lines shown in the figures represent results of linear regressions. The good fitting shows that the relation $d = \sqrt{D_e t}$ is again valid for the longer wavelengths as for $\lambda = 0.6328\mu$ m [8], where D_e is the effective diffusion coefficient. The average Δn and D_e for both TE and TM modes and both wavelengths are summarized in Table 4.6. Due to the stress induced birefrgence in a K^+ ion-exchanged waveguide, the differences between TE and TM modes are also shown in the table. The results from different fitting functions are given in Table 4.7 for a typical waveguide sample. The Gaussian function provides the best fit to the measured mode indices, whereas the exponential function the worst.

$\lambda(\mu m)$	Δn^{TE} $(\times 10^{-3})$	Δn^{TM} $(\times 10^{-3})$	D_e^{TE} (m^2/sec) $(\times 10^{-16})$	D_e^{TM} (m^2/sec) $(\times 10^{-16})$
1.152	8.56 ± 0.11	10.05 ± 0.36	10.33	10.04
1.523	8.57 ± 0.26	10.34 ± 0.24	11.53	11.27

Table 4.6: Measured surface index change Δn, and the effective diffusion constants D_e at T=385° C. After [7]

Due to the non-availability of He-Ne laser at $\lambda = 1.31\mu m$, no measurement at this wavelength was made. However, data at $\lambda = 1.31\mu m$ can be determined by interpolation.

m	n_e (Meas.)	n_e (Theor.)			Error $\Delta(\times 10^{-4})$		
		Gaus.	exp.	erfc	Gaus.	exp.	erfc
0	1.5106	1.5105	1.5121	1.5111	0.87	15.66	5.25
1	1.5074	1.5075	1.5079	1.5076	0.43	4.49	1.97
2	1.5050	1.5051	1.5054	1.5052	0.15	3.58	1.93
3	1.5035	1.5034	1.5039	1.5037	1.07	4.25	1.51

Table 4.7: Comparisons of measured TM-mode indices with theoretical values for a sample prepared at T=385°C and t=2130 min. After [7]

4.4 Characterization of Ag$^+$ Ion-exchanged Waveguides

Optical waveguides have been fabricated from silver nitrate melts diluted with sodium nitrate [9]. Depending on the degree of dilution, the surface index change can be adjusted to any specified value between 0 and 0.09. Besides, diluted silver ion-exchange decreases the 'yellow staining' of the glass and reduces the waveguide loss. All these make the diluted silver ion-exchanged waveguide a very good candidate in making integrated optical devices. In Chapter 6, $\Delta n_s = 0.05$ of a diluted Ag+ ion-exchanged waveguide is required in the wavelength demultiplexer. Based on the results reported in [9], a weight ratio of $AgNO_3 : NaNO_3$ of approximately 1:100 is required to achieve this surface index change at T=325°. Although the characterization of Ag^+ ion-exchanged glass waveguides at a visible wavelength has been reported previously [9], similar work at infrared wavelengths is not yet available. Besides, a better characterization can be made with the help of the improved phase shift presented in Section 2.4 for a waveguide with an index truncation which exists in the Ag$^+$ ion-exchanged waveguide.

4.4.1 The methodology

It has been widely accepted that the index profile of a waveguide fabricated from a diluted silver nitrate melt can be described by a second-order polynomial [9] given by

$$n(x) = n_s - \Delta n_s[(\frac{x}{d_o}) + b_o(\frac{x}{d_o})^2] \tag{4.9}$$

where $d_o = \sqrt{D_e t}$ is the profile depth parameter [10] and other parameters are defined in the last section. Both the surface index change Δn_s and the effective diffusion constant D_e depend on the dilution of silver nitrate and diffusion temperature T.

Fig.4.15 gives a sketch of the index profile given by Eq.(4.9), where a sharp index slope change (index truncation) exists at x=d, where d satisfies

$$[(\frac{x}{d_o}) + b_o(\frac{x}{d_o})^2]_{x=d} = 1. \tag{4.10}$$

Here, we choose the constant b$_o$ to be equal to 0.64 as was done in [10]. Then, we have $d = 0.692809551 \times d_o$.

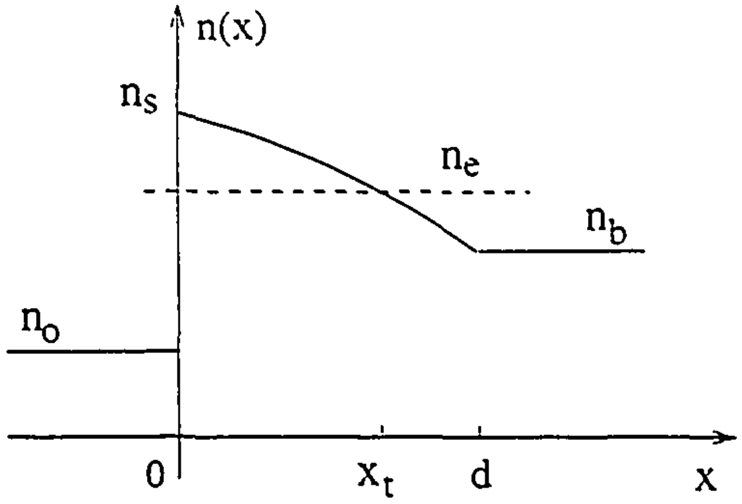

Figure 4.15: A schematic diagram of a silver ion-exchanged planar waveguide index profile (solid lines) with a index truncation at x=d. The dashed line denotes the value of the effective index n_e. The turning point x_t is given by the point of intersection between the dashed line and the solid line.

To find the two unknown parameters in Eq.(4.9), the WKB dispersion relation

$$k_o \int_0^{x_t} \sqrt{n^2(x) - n_e^2}dx = M\pi + tan^{-1}[\eta_1\sqrt{\frac{n_e^2 - n_{0-}^2}{n_{0+}^2 - n_e^2}}] + \phi_t; \quad M = 0, 1, 2, \cdots \tag{4.11}$$

for the guided modes was used. ϕ_t in the above equation is the half phase shift at the turning point x_t. Usually, ϕ_t is taken as a constant $\pi/4$. Since there is an index truncation outside x_t ($x > x_t$ see Fig.4.15), ϕ_t is no longer a constant. The corrected phase shift is given in Eq.(2.46) with

$$\xi = [k_o\sqrt{n_e^2 - n_b^2}(d - x_t)]^{3/2}. \tag{4.12}$$

To obtain the two unknown parameters, n_s and d_o, in a waveguide, at least two modes are needed to yield a pair of dispersion equations with differences in the mode order M. These two equations, then, can be solved by a non-linear root search technique.

4.4.2 Measurement results and discussions

The diluted salt was made of $AgNO_3$ 1.0 : $NaNO_3$ 100.0 in weight ratio. Nine diffused planar waveguide samples were fabricated by immersing soda-lime glass substrates in the molten salt at 325°C for different time durations, 2.5, 3.0, 4.0, 5.0, 10.0, 20.0, 3.0, 40.0, and 60.0 minutes. The effective indices of the guided modes in each sample were obtained by measuring the synchronous angles with a prism coupler. The refractive indices of the prism coupler n_p (flint glass) at $\lambda = 0.6328\mu m$, 1.152μm, and 1.523μm are 1.77862, 1.75231, and 1.74486, respectively. The corresponding indices for the substrate glass n_b are 1.5125, 1.5030, and 1.4984 respectively.

Fig.4.16 [11] shows the surface index change versus the diffusion time for TE modes at $\lambda = 0.6328\mu m$. The independence of Δn_s on diffusion time can be clearly seen. Similar results are also true at other wavelengths for both polarizations. We took averages of n_s among the samples (multi-mode) for different wavelengths and polarizations as listed in Table 4.8 [11].

According to the calibrated results in [9] at $\lambda = 0.6238\mu m$, the surface index change is 0.05 which is very close to our results. The results in Table 4.8 also show that there is almost no birefringence in diluted silver ion-exchanged waveguides which is different from the waveguides made by K^+-ion exchange. It is worth pointing out that the results are less accurate at longer wavelengths because there are fewer multimode samples.

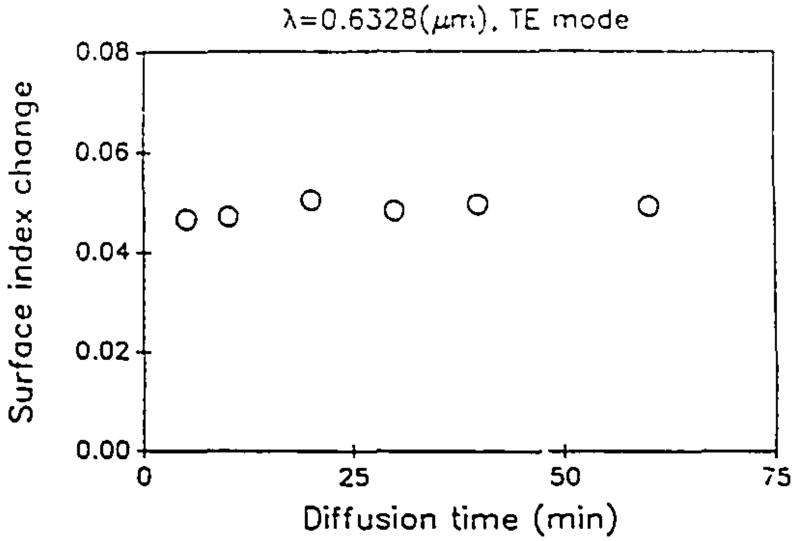

Figure 4.16: The surface index change dependence on the diffusion time for TE modes at $\lambda = 0.6328\mu m$ at 325°C.

$\lambda(\mu m)$	0.6328	1.152	1.523
TE	0.049	0.048	0.046
TM	0.049	0.048	0.048

Table 4.8: Measured average surface index changes at 325°C

With n_s known, we can obtain the dispersion curves for different modes by the modified WKB method. Plotting the measured effective indices together with the dispersion curves, we have Figs.4.17, 4.18, and 4.19 [11] as illustrations.

Fig.4.17 show that the results obtained by either WKB or MWKB are very close in multi-mode regions. But near cutoffs, the measured results are closer to the curves obtained by MWKB. Figs.4.18 and 4.19 have been enlarged in comparison with Fig.4.17 for a closer look at the single mode regions. The curves obtained by MWKB obviously provide a much better fitting.

Figs.4.20 and 4.21 [11] indicate the relation between the normalized waveguide depth and the square root of the diffusion time. They are linearly dependent as expected. The slopes of the best fitted lines for both the TE and TM polarizations at the three wavelengths are given in Table 4.9. We can see also in Figs.4.20 and 4.21 that the fitting lines almost pass through the origin. Similar results are also true in other wavelengths. The results in Table 4.9 are accurate to the first decimal place and yield approximately 1.5. According to results presented in [9] $\sqrt{D_r} = 1.58$ $(\mu m/\sqrt{min})$. Our values are slightly smaller.

$\lambda(\mu m)$	0.6328	1.152	1.523
TE mode	1.497	1.450	1.494
TM mode	1.531	1.480	1.509

Table 4.9: Measured square root of diffusion coefficients $(\mu m/\sqrt{min})$.

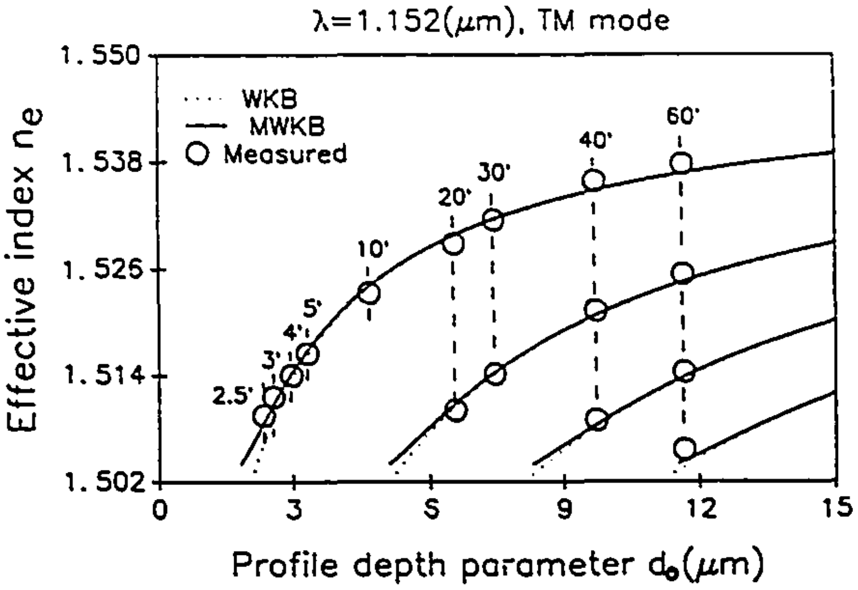

Figure 4.17: Theoretical dispersion curves, — MWKB and ····· WKB, of guided TM modes are compared with measured mode indices at $\lambda = 1.152\mu m$ for samples made for different time durations (in minute) at 325°C.

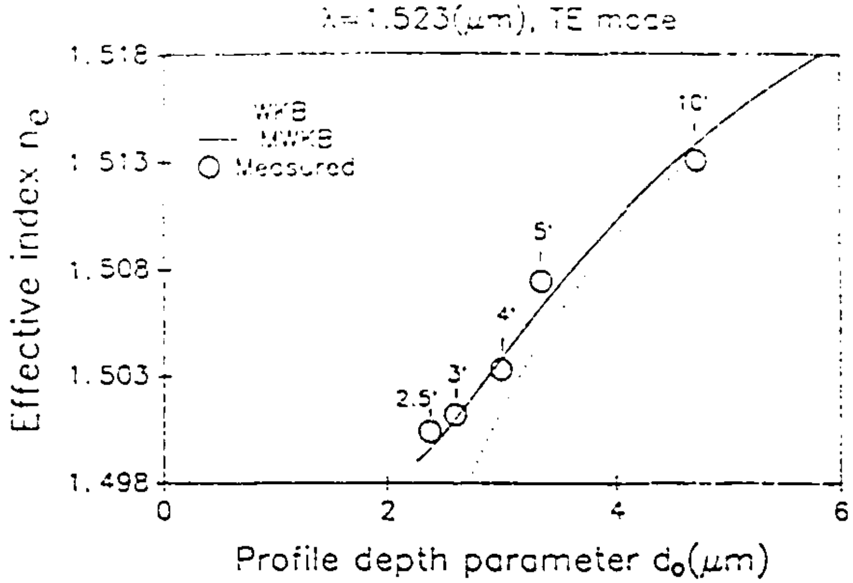

Figure 4.18: Theoretical dispersion curves, —— MWKB and ····· WKB, of guides modes are compared with measured mode indices at $\lambda = 1.523\mu m$ for TE modes for single mode samples at 325°C.

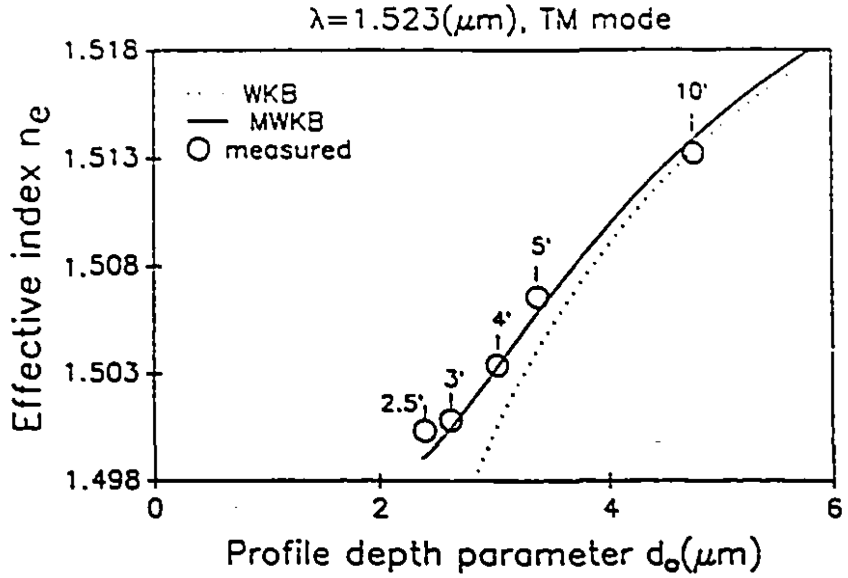

Figure 4.19: See the caption of Fig.4.18 but for TM modes.

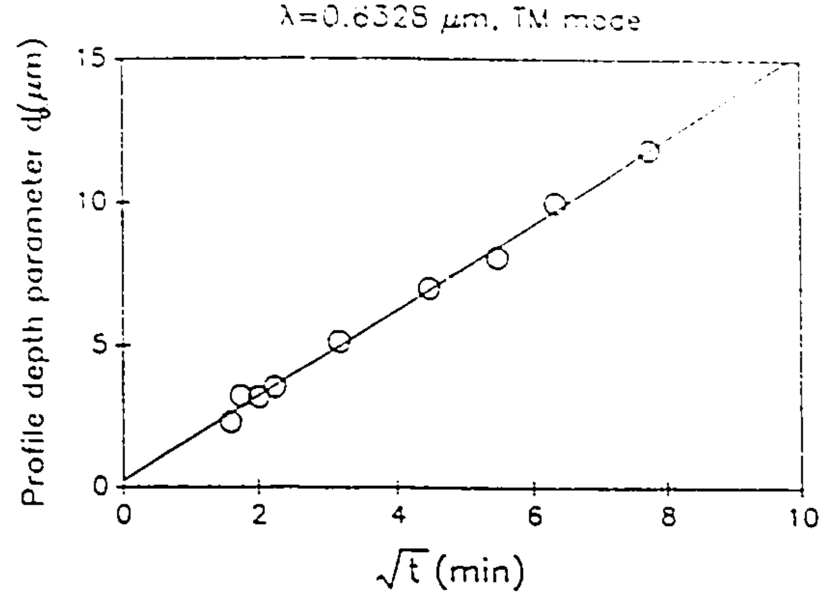

Figure 4.20: Index profile depth parameter versus square root of diffusion time at $\lambda = 0.6328\mu m$ for TM modes.

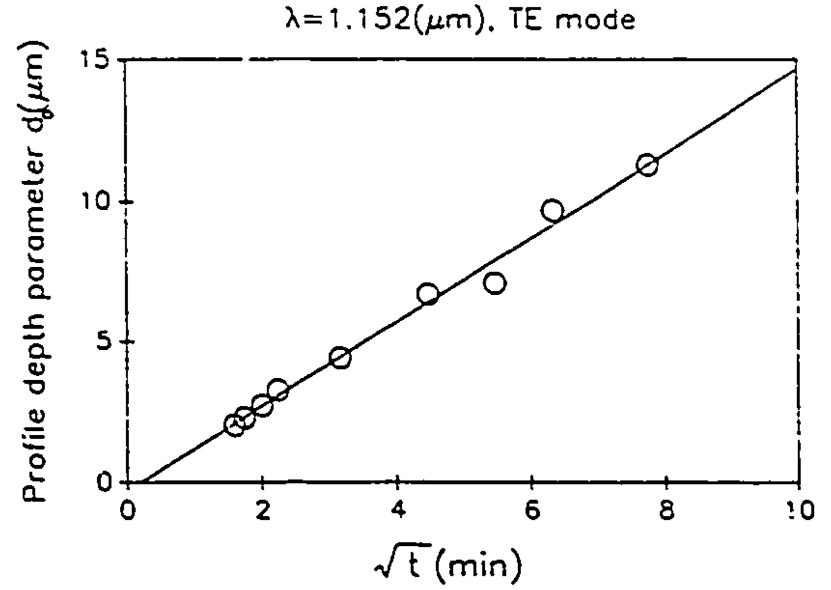

Figure 4.21: Index profile depth parameter versus square root of diffusion time at $\lambda = 1.152\mu m$ for TE modes.

Bibliography

[1] *Optical Materials*, Optics Guide 4 (Melles Griot Corporation, Irvine, Calif. 1988), pp.3-10.

[2] F. Xiang and G.L. Yip,"Simple technique for determining substrate indices of isotropic materials by a multisheet Brewster angle measurement", Applied Optics, vol. 31, No. 36, pp.7570-7574, December 1992.

[3] W.H. Press, B.P. Flannery, S.A. Tenkolsky, and W.T. Vetterling, *Numerical Recipes* (Cambridge U. Press, New York, 1986), Chap. 7, pp.191-225.

[4] C.W. Pitt,"Sputtering-glass optical waveguides", Electron. Lett., vol.9, No.17, pp.401-403, 1973.

[5] P.K. Tien and R. Ulrich,"Theory of prism-film coupler and thin-film light guides", J. of the Opt. Soc. Am., vol.60, No.10, pp.1325-1337, 1970.

[6] I.H. Malitson,"Refraction and dispersion of synthetic sapphire", J. of the Opt. Soc. of Am., vol.52, p.1377-1379, 1962.

[7] G.L. Yip, K. Kishioka, F. Xiang, and J.Y. Chen, "Characterization of planar optical waveguides by K^+-ion exchange in glass at 1.152 and 1.523 μm", SPIE Proceedings, vol.1583, pp.14-18, 1991.

[8] G.L. Yip and J. Albert,"Characterization of planar optical waveguides by K^+-ion exchange in glass", Opt. Letters, vol. 101, pp.151-153, March 1985.

[9] G. Stewart and P.J.R. Laybourn, "Fabrication of ion-exchanged optical waveguides from dilute silver nitrate melts", IEEE J. Quantum Elec., vol.QE-14, pp.930-934, 1978.

[10] G. Stewart, C.A. Millar, P.J.R. Laybourn, C.D.W. Wilkinson, and R.M. Delarue, "Planar optical waveguides formed by silver-ion migration in glass", IEEE J. Quantum Elec., vol.QE-13, pp.192-200, 1977.

[11] F. Xiang, K.H. Chen, and G.L. Yip, "The application of an improved WKB method to the characterization of diluted silver ion-exchanged glass waveguides in the near infrared", SPIE Proceedings, vol.1794, pp.40-47, 1992.

Chapter 5

An Al_2O_3 Strip Loaded Y-branch WDM for $\lambda = 1.55$ and $1.31\mu m$ by K^+-Na^+ Ion-exchange in Glass

5.1 Introduction

The objective of this work is to design and fabricate a Y-junction WDM for λ=1.31 and 1.55μm as shown in Fig.5.1. Its waveguides are made by K^+ ion-exchange with its arm 2 cladded by an Al_2O_3 layer. The demultiplexing is based on mode transformation from the fundamental mode in the input waveguide to the local fundamental mode of the 5-layer branch structure and the difference in the dispersion characteristics of the two dissimilar branches. For efficient demultiplexing, a large difference between the effective indices of the two branches is desirable based on the conclusions drawn in Chapter 3. It can be achieved by a waveguide asymmetry, consisting of two branches with a different height and width. The extinction ratio (ER), defined by the ratio of both the fundamental modal powers from the two infinitely separated branches, can be further enhanced by an Al_2O_3 layer over one branch (branch 2).

The design was first proposed in [1]. However, it is far from being optimized and little progress has been made to achieve reasonable extinction ratios experimentally since then. According to our knowledge, the values of ER measured from a real device have not been over 10db at both wavelengths. The problems were mainly due to a non-optimized mask design and the difficulties in fabricating the Al_2O_3 cladded waveguide. In order to overcome the difficulties, the device structure and its fabrication process have to be modified for improvement. Here, we present the analysis and design optimization of the device by the beam propagating method (BPM). According to the BPM results, our new design provides ERs over 20dB at both wavelengths with a generally realizable fabrication tolerance.

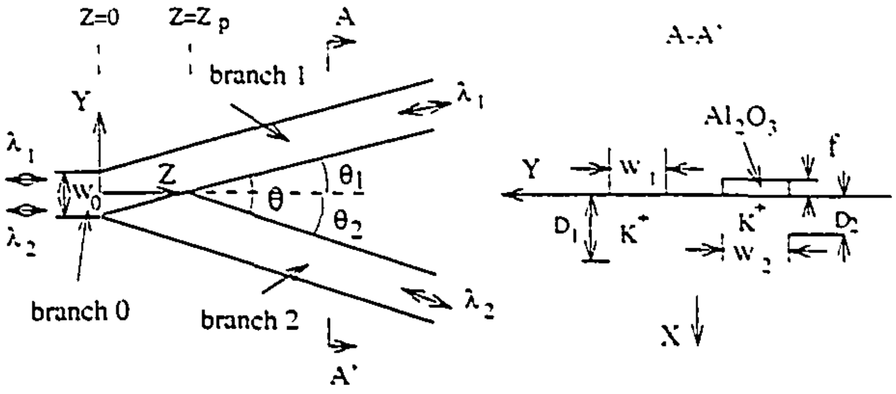

Top view

Section view

Figure 5.1: The configuration of a Y-junction demultiplexer, where $\lambda_1 = 1.55\mu m$, $\lambda_2 = 1.31\mu m$.

The fabrication process has also been modified mainly for controlling the Al_2O_3 cladding thickness. There are three major fabrication steps to make a device. They are, (1) making the deeper K^+ ion-exchanged waveguides, branch 0, branch 1, and the part of the taper not covered with Al_2O_3; (2) making the shallower K^+ ion- exchanged branch 2; and (3) sputter-depositing an Al_2O_3 cladding layer on top of branch 2. The details will be given in Section 4. The measured results are much improved from those already reported [1]. The discussions will be given in the final section.

5.2 Principle of Operation

An asymmetric Y-branch with a small branch angle acts like a mode splitter as we have discussed in Chapter 3. Assume that the incoming light from branch 0 to be in the fundamental mode. The modal structure will be preserved before the branching because of the adiabatic invariance in the slow change taper region. Then, this mode power will be gradually transferred to one branch arm which has the higher effective index with the increase of the branch separation. To achieve demultiplexing for two wavelengths $\lambda_1 = 1.55\mu m$ and $\lambda_2 = 1.31\mu m$, it is required that the effective index of branch 1 is higher than that of branch 2 at λ_1 and lower at λ_2 assuming the light at λ_1 is designed to come out from branch 1 and the other from branch 2. As a result, there must be an intersection of two branches' dispersion curves between the two wavelengthes when the two branches are infinitely separated as shown in Fig.5.2.

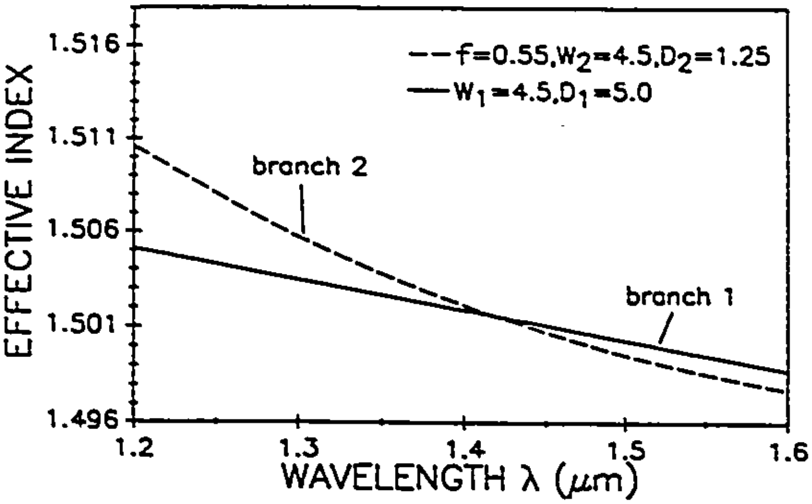

Figure 5.2: Dispersion curves of TM mode in both branch 1 and branch 2 when they are completely separated. The parameters are given in μm.

In general, the larger the difference of the effective indices between the two branches, the higher the ER. The use of an Al_2O_3 cladding layer reduces the required depth of branch 2, D_2, and hence increases the asymmetry between the two branches in the waveguide geometry and the effective indices. The dispersion curve for branch 2 becomes steeper, leading to a large effective index difference between the two branches.

To transfer the input light power into its destined branch, a branch region $(z \geq z_b)$ is needed, which acts as a mode splitter. Branch 0 is designed as a single mode waveguide with the same width as that of branch 1. A taper region $(0 \leq z \leq z_b)$ is inserted to depress local high-order modes as indicated in Fig.5.1. The ER is strongly dependent on the branch angle θ. If θ is not small enough, the branch will act as a power divider instead of a mode splitter. The limit of θ is given in Eq.(3.14). In the following, we assume that all the branch angles θ satisfy Eq.(3.14). The indices of Al_2O_3 sputtering layer are given in Table 4.4 after the target voltage of the sputtering were set to 0.75 kv.

5.3 BPM Analysis and Design Optimization

The effective index method has been used to simplify the device from a three-dimensional problem to a two-dimensional problem before the BPM is used. For the waveguides made by the first K^+ ion-exchange, the WKB dispersion equation (2.28) is used to calculate n'_{eff} of the slab waveguide $(\partial/\partial y = 0)$ with D_1 as the waveguide depth. The index profile of this slab waveguide is assumed to be Gaussian as discussed in Chapter 4. For the Al_2O_3 cladded waveguide, the dispersion equation (2.36) will be used to find n''_{eff}. Again, the K^+ ion-exchanged shallow waveguide index profile is Gaussian. Then, the device can be approximated by a slab-branch structure as shown in Fig.3.1 where all the equivalent indices are wavelength dependent and all the index dependence along y are assumed to be step-like.

The BPM can, now, be applied to solve this two-dimensional problem. Tremendous computing time can be saved in the BPM simulation employing a two-dimensional formulation instead of a three-dimensional one. On the other hand, the only large index discontinuity appears on the waveguide surface. This discontinuity can be easily considered in the WKB method such that a structure with a very small index change is left for analysis by the BPM. This is especially good when a vector BPM was not yet available. For this historic reason, only the FTT-BPM were used and will be presented in this chapter. The BPM window was 100μm wide, the transverse grid size was 100/512 μm, and the propagation step size was 2μm. The fundamental eigenfunction was input at z=0 as shown in Fig.5.1. The output powers (fundamental modes only) from two branches are calculated at where the separation is sufficient large, for example 20μm.

The extinction ratios were calculated by using the following definition

$$ER = \begin{cases} 10log_{10}(\frac{P_1}{P_2}) & \text{for } \lambda_1 \\ 10log_{10}(\frac{P_2}{P_1}) & \text{for } \lambda_2 \end{cases} \tag{5.1}$$

where P_1 and P_2 are the powers of the fundamental mode in branch 1 and branch 2 respectively. In the calculations, all the media were assumed to be lossless. The power from its designed branch in the fundamental mode is considered as the received power, i.e. P_1 or P_2. The other power is taken as loss, which includes the reflected power, the scattered power, the power going into another branch, and the power carried by higher-order modes. Here, we call this loss a device loss, which can be expressed by

$$\text{device loss} = \begin{cases} 10log_{10}(\frac{P_0-P_1}{P_0}) & \text{for } \lambda_1 \\ 10log_{10}(\frac{P_0-P_2}{P_0}) & \text{for } \lambda_2 \end{cases} \tag{5.2}$$

where P_0 is the input power.

5.3.1 ER dependence on the branch angle

Although, in Chapter 3, it has been demonstrated that the performance of a mode splitter strongly depends on its branch angle, a detailed analysis of ER with respect to the branch angle by the BPM for a Y-branch is still necessary.

The curves of ER versus the branch angle θ are presented in Fig.5.3 for a device sample described in the figure caption. The ERs are seen to be strongly dependent on θ. The oscillation of ER between $\theta = 0.008$ and 0.02 rad is due to the strong coupling coefficient $c_{2,1}$ (see Chapter 3) which competes with $c_{1,2}$. Since our interests are out of this region ($\theta < 0.008$ rad), this phenomenon will not be encountered and, hence, not discussed here (see [2] for details). It is necessary for θ to be less than 0.008 rad in order to achieve the ERs over 20dB at both wavelengths. During fabrication, two masks are required for making the branches with two different depths. The branch angle is formed by these two masks. θ=0.005 rad is chosen in our design, which can be achieved by a careful mask alignment. If θ = 0.003 rad is chosen, the ERs are certainly higher but the resulting device must also be longer.

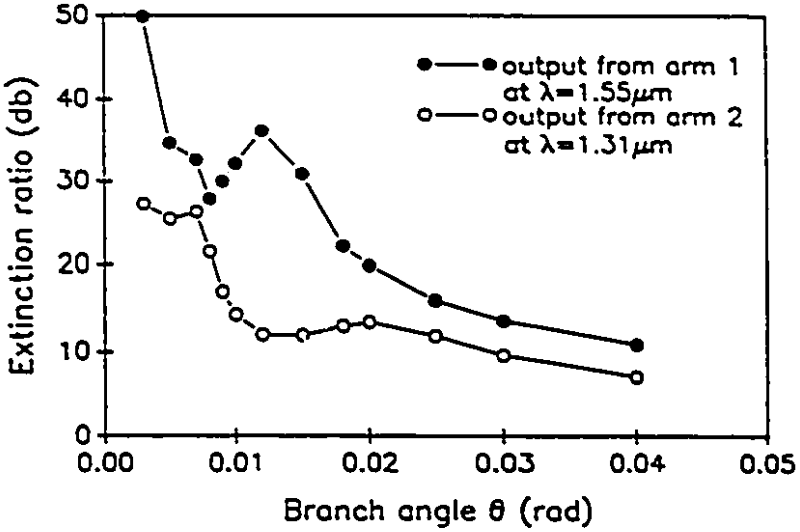

Figure 5.3: The dependence of ER on the branch angle θ, where $\theta_1 = \theta_2 = \theta/2$, $W_1=W_2=W_0 = 4.5\mu m$, $D_1 = 5.0\mu m$, $D_2 = 1.0\mu m$, and $f=0.55\mu m$.

The results in Fig.5.3 also show that the ER at $\lambda = 1.55\mu m$ is always higher than that at $\lambda = 1.31\mu m$ for $\theta_2 = \theta/2$. Since branch 1 is the same waveguide as the main branch, retaining the power in branch 1 at $\lambda = 1.55\mu m$ is easier than transferring it into branch 2 at $\lambda = 1.31\mu m$ when $\theta_2 = \theta/2$. To reduce the unequal ER between the two branches, bending branch 1 further away from branch 0 or straightening branch 2 along the main branch should help.

Fig.5.4 shows the curves of the ER versus θ_1 (θ kept constant) for both wavelengths for a sample described in the figure caption. The results show that the ER increases at λ=1.31μm but decreases at λ=1.55 μm with θ_1 increasing as expected. By setting $\theta_2 = 0$ ($\theta_1 = 0.005$), the ER at λ=1.31 μm is increased by 8dB to 33dB while that at λ=1.55 μm is decreased by 5dB to 30dB from the figure when $\theta_2 = \theta/2$. Besides, straightening branch 2 also compensates the field mismatch due to the depth discontinuity from branch 0 to branch 2 with a much smaller effective depth.

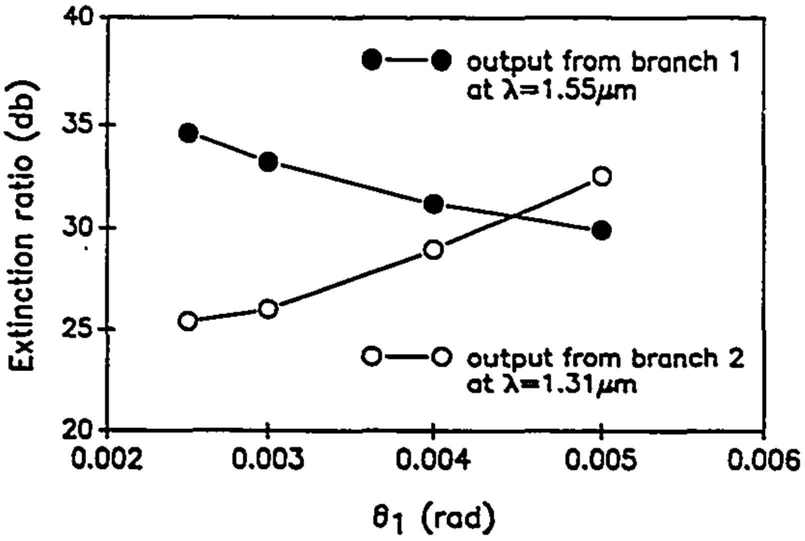

Figure 5.4: The dependence of ER on the angle θ_1, where $\theta = 0.005$ rad, $\theta_1 = \theta - \theta_2$, $W_1 = W_2 = W_0 = 4.5\mu m$, $D_1 = 5.0\mu m$, $D_2 = 1.0\mu m$, and $f = 0.55\mu m$.

5.3.2 ER dependence of the effective index difference

Another important parameter which affects the performance of the mode splitter is the difference of the effective indices between the two branches when they are infinitely separated.

To discuss its effect on the ER, we fix the parameters for all the branch structures with $W_0 = W_1 = W_2$, $\theta_2 = 0$, and $\theta = 0.005$ rad as shown in Fig.5.1. In the following, where there are two subscript numbers, the first indicates the order of the wavelength and the second is for the branch number. We define the effective index differences of the two separated branches as

$$\Delta n_{e1} = n_{e11} - n_{e12} \qquad \text{for } \lambda_1 = 1.55\mu m \tag{5.3}$$

$$\Delta n_{e2} = n_{e22} - n_{e21} \qquad \text{for } \lambda_2 = 1.31\mu m \tag{5.4}$$

where n_{e11} and n_{e12} are the branch 1 and branch 2's effective indices, respectively, at λ_1 and n_{e21} and n_{e22} are those at λ_2.

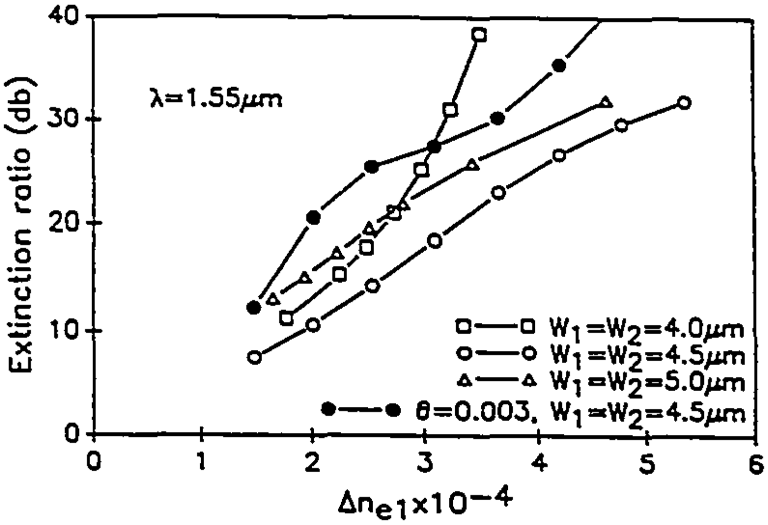

Figure 5.5: Extinction ratio versus the effective index difference between the two output branches at $\lambda_1 = 1.55\mu m$. The device parameters are given in the text.

At $\lambda_1 = 1.55\mu m$, fixing n_{eff12} at 1.500 while changing n_{eff11}, we have calculated the ERs which are plotted in Fig.5.5 versus the effective index difference Δn_{e1}. At $\lambda_2 = 1.31\mu m$, fixing n_{eff21} at 1.504 while changing n_{eff22}, we have also calculated the ERs which are plotted in Fig5.6 versus the effective index difference. As we can see in both figures, the ERs increase with the increase of the effective index differences. ERs are over 20db only when $\Delta n_{e1} > 0.00033$ at λ_1 and $\Delta n_{e2} > 0.00057$ at λ_2. These two values are important and will be taken as the criteria for the design optimization later on.

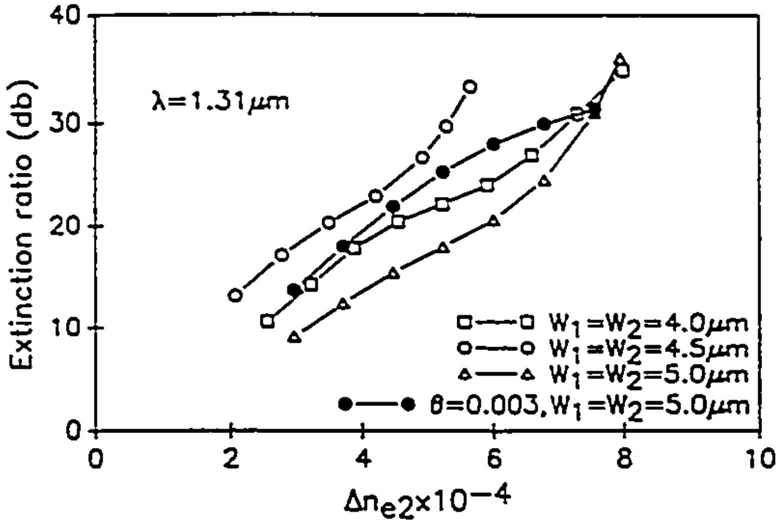

Figure 5.6: Extinction ratio versus the effective index difference between the two output branches at $\lambda_2 = 1.31\mu m$. The device parameters are given in the text.

5.3.3 The optimized design

With the criteria established above, the optimization is simplified. We simply calculate the individual branch's effective index to check the device performance instead of calculating the ER every time. The parameters which can be adjusted for the optimization are W_1 the width of branch 1, W_2 the width of branch 2, D_1 the depth of branch 1, D_2 the depth of branch 2, and Al_2O_3 film thickness f. For a further simplification, we set $W_1 = W_2 = W_0$. Then, the waveguide effective index differences between the two infinitely separated branches were calculated for different widths, depths, and thicknesses at the two wavelengths. The results are presented in Tables.5.1 -5.9 for the combinations of three D_2 (1.0μm, 1.5μm, and 2.0μm) and three W (4.0μm, 4.5μm, and 5.0μm). In these tables, the effective index differences are given by Eqs.(5.3) and (5.4), " c " indicates that branch 1 is cutoff, " n " indicates that the effective difference as defined by Eqs.(5.3) and (5.4) is negative, and the double lines mark the boundaries over which branch 2 will support a second-order mode at λ_2 with a further increase in f. Although the side-diffusion of ion-exchange may not be important in the design, it can not be completely ignored. It is hard to make a deep waveguide, for example $D_1 = 6.0\mu m$, with a narrow width of the mask window, for example $W_0 = 4.0\mu m$, by purely thermal ion-exchange. Here, it is assumed that $D_1 \leq W_0 + 1.0\mu m$.

Thus, we indicate the enclosed regions in highlight in the tables that present the designs having the ERs over 20db for both the wavelengths and satisfying the conditions mentioned above. The tables show that the ERs are very sensitive to the Al_2O_3 film thickness f. To provide the ERs over 20db, f has to be accurate up to about $0.01\mu m$ which is very difficult to control. Compared with all the sizes of the enclosed regions in the tables, the areas in Tables 5.2 and 5.5 are the two bigest. If the parameters of the device are chosen from the middle of the two enclosed regions, the design should be close to the optimized one. In these regions, the parameters provide the largest fabrication tolerance for the ERs over 20db at both the wavelengths. But its ERs are not necessarily the highest ones. This near-optimized design is $D_1 = 5.0 \pm 0.5\mu m$, $W_0 = W_1 = W_2 = 4.5 \pm 0.5\mu m$, $D_2 = 1.25 \pm 0.25\mu m$, and $f = 0.55 \pm 0.01\mu m$.

f	λ	D_1=3.5	4.0	4.5	5.0	5.5	6.0
0.52	1.55	0.274	0.549	0.846	1.138	1.414	1.670
	1.31	1.123	0.713	0.327	n	n	n
0.53	1.55	0.254	0.529	0.826	1.118	1.394	1.650
	1.31	1.564	1.154	0.768	0.419	0.105	n
0.54	1.55	0.218	0.493	0.790	1.082	1.352	1.614
	1.31	2.052	1.641	1.256	0.907	0.593	0.313
0.55	1.55	0.163	0.438	0.735	1.027	1.303	1.559
	1.31	2.583	2.173	1.787	1.438	1.124	0.844
0.56	1.55	0.082	0.357	0.654	0.946	1.222	1.478
	1.31	3.158	2.748	2.362	2.013	1.699	1.419
0.57	1.55	n	0.248	0.545	0.837	1.113	1.369
	1.31	3.772	3.362	2.976	2.627	2.313	2.033
0.58	1.55	n	0.108	0.405	0.697	0.973	1.229
	1.31	4.224	4.012	3.626	3.277	2.963	2.683

Table 5.1: A chart of Δn_{e1} and Δn_{e2} ($\times 10^{-3}$) distributions versus D_1 and f for D_2=1.0μm and W_0=4.0μm. The parameters, λ, D_1, and f, are all in μm

f	λ	D_1=3.5	4.0	4.5	5.0	5.5	6.0
0.52	1.55	0.325	0.639	0.973	1.296	1.600	1.879
	1.31	1.218	0.769	0.351	n	n	n
0.53	1.55	0.300	0.614	0.948	1.271	1.575	1.854
	1.31	1.689	1.240	0.822	0.447	0.112	n
0.54	1.55	0.257	0.571	0.905	1.228	1.532	1.811
	1.31	2.206	1.757	1.339	0.964	0.629	0.332
0.55	1.55	0.190	0.504	0.838	1.161	1.465	1.744
	1.31	2.767	2.318	1.900	1.525	1.190	0.893
0.56	1.55	0.096	0.410	0.744	1.067	1.371	1.650
	1.31	3.370	2.921	2.503	2.128	1.793	1.496
0.57	1.55	n	0.283	0.671	0.940	1.244	1.523
	1.31	4.011	3.562	3.144	2.769	2.434	2.137
0.58	1.55	n	0.122	0.456	0.779	1.083	1.362
	1.31	4.688	4.239	3.821	3.446	3.111	2.814

Table 5.2: A chart of Δn_{e1} and Δn_{e2} ($\times 10^{-3}$) distributions versus D_1 and f for D_2=1.0μm and W_0=4.5μm. The parameters, λ, D_1, and f, are all in μm

f	λ	D_1=3.5	4.0	4.5	5.0	5.5	6.0
0.50	1.55	c	c	c	c	c	c
	1.31	0.454	n	n	n	n	n
0.51	1.55	c	c	c	c	c	c
	1.31	0.850	0.368	n	n	n	n
0.52	1.55	0.373	0.724	1.090	1.441	1.767	2.066
	1.31	1.297	0.815	0.371	n	n	n
0.53	1.55	0.344	0.695	1.061	1.412	1.738	2.037
	1.31	1.791	1.309	0.865	0.469	0.116	n
0.54	1.55	0.293	0.644	1.010	1.361	1.687	1.986
	1.31	2.332	1.850	1.406	1.010	0.657	0.346
0.55	1.55	0.216	0.567	0.933	1.284	1.610	1.909
	1.31	2.915	2.433	1.989	1.593	1.240	0.929
0.56	1.55	0.107	0.458	0.824	1.175	1.501	1.800
	1.31	3.540	3.058	2.614	2.218	1.865	1.554
0.57	1.55	n	0.316	0.682	1.033	1.359	1.658
	1.31	4.203	3.721	3.277	2.881	2.528	2.217

Table 5.3: A chart of Δn_{e1} and Δn_{e2} ($\times 10^{-3}$) distributions versus D_1 and f for D_2=1.0μm and W_0=5.0μm. The parameters, λ, D_1, and f, are all in μm

f	λ	D_1=3.5	4.0	4.5	5.0	5.5	6.0
0.51	1.55	0.131	0.406	0.703	0.995	1.271	1.527
	1.31	1.571	1.161	0.775	0.426	0.112	n
0.52	1.55	0.067	0.342	0.639	0.931	1.207	1.463
	1.31	1.976	1.566	1.180	0.831	0.517	0.237
0.53	1.55	n	0.262	0.559	0.851	1.127	1.383
	1.31	2.420	2.010	1.624	1.275	0.961	0.681
0.54	1.55	n	0.163	0.460	0.752	1.028	1.284
	1.31	2.902	2.493	2.107	1.758	1.444	1.164
0.55	1.55	n	0.043	0.340	0.632	0.908	1.164
	1.31	3.424	3.014	2.628	2.279	1.965	1.685
0.56	1.55	n	n	0.197	0.489	0.765	1.021
	1.31	3.983	3.573	3.187	2.838	2.524	2.244
0.57	1.55	n	n	0.029	0.321	0.597	0.853
	1.31	4.577	4.167	3.781	3.432	3.118	2.838
0.58	1.55	n	n	n	0.127	0.403	0.659
	1.31	5.205	4.795	4.409	4.060	3.746	3.466

Table 5.4: A chart of Δn_{e1} and Δn_{e2} ($\times 10^{-3}$) distributions versus D_1 and f for D_2=1.5μm and W_0=4.0μm. The parameters, λ, D_1, and f, are all in μm

f	λ	D_1=3.5	4.0	4.5	5.0	5.5	6.0
0.49	1.55	0.254	0.568	0.902	1.225	1.529	1.808
	1.31	0.956	0.507	0.089	n	n	n
0.50	1.55	0.210	0.524	0.858	1.181	1.485	1.764
	1.31	1.307	0.858	0.440	0.065	n	n
0.51	1.55	0.153	0.467	0.801	1.124	1.428	1.707
	1.31	1.696	1.247	0.829	0.454	0.119	n
0.52	1.55	0.079	0.393	0.727	1.050	1.354	1.633
	1.31	2.126	1.677	1.259	0.884	0.549	0.252
0.53	1.55	n	0.299	0.633	0.956	1.260	1.539
	1.31	2.595	2.146	1.728	1.353	1.018	0.721
0.54	1.55	n	0.186	0.520	0.848	1.147	1.426
	1.31	3.103	2.654	2.236	1.861	1.549	1.229
0.55	1.55	n	0.048	0.382	0.705	1.009	1.288
	1.31	3.648	3.199	2.781	2.406	2.071	1.774
0.56	1.55	n	n	0.221	0.544	0.848	1.127
	1.31	4.231	3.782	3.364	2.989	2.654	2.237

Table 5.5: A chart of Δn_{e1} and Δn_{e2} ($\times 10^{-3}$) distributions versus D_1 and f for D_2=1.5μm and W_0=4.5μm. The parameters, λ, D_1, and f, are all in μm

f	λ	D_1=3.5	4.0	4.5	5.0	5.5	6.0
0.48	1.55	0.327	0.678	1.044	1.395	1.721	2.020
	1.31	0.689	0.207	n	n	n	n
0.49	1.55	0.290	0.641	1.007	1.358	1.684	1.983
	1.31	1.020	0.538	0.094	n	n	n
0.50	1.55	0.239	0.590	0.956	1.307	1.633	1.932
	1.31	1.340	0.908	0.464	0.068	n	n
0.51	1.55	0.172	0.523	0.889	1.240	1.566	1.865
	1.31	1.799	1.317	0.873	0.477	0.124	n
0.52	1.55	0.088	0.439	0.805	1.156	1.482	1.781
	1.31	2.248	1.766	1.322	0.926	0.573	0.262
0.53	1.55	n	0.334	0.700	1.051	1.377	1.676
	1.31	2.737	2.255	1.811	1.415	1.062	0.751
0.54	1.55	n	0.206	0.572	0.923	1.249	1.548
	1.31	3.264	2.782	2.338	1.942	1.589	1.278
0.55	1.55	n	0.053	0.419	0.770	1.096	1.395
	1.31	3.828	3.346	2.902	2.506	2.153	1.842

Table 5.6: A chart of Δn_{e1} and Δn_{e2} ($\times 10^{-3}$) distributions versus D_1 and f for D_2=1.5μm and W_0=5.0μm. The parameters, λ, D_1, and f, are all in μm

f	λ	D$_1$=3.5	4.0	4.5	5.0	5.5	6.0
0.49	1.55	n	0.213	0.510	0.802	1.078	1.334
	1.31	1.529	1.119	0.733	0.384	0.070	n
0.50	1.55	n	0.141	0.438	0.730	1.006	1.262
	1.31	1.852	1.442	1.056	0.707	0.393	0.113
0.51	1.55	n	0.056	0.353	0.645	0.921	1.177
	1.31	2.209	1.799	1.413	1.064	0.750	0.470
0.52	1.55	n	n	0.255	0.547	0.823	1.079
	1.31	2.601	2.191	1.805	1.456	1.142	0.862
0.53	1.55	n	n	0.141	0.433	0.709	0.965
	1.31	3.029	2.619	2.233	1.884	1.570	1.290
0.54	1.55	n	n	0.011	0.303	0.579	0.835
	1.31	3.493	3.083	2.697	2.348	2.034	1.754
0.55	1.55	n	n	n	0.155	0.431	0.687
	1.31	3.993	3.583	3.197	2.848	2.534	2.254
0.56	1.55	n	n	n	n	0.263	0.519
	1.31	4.528	4.118	3.732	3.383	3.069	2.789

Table 5.7: A chart of Δn_{e1} and Δn_{e2} ($\times 10^{-3}$) distributions versus D$_1$ and f for D$_2$=2.0μm and W$_0$=4.0μm. The parameters. λ. D$_1$. and f. are all in μm

f	λ	D$_1$=3.5	4.0	4.5	5.0	5.5	6.0
0.46	1.55	0.112	0.426	0.760	1.083	1.387	1.666
	1.31	0.815	0.366	n	n	n	n
0.48	1.55	0.000	0.314	0.648	0.971	1.275	1.554
	1.31	1.342	0.893	0.475	0.100	n	n
0.49	1.55	n	0.243	0.577	0.900	1.204	1.483
	1.31	1.651	1.202	0.784	0.409	0.074	n
0.50	1.55	n	0.160	0.494	0.871	1.121	1.400
	1.31	1.994	1.545	1.127	0.752	0.417	0.120
0.51	1.55	n	0.063	0.397	0.720	1.024	1.303
	1.31	2.372	1.923	1.505	1.130	0.795	0.498
0.52	1.55	n	n	0.286	0.609	0.913	1.192
	1.31	2.785	2.336	1.918	1.543	1.208	0.911
0.53	1.55	n	n	0.158	0.481	0.785	1.064
	1.31	3.234	2.785	2.367	1.992	1.657	1.360
0.54	1.55	n	n	0.013	0.336	0.640	0.919
	1.31	3.720	3.271	2.853	2.478	2.143	1.846
0.55	1.55	n	n	n	0.171	0.475	0.754
	1.31	4.241	3.792	3.337	2.999	2.664	2.367

Table 5.8: A chart of Δn_{e1} and Δn_{e2} ($\times 10^{-3}$) distributions versus D$_1$ and f for D$_2$=2.0μm and W$_0$=4.5μm. The parameters, λ, D$_1$, and f, are all in μm

f	λ	D_1=3.5	4.0	4.5	5.0	5.5	6.0
0.48	1.55	0.000	0.351	0.717	1.068	1.394	1 693
	1.31	1.427	0.945	0.501	0.105	n	n
0.49	1.55	n	0.270	0.636	0.987	1.313	1.612
	1.31	1.752	1.270	0.826	0.430	0.077	n
0.50	1.55	n	0.177	0.543	0.894	1.220	1.519
	1.31	2.111	1.629	1.185	0.789	0.436	0.125
0.51	1.55	n	0.070	0.436	0.787	1.113	1.412
	1.31	2.505	2.023	1.579	1.183	0.830	0.519
0.52	1.55	n	n	0.313	0.664	0.990	1.289
	1.31	2.935	2.453	2.009	1.613	1.260	0.949
0.53	1.55	n	n	0.173	0.524	0.850	1.149
	1.31	3.400	2.918	2.474	2.078	1.725	1.414
0.54	1.55	n	n	0.014	0.365	0.691	0.990
	1.31	3.903	3.421	2.977	2.581	2.228	1.917
0.55	1.55	n	n	n	0.185	0.511	0.810
	1.31	4.440	3.958	3.514	3.118	2.765	2.454

Table 5.9: A chart of Δn_{e1} and Δn_{e2} ($\times 10^{-3}$) distributions versus D_1 and f for D_2=2.0μm and W_0=5.0μm. The parameters, λ, D_1, and f, are all in μm

Figs.5.7 and 5.8 show the BPM simulations for this design at λ_1 and λ_2, respectively and its corresponding extinction ratios are 32db and 29db for the TM polarization. All the discussions are based on the assumption of $W_1 = W_2$, but W_1 and W_2 can be different. Nevertheless, it does not make much difference in the ERs according to our calculations.

The device has also been calculated for the TE polarization. Since the surface index change is 0.0086 for the TE polarization as shown in Table 4.6 which is much less than that (0.01) for the TM polarization. However, the index of Al_2O_3 cladding is isotropic (ref. Sub-section 4.4.2). As a result, the dispersion curves of two completely separated branch waveguides intersect outside the wavelength region (λ_2, λ_1) for this device optimized for the TM polarization. Hence, no demultiplexing will occur.

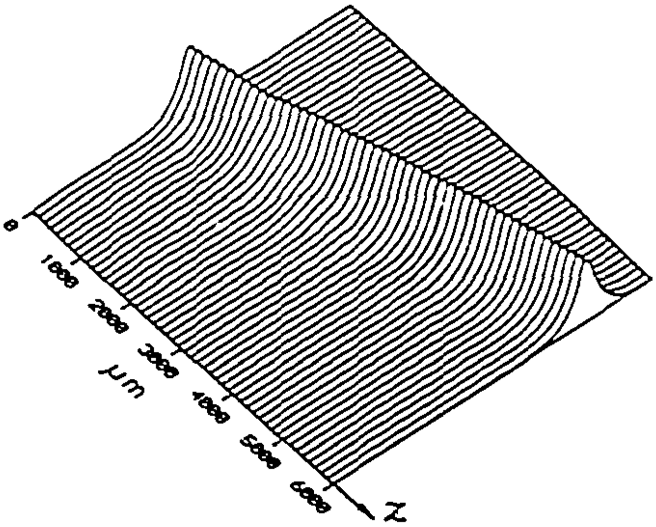

Figure 5.7: BPM results (TM) at $\lambda = 1.55\mu m$, ER=32dB and its device loss -0.18dB, for the device with $\theta = 0.005$ rad, $\theta_2 = 0$, W_1=W_2=W_0=$4.5\mu m$, $D_1 = 5.0\mu m$, $D_2 = 1.25\mu m$, and $f=0.55\mu m$.

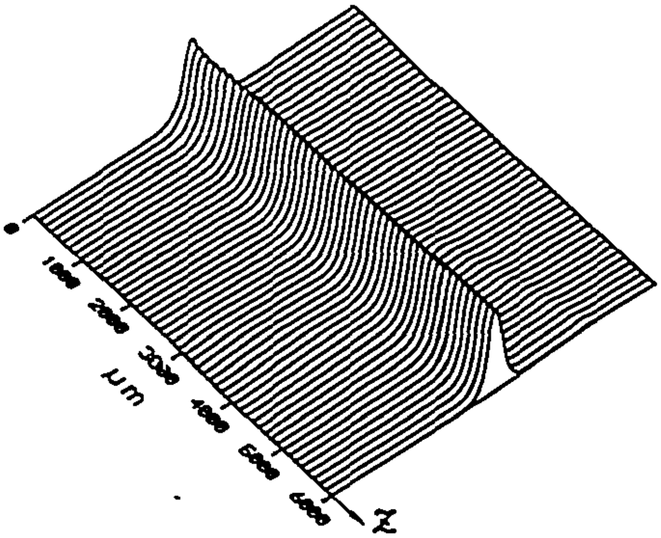

Figure 5.8: BPM results (TM) at $\lambda = 1.31\mu m$, ER=29dB and its device loss -0.17dB, for the device with $\theta = 0.005$ rad, $\theta_2 = 0$, W_1=W_2=W_0=4.5μm, $D_1 = 5.0\mu$m, $D_2 = 1.25\mu$m, and f=0.55μm.

5.4 Fabrication

Before the fabrication, a glass substrate has to be well cleaned. The cleaning procedure is standard [3]. Glass slides made by Fisher Scientific Co. were used as the substrates. The substrate cleaning and most of other fabrication process were performed in a suitable clean-room environment. Both Al-deposition by thermal evaporation and Al_2O_3 deposition by RF sputtering were carried out in a Cooke Vacuum system. The photo-mask alignment and contact printing were carried out in a Cobilt photomask aligner.

5.4.1 Initial fabrication process

The initial fabrication process is illustrated in sequence in Fig.5.9. Two photomasks were needed for fabricating each device sample. The first one as illustrated in Fig.5.10 was used for the first K^+ ion-exchange to form the branch 0 and the branch 1. The figure illustrates only one of the three devices. They are parallel to each other on the mask with a difference only in the wavguide width 4.0μm, 4.5μm, and 5.0μm respectively. The effective waveguide depth and the width are D_1 and $W_0 = W_1$ respectively. The second one as illustrated in Fig.5.11 was used for making branch 2 by K^+ ion-exchange and then by sputtering an Al_2O_3 layer on the top, where $W_0 = W_2$. The second mask has to be aligned with the device which has been made through the first K^+ ion-exchange. The diamond marks in both the masks (see Figs.5.10 and 5.11) are for alignment. The branches are bent out-wards with an angle α (=0.01 rad) after the two branches are well separated (20μm) to shorten the device. Thus, if the final separation of the two branches at the output is to be set to 250μm, the device will be about 2cm long. The descriptions of the fabrication steps are given as follows.

1 Aluminum metallization of the sample by thermal evaporation.

2 Photoresist coating

First, a 4:1 mixture of photoresist (Shipley) and thinner (Shipley AZ) was deposited onto the aluminum surface of the substrate by spin-coating at 3000 RPM for 20 seconds, and then, baking the resulting film for 30 minutes at 80° C (pre-baking).

3 UV exposure

After pre-baking, the first photo-mask was used to expose the resist to UV light through the mask opening for 80-90 seconds.

4 Development

Development of the resist was done in a 2:1 mixture of Microposit developer and D.I. water for 40-60 seconds (depending on the freshness of the solution), resulting in the removal of the resist from the UV exposed areas. Then, the sample was baked for 30 minutes at 120° C to harden the resist pattern (post-baking).

5 Etching

The aluminum was etched away from the areas unprotected by the resist by immersing it in a solution of phosphoric acid, nitric acid, acetic acid, and DI water (16:1:2:1) for 2-10 minutes depending on the freshness of the solution and the thickness of the aluminum film. The etched pattern was occasionally checked under a microscope during the process to make sure that the pattern was free from residues of Al.

6 Photoresist removal

The photoresist was removed by immering the sample in a remover solution (Microposit remover diluted with DI water 1:1).

7 Ion-exchange

KNO$_3$ salt was held in a steel crucible inside a vertical furnace. After the salt was well molten at T=385±1°C, the sample was put inside the furnace to warm up for 10 min. Then, the sample was dipped into the molten salt and the dipping time was counted. The sample was taken out immediately when the desired time was reached. The four ion-exchanged diamond areas became swollen due to the stress in the substrate induced by the ion-exchange [6] but are not visible under the microscope.

8 The aluminum mask was completely etching away in the etching solution as described in Step 5.

9 An aluminum thin film (0.05μm) was deposited on the top of the sample to prepare for the next photomask alignment. After depositing the Al-film, the four swollen diamond areas in the substrate will be clearly visible under the miroscope, and hence, can be used for aligning the second mask.

10 Photoresist coating, same as in Step 2 except the pre-baking for 20 minutes at 80°C.

11 UV exposure, same as Step 3 except that more care should be taken for the alignment. It is designed in the two masks that the two branches are aligned with a designed angle when the diamonds are aligned with each other between the two masks. Here, the alignment is done by aligning the diamond marks on the second mask with the swollen diamonds on the substrate.

12 Development, same as Step 4 but no post-baking.

13 Aluminum deposition by thermal evaporation, same as Step 1.

14 Lift-off

The photoresist together with the Al on its top was removed by immersing the sample in the remover solution as described in Step 6.

15 The sample was dipped into the etching solution for a short period of time which is enough to etch away the Al thin-film used for the pattern visualization in Step 9. so that the parts to be ion-exchanged (branch 2 and those diamonds) are completely opened leaving others covered by aluminum (see Fig.5.9).

16 K^+ ion-exchange for making branch two, the process being the same as in Step 7.

17 Photoresist coating as in Step 2.

18 UV exposure from the back of the substrate for 90 seconds.

19 Development as in Step 4.

20 Al_2O_3 depostion by RF sputtering

After high vacuum was reached in the chamber, a mixed gas of argon and oxygen (80:20) from a gas cylinder was let in with pressure set to 12 PSI in the pressure gauge on the gas supply cylinder. By adjusting the high vacuum valve, the pressure of the flowing gas as indicated in the pressure gauges in the vacuum system was kept at 20 micons (1 micro=1×10^{-3} torr) inside the chamber and 50 micons in the intake of the mechanic pump. Once the air flow was stablized, the RF power was turned on. A light would be on after the RF unit had been warmed up to the normal stage. The RF output was then switched on and its power was tuned to the desired level. Now, a plasma should be clearly seen in the chamber. By tuning the two capacitors of the impedance matching circuit, the reflected power was reduced to a minimum. The shuttle, which usually covers the Al_2O_3 target when it closes, was kept closed for 20 minutes to warm up the system or stabilize the plasma after the plasma was established. Once the shuttle was opened, timing was started. During the sputtering, the input power (or the target voltage), the impedance matching, the water cooling system, and the gas flow were checked every half hour.

21 Photoresist removal as in Step 6.

22 The sample was cut by a diamond cutter for the device to provide good coupling for the input and output light. Smoothly cut edges are always needed for good coupling.

23 Aluminum etching as in Step 5 but with the etching solution heated on a hot plate to speed up the process.

As we can see that to form the Al-mask for the second K^+ ion-exchange, we used a lift-off technique which is more complicated than the process (direct etching) used to form the Al-mask for the first K^+ ion-exchange. However, if the direct etching technique is adopted, the second photo-mask should be the negative of the one shown in Fig.5.11. Thus, the second mask has only the diamonds and the second branch open. They look like small dark diamonds and a dark line respectively under a microscope since they are very small (in the scale of micrometer) and the rest of mask made by chrome strongly reflects the light from above. The pattern on the sample substrate underneath the second mask can be hardly seen from the above. Therefore, it is almost impossible to align the the pattern made by the first K^+ ion-exchange with the mask with only the second branch and the diamonds open provided we make the four diamond areas much larger. After the second K^+ ion-exchange, a photoresist film was used to cover the Al mask. There are two purposes for making this film. One is to ease the removal of unwanted Al_2O_3 after sputtering and the other is to protect the aluminum from the bomdbardment of high power Al_2O_3 molecules splashing from the Al_2O_3 target, since the gigantic chain of the photoresist is much heavier than an Al-atom.

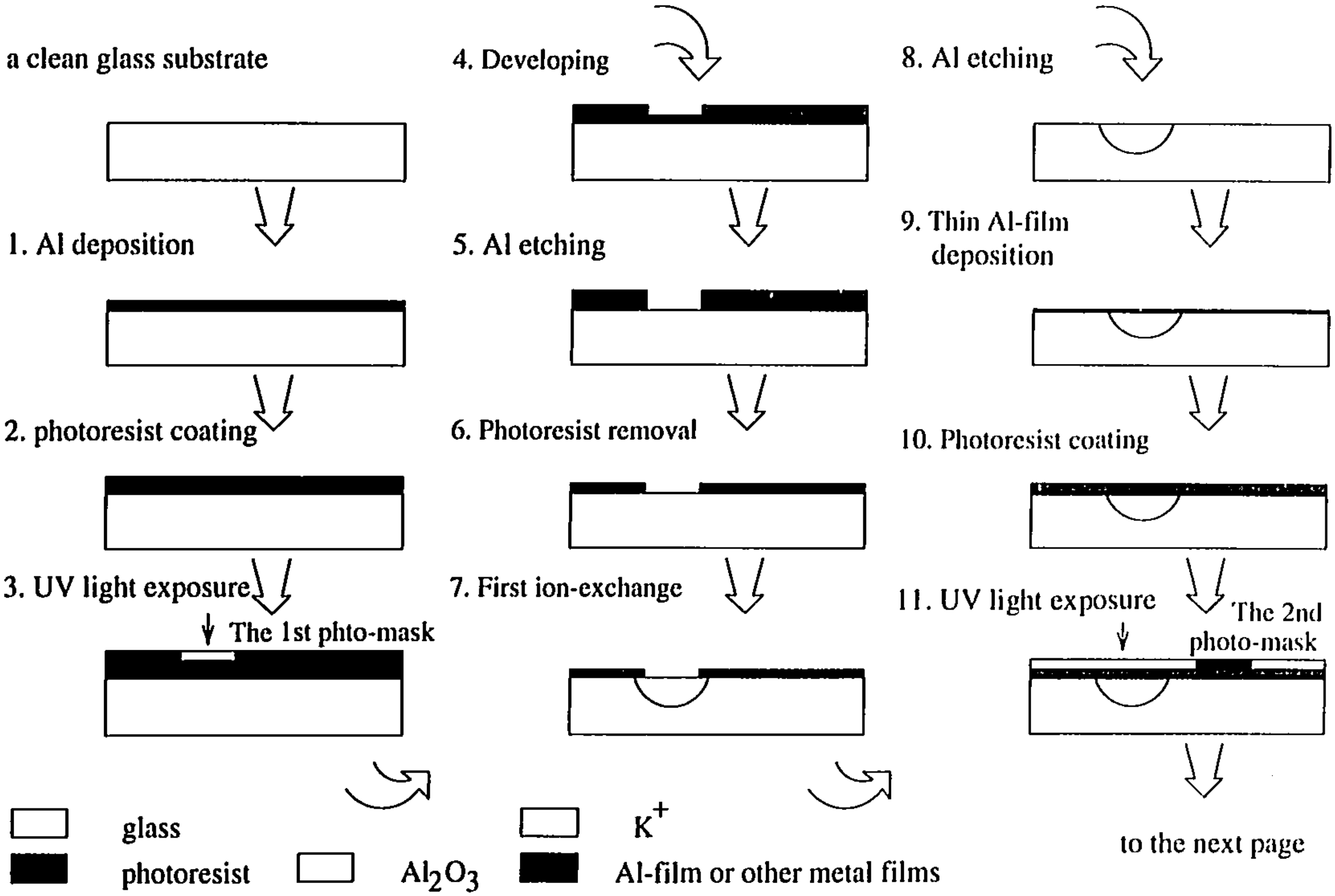

Figure 5.9 (in part)

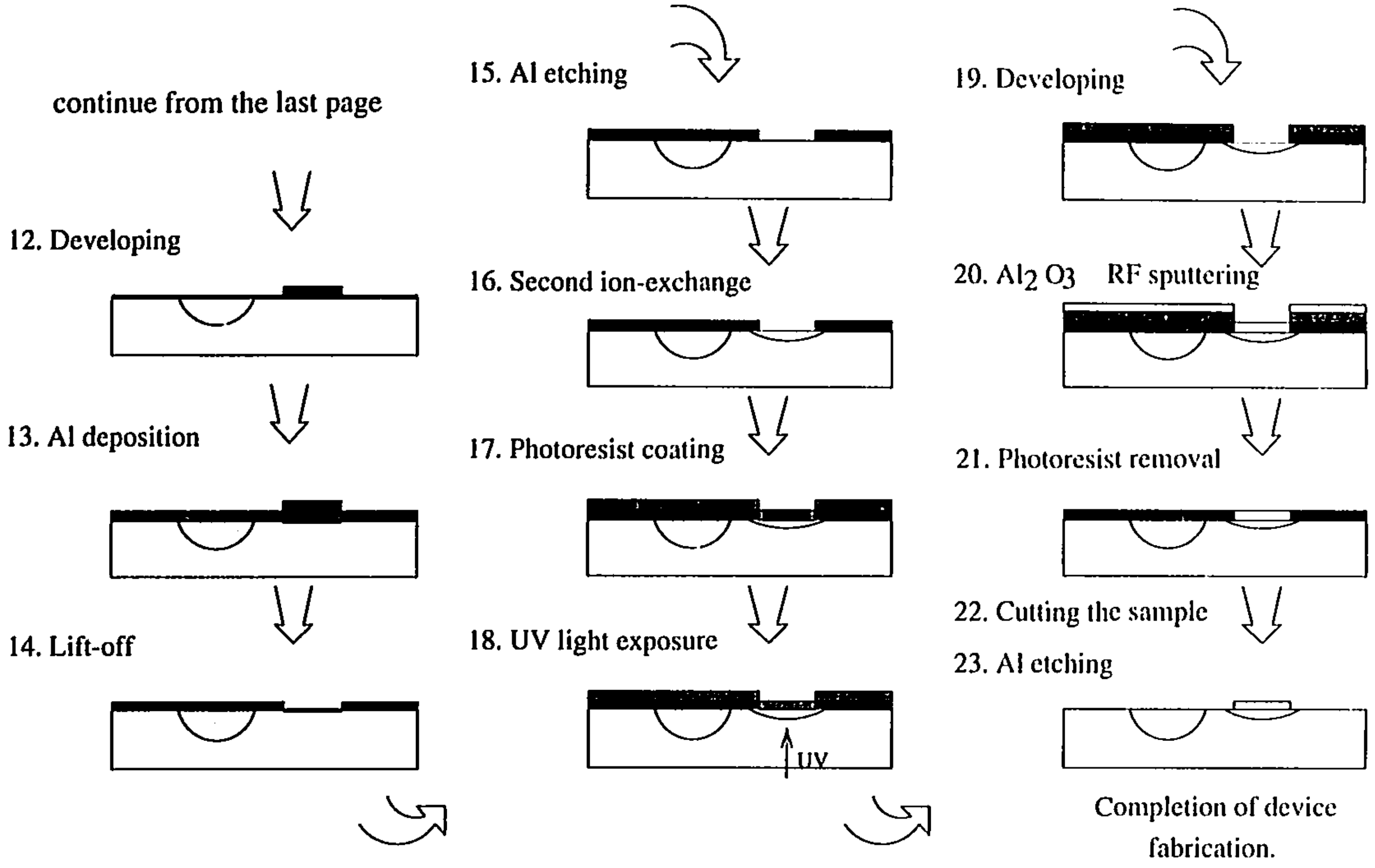

Figure 5.9 The flow chart of the initial fabrication process.

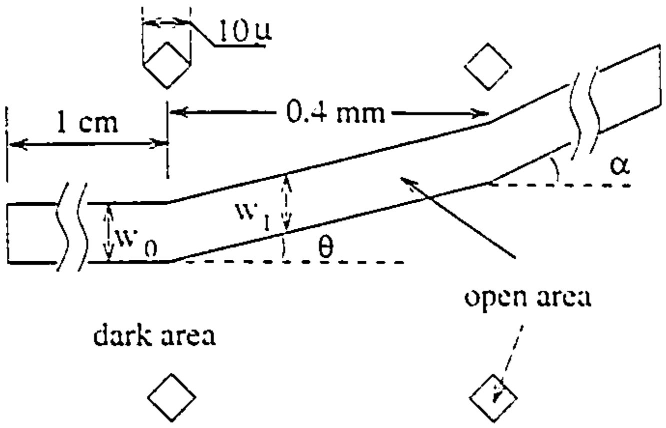

Figure 5.10: The first photo-mask for making the first K$^+$ ion-exchange. The other two devices in the mask are not shown. The difference is only in the waveguide width.

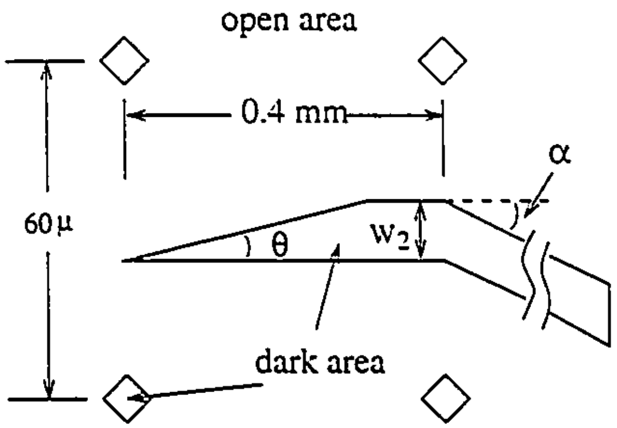

Figure 5.11: The second photo-mask for making the second K$^+$ ion-exchange. The other two devices in the mask are not shown. The difference is only in the waveguide width.

Aluminum would then also be deposited on the surface of branch 2 without a photoresist film's protection, resulting in a highly lossy waveguide.

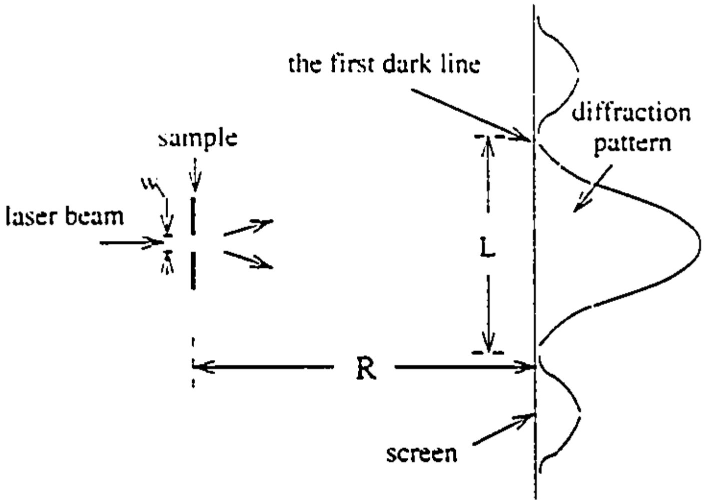

Figure 5.12: The width measurement of an aluminum-mask window by slab diffraction technique.

Before each ion-exchange, the window width of the aluminum mask was measured by a slab aperture diffraction pattern measurement method which is schematically shown in Fig5.12. The Al-mask window for a waveguide is taken as a slit. Its width W is related to the distance L between the two first-order dark lines of the diffraction pattern by

$$W = \frac{\lambda}{sin[tan^{-1}(\frac{L}{2R})]} \tag{5.5}$$

where R is the distance from the mask surface to the screen on which the pattern is measured and λ is the wavelength of a laser light source. In our set-up, $\lambda = 0.6328\mu$m and R=2 m were chosen, which led to a measurement error about $\Delta W = 0.4\mu$m.

5.4.2 Measurement set-up

The measurement set-up used to test our devices is shown in Fig.5.13. The light coupling was realized by a fiber butt-coupling technique. The output light was focussed via a micro (20×) lens to form an image in a Hamamatsu video camera. The video signals were, then, sent to an oscilloscope from which the ERs could be measured. The light spots from the two branches were displayed as two separated peaks on the oscilloscope screen. If V_1 and V_2 represent the heights of the peaks from branch 1 and branch 2 respectively, the ERs in db are defined by

$$ER = \begin{cases} 20log_{10}(\frac{V_1}{V_2}) & \text{for } \lambda_1 \\ 20log_{10}(\frac{V_2}{V_1}) & \text{for } \lambda_2. \end{cases} \qquad (5.6)$$

A He-Ne laser emitting light at $\lambda = 0.6328\mu m$ was used to align the light coupling. Before measurement, the $\lambda = 0.6328\mu$ laser light was coupled into a fiber end by a long focusing lens. After the output spots from the branches were observed, the input-end of the fiber was removed from the $\lambda = 0.6328\mu m$ laser source and plugged into a λ_1 or λ_2 laser diode source. The light coupled into the device from the fiber was considered randomly polarized. A polarizer between the object lens and the video camera was used to get TM modes output only by positioning the polarizer perpendicular to the waveguide surface.

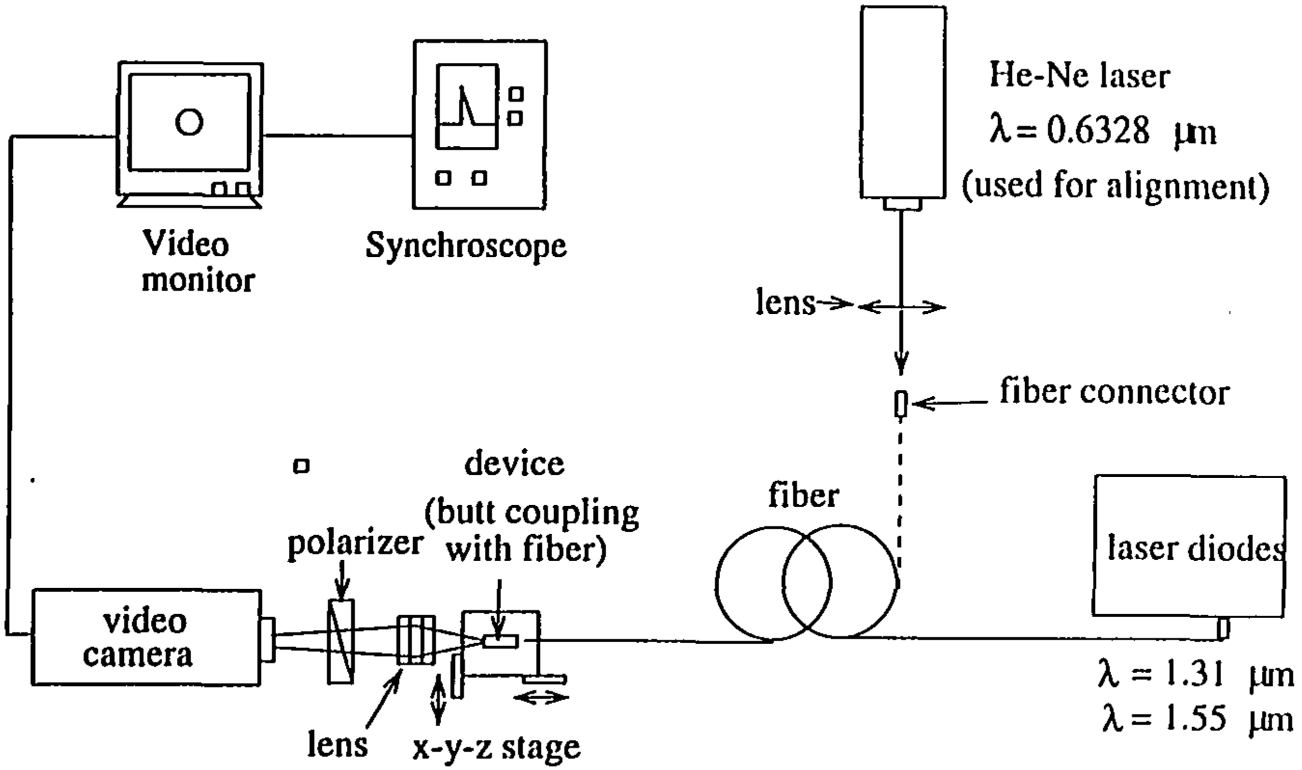

Figure 5.13 DM device measurement set-up.

5.4.3 Preliminary measured results and discussions

Following the process described above, we made many device samples. The output lights came out of branch 1 in most of our fabricated devices even at λ_2 instead of branch 2 as designed. The light could be detected from branch 2 at λ_2 only when the cutting at the output end was very close to the branch apex and the Al_2O_3 cladding was thicker than designed and after the completed device was annealed at high temperature for a period of time. Figs.5.14 and 5.15 show the measured results of the best device among those made. The device has $W_0 = W_1 = 5.40\mu m$, $W_2 = 5.62\mu m$, $D_1 = 3.7\mu m$, $D_2 = 2.5\mu m$, and $f = 0.60\mu m$. The annealing was carried out at 400^oC for an hour with a steady flow of oxygen in a horizontal oven. The measured ERs are greater than 23db and 10db at λ_1 and λ_2 respectively. The results are still much better than those reported previously [1].

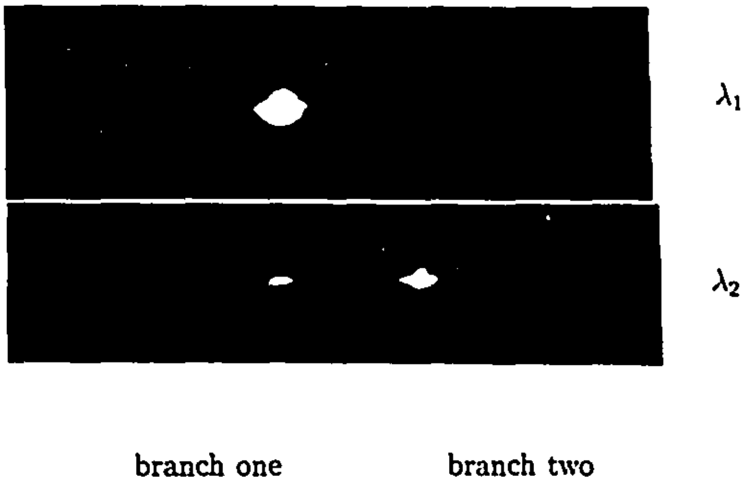

Figure 5.14: Output spots at the end facet of a DM made through the initial fabrication process. W_0=W_1=5.4μm, W_2=5.62μm, D_1=3.7μm, D_2=2.5μm, f=0.6μm.

According to our observations, it is believed that the failure to measure light from branch 2 was due to the high loss in the Al_2O_3 cladded waveguide. This loss might be caused by two factors. One is due to the rough edges of the cladding strip

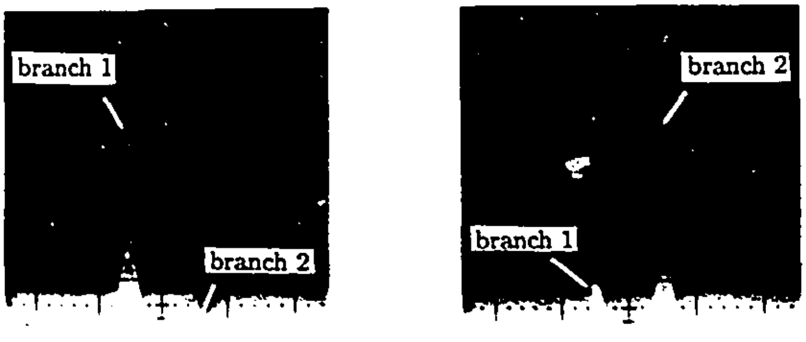

$\lambda_1 = 1.55\mu m$ $\lambda_2 = 1.31\mu m$

Figure 5.15: Output field amplitudes of a DM made through the initial fabrication process.

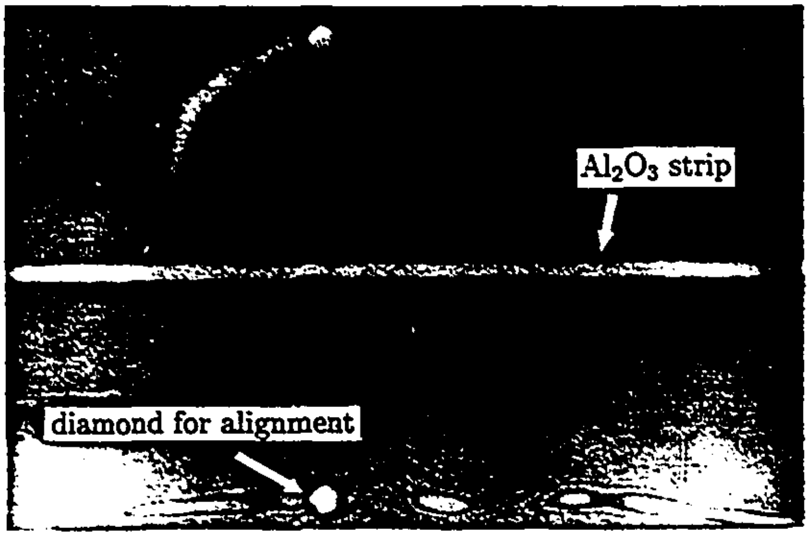

Figure 5.16: The roughness of Al_2O_3 strip edges formed by wet-etching.

since the lift-off of Al_2O_3 over unwanted areas was done by a wet-etching. Fig.5.16 shows a typical strip edges formed by our wet-etching. The other is the roughness of the cladding surface caused by the etching. It has been observed that a sputtered

Al_2O_3 film can be etched away by the etching solution for aluminum at the room temperature. Thus, while we were etching away the aluminum mask in Step 23 in Fig.5.9, the Al_2O_3 cladding was being also etched although its etching was much slower compared with the aluminum's. As a result, the wet-etching not only can damage the surface of the cladding strip but also make the film thinner. To prevent these, the fabrication process had to be modified which will be discussed in the next subsection.

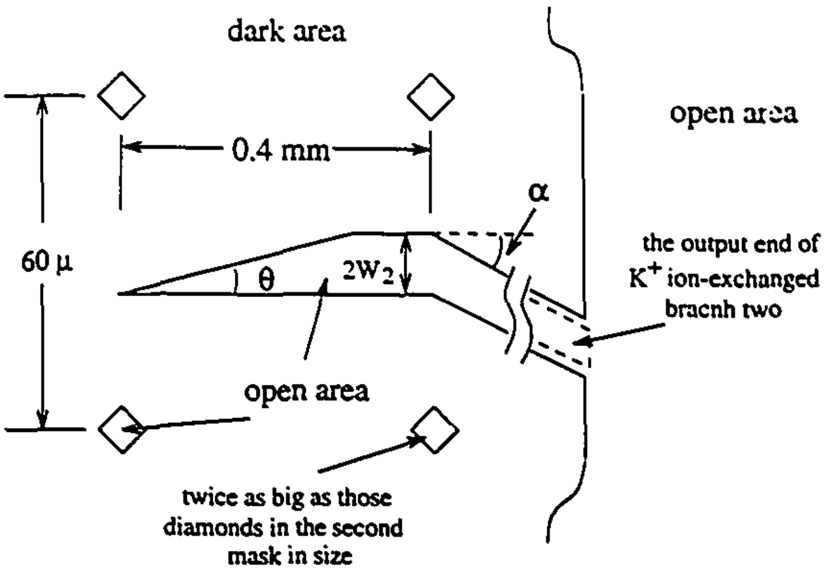

Figure 5.17: The third photo-mask for making an Al_2O_3 strip wider than the second-K^+ ion-exchanged branch.

5.4.4 Modified fabrication process

It is clear that the difficulty in making branch 2 is the chief cause of a faulty device. To eliminate or reduce the light scattering at the Al_2O_3 strip edges, the cladding was widened to about twice of the waveguide width W_2 made by the second ion-exchange. As a result, the rough edges are away from the waveguide. Thus, the field has decayed almost completely as it reaches the cladding edges. To do so, a third

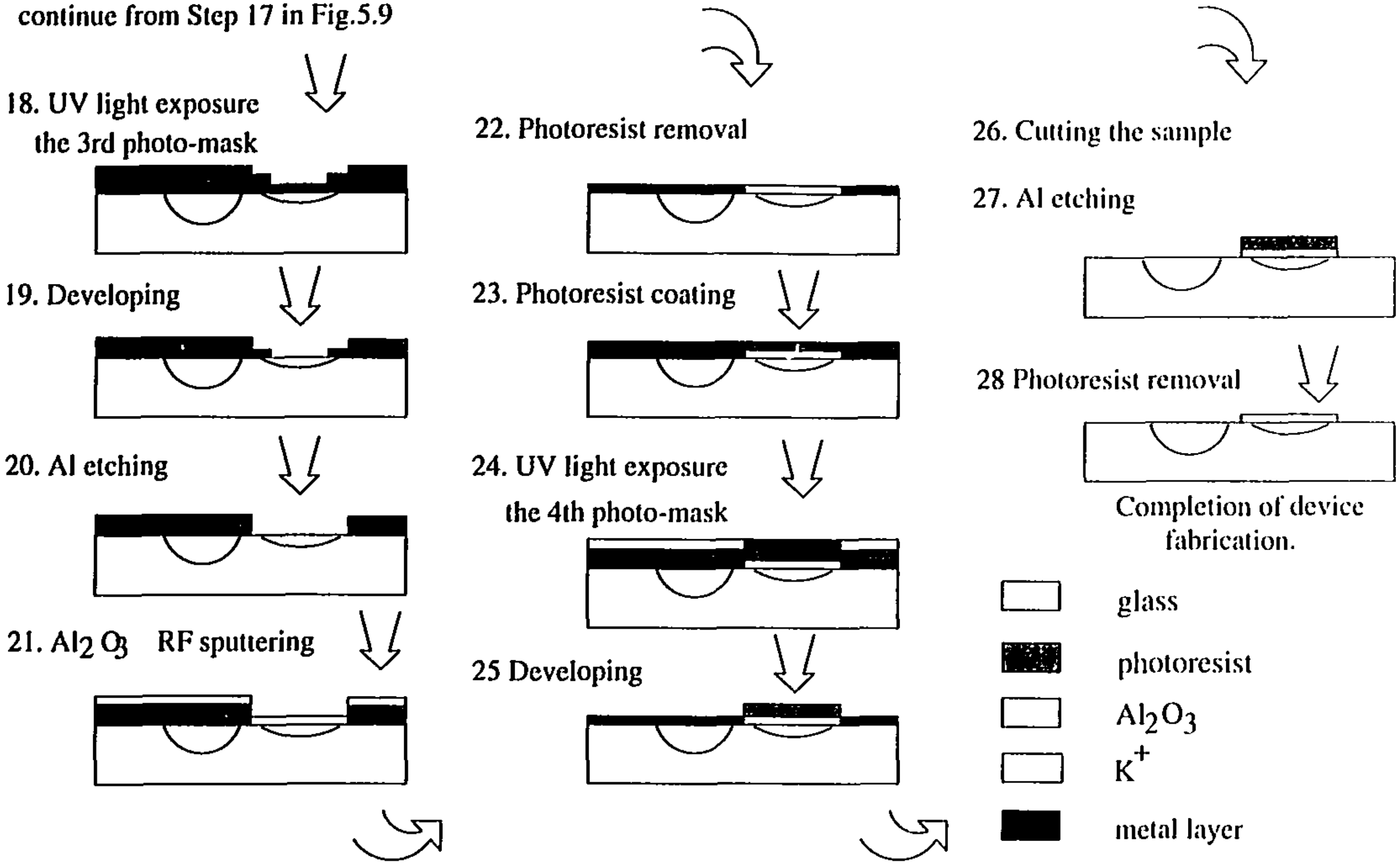

Figure 5.18 The flow chart of the modified fabrication process.

photomask is needed which was shown in Fig.5.17. For the mask alignment, the diamonds in the third mask are twice as big as those in the second mask and the mask is transparent starting right from the ends of all the three devices which are parallelly located on the same masks. In the mask alignment, the open ends of branch two in the 3rd mask are aligned with the K^+ ion-exchanged patterns of branch two. Then, the alignment is checked by the matching of diamonds with the K^+ ion-exchanged diamond patterns. To protect the Al_2O_3 film from being etched, a photoresist film was coated on top of the Al_2O_3 strip before etching away the last aluminum mask. A fourth photo mask may be needed which is exactly the negative of the third photomask. We can also use negative photoresist coating on the top of the devices and expose it from the back of the substrate with UV light without the fourth mask.

The modified process after Step 17 in the last subsection is described as follows and the flow chart for the process is shown in Fig.5.18.

18 UV light exposure after the alignment of the third mask.

19 Development, same as Step 4 in the last sub-section.

20 Al etching, same as Step 5 in the last sub-section.

21 Sputtering, same as Step 20 in the last sub-section.

22 Photoresist removal, same as Step 6 in the last sub-section.

23 Coating a positive photoresist (or negative photoresist).

24 UV exposure after the alignment of the fourth photomask. If a negative photoresist were used, the back of the substrate can be UV exposed without a photomask.

25 Development, same as Step 4 in the last sub-section.

26 The sample was cut at proper locations for the coupling in and out of light.

27 Al etching, same as Step 5 in the last sub-section.

28 The photoresist removal, same as Step 6 in the last sub-section.

Following the fabrication process above, the loss due to the edge roughness and Al_2O_3 surface damage can be reduced. The device is much improved and the output light from branch 2 at λ_2 can now be easily observed.

5.5 Measured Results and Discussions

Fig.5.19 shows the output spots for a device with $W_0 = W_1 = 5.32 \pm 0.4\mu m$, $W_2 = 5.02 \pm 0.4\mu m$, $D_1 = 5.0 \pm 0.1\mu m$, $D_2 = 1.5 \pm 0.1\mu m$, and $f = 0.56 \pm 0.02\mu m$. Their field intensities are shown in Fig.5.20. Their measured ER values together those obtained by BPM simulations are listed in Table 5.10.

ER(dB)	λ_1	λ_2
measured	>25	20
BPM	26	24

Table 5.10: Extinction ratios for a device with $W_0 = W_1 = 5.32 \pm 0.4\mu m$, $W_2 = 5.02 \pm 0.4\mu m$, $D_1 = 5.0 \pm 0.1\mu m$, $D_2 = 1.5 \pm 0.1\mu m$, and $f = 0.56 \pm 0.02\mu m$.

As shown in the table, the device works well and provides high ERs. The measured results basically agree with those calculated from BPM simulations.

The discrepancies between the calculated and measured ER values are mainly due to the uncertainty in the Al_2O_3 thickness. It is difficult to control its error less than ±0.01. We can also see that the device parameters are different from those in the optimized design presented in the previous section, especially the waveguide widths. In the fabrication, the ion-exchange time can be controlled within one minute, resulting in an error ±$0.1\mu m$ in the waveguide effective depth if the furnace temperature T is stable between 384-386°C. But for the waveguide width the situation is very much different. There are many factors which affect the width of the waveguide mask, such as the aluminum film thickness, thickness of the photoresist, UV exposure time, development time, etching time, and uniformities of the aluminum film and the photoresist coating. The waveguide width is difficult to control. To make all the fabricated parameters the same as BPM-optimized ones is very difficult. Fortunately, there are safety margins for those parameters to obtain the ERs over 20db. It is worth mentioning that the linear response range of the video camera is quite limited. The power measured might be beyond the linear range yielding the measured ERs somewhat less than the true ones.

The device works well and can provide high ERs. However, the high sensitivity to the Al_2O_3 cladding thickness makes the device hard to fabricate. A good way to overcome this is to reduce the branch angle. For example, if the angle is chosen to be 0.003 rad, the effective index difference of the two infinitely separated branch waveguides Δn_1 would be less than 0.0002 at λ_1 and Δn_2 less than about 0.0004 at λ_2 to achieve the ERs over 20 db (see Figs.5.5 and 5.6). The fabrication tolerance to the Al_2O_3 thickness can then be approximately relaxed to ±$0.02\mu m$ as we can see from Table 5.1-5.9. As we have discussed before, the branch angle is formed by two photomasks' alignment which can be done without much difficulty. The drawback in the branch angle reduction is a required increase in the device's lengh.

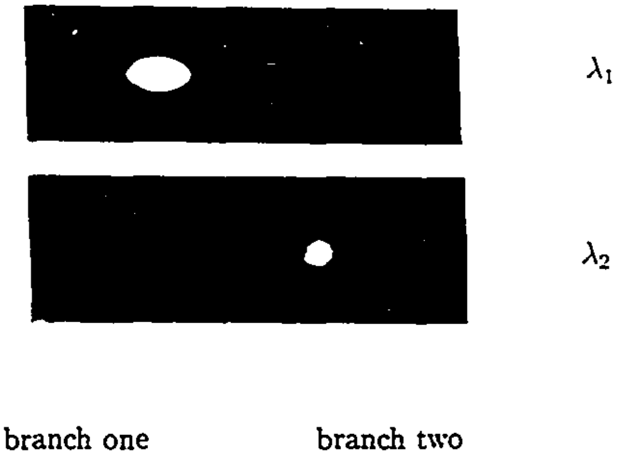

Figure 5.19: Output spots at the end facet for a device described in the text.

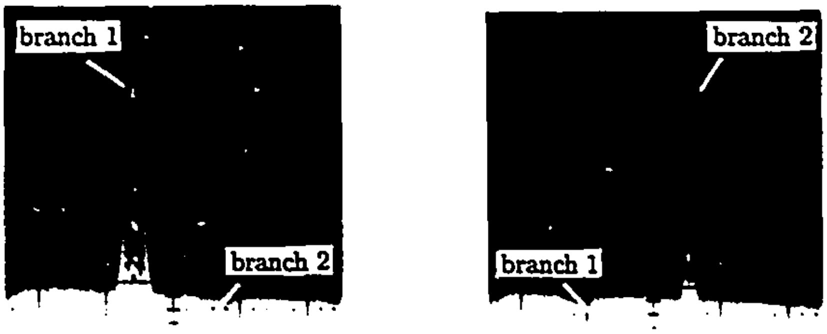

$\lambda_1 = 1.55\mu m$ $\lambda_2 = 1.31\mu m$

Figure 5.20: Output field amplitudes.

Bibliography

[1] N. Goto and G.L. Yip,"Y-branch wavelength multi/demultiplexer for $\lambda = 1.30\mu m$ and $\lambda = 1.55\mu m$", Electronics Lett., vol.26, pp.102-103, 1990.

[2] H. Yajima,"Theory and applications of dielectric branching waveguides", in Proc. Symp. Optical and Acoustical Micro-Elecctronics, pp.339-358, New York, 1974.

[3] M. Masuda and G.L. Yip,*Fabrication techniques of thin film optical waveguides using McGill facilities*, A report of McGill Guided-Wave Photonics Lab., Jan., 1980.

Chapter 6

A K^+ and Ag^+ Ion-exchanged Y-branch WDM

6.1 Introduction

In an Al_2O_3 strip loaded Y-branch WDM discussed in the last chapter, the refractive index of Al_2O_3 is much higher than the surface index of the K^+ ion- exchanged waveguide. In view of this, an Al_2O_3 loaded arm 2 can be made to be relatively shallow and yet to yield a strongly asymmetrical Y-branch and a steep intersection of the dispersion curves of two infinitely separated branches. If the intersection is between the two wavelengths to be demultiplexed and the branch angle is sufficiently small (see Eq.(3.13)), the branch will work as a WDM for these two wavelengths.

Ag^+ ion-exchange in a glass substrate has been a well established technique. It can provide a surface index exchange Δn_s between 0.01 to 0.09 by adjusting the $AgNO_3$ dilution [1], which is much larger than the surface index change $\Delta n_s = 0.01$ by K^+ ion-exchange. Thus, if one branch is made by K^+ ion-exchange and the other branch is made by Ag^+ ion-exchange, a strongly asymmetic Y-branch can be realized. A Y-branch wavelength multi/demultiplexer with a configuration shown in Fig.6.1 can be made by using these two ion-exchanges (K^+ and Ag^+).

The new device does not need an Al_2O_3 cladding which would then simplify the fabrication process and reduces the difficulty of making the second branch. In addition, Ag^+ ion-exchange is done at a temperature lower than the molten temperature of KNO_3. Branch 1 made by K^+ ion-exchange will not suffer from a possible annealing effect during the Ag^+ ion-exchange. This annealing effect would be present if the K^+ ion-exchange is again used to make branch 2 as was the case with the devices discussed in Chapter 5.

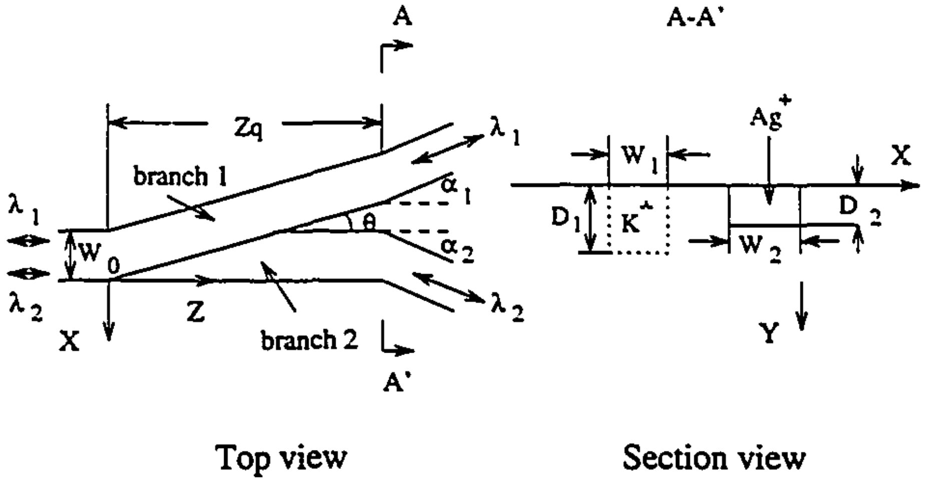

Figure 6.1: Configuration of a Y-junction multi/demultiplexer, where branch 1 is made by K^+ ion-exchange and branch 2 by Ag^+ ion-exchange.

A higher surface-index change, for example $\Delta n = 0.09$ by a pure Ag^+ ion-exchange [2], can yield a large asymmetry in the Y-branch. However, it increases the sensitivity of the device to the parameters, namely, width and depth, of Ag^+ ion-exchanged waveguides. In addition, a waveguide made by a pure Ag^+ ion-exchange suffers from a yellow staining of the glass [3] which increases waveguide losses. On the other hand, diluted $AgNO_3$ will not cause a yellow staining in the glass. Thus, a proper dilution of $AgNO_3$ should be chosen which will be discussed in the next section.

6.2 Chioce of $AgNO_3$ Dilution

A Gaussian function was used to model the index profile of the K^+ ion-exchanged waveguide but a second-order polynomial for that of the Ag^+ ion-exchanged one as discussed in Chapter 4. Numerical simulations of wavelength demultiplexing were carried out with the two-dimensional BPM together with the effective index method.

Since the surface index of branch 2 is the highest of all indices, the depth of the Ag^+ ion-exchanged branch 2, D_2, where the index profile is truncated to intersect the substrate index (d in Fig.4.13 and Fig.4.15), is the most sensitive parameter in this device. Thus, the job of a design optimization is mainly to maximize the tolerance on D_2 while keeping the extinction ratios (ERs) over 20 dB for both wavelengths.

ER is approximately proportional to Δn_{ei} (i=1 or 2). Thus, a steeper dispersion curve for branch 2, corresponding to a more asymmetric branch, would yield larger values of Δn_{ei} and, hence, extinction ratios at both wavelengths, provided D_2 is properly chosen to ensure that the intersection point of the two dispersion curves can be appropriately located between the two wavelengths to be demultiplexed. D_2 depends critically on the surface index change Δn_s of branch 2. A higher value Δn_s of branch 2 will result in a larger asymmetry of the branch and, hence, higher values of ER. However, a simultaneous reduction of D_2 will also be required to locate the intersection point between λ_2 and λ_1 as has been mentioned above. A small change in D_2 will cause relatively larger shift in its dispersion curve due to the larger Δn_s and the smaller D_2. Hence, the device's sensitivity to D_2 is increased. On the other hand, a small Δn_s value of branch 2 will still make the device sensitive to D_2 since a less steep dispersion curve for arm 2 will leave a smaller tolerance margin for D_2 to keep ERs> 20dB. Thus, between the two extremes, there is an optimal Δn_s of branch 2 to yield the largest allowable tolerance ΔD_2 in D_2.

Applying the same definition to the effective-index differences between the branches when they are infinitely separated as those by Eqs.(5.3) and (5.4) and letting the branch angle $\theta = 0.005$rad, we can still use the criteria $\Delta n_{e1} > 0.00033$ for λ_1 and $\Delta n_{e2} > 0.00057$ for λ_2 to achieve the ERs over 20 db as obtained in Chapter 5 based on the BPM simulations. A sketch of the dispersion curves are shown in Fig.6.2 for both individual branches with D_1, W_1 and W_2 given, where $D_2 = D_2''$ gives $\Delta n_{e1} = 0.00033$ and $D_2 = D_2'$ gives $\Delta n_{e2} = 0.00057$.

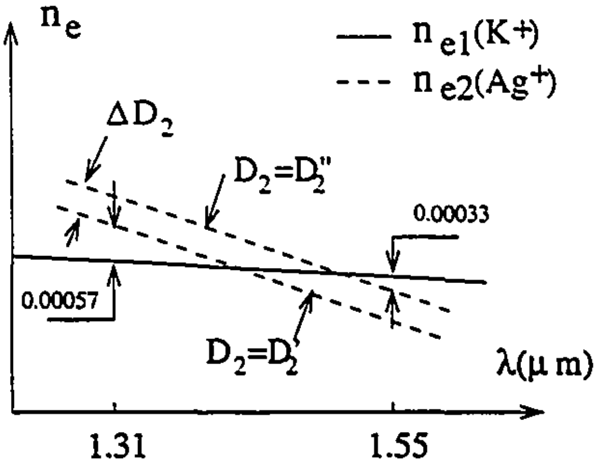

Figure 6.2: The sketch of the dispersion curves for both individual branches,D_2'' is the upper limit of D_2 and D_2' is the lower limit of D_2 for $ER > 20$ dB at both wavelengths.

In Fig.6.2, it can be seen that the desired D_2 should be between D_2' and D_2'' to achieve ERs> 20 dB for both wavelengths. Defining the allowed tolerance of D_2 by

$$\Delta D_2 = D_2'' - D_2' \tag{6.1}$$

ΔD_2 is plotted in Fig.6.3 versus Δn_s of branch 2. The corresponding results for different values of W_1, W_2, and D_1 are quite close when W_1 W_2 and D_1 are not changed beyond $\pm 1\mu m$.

In Fig.6.3, the maximum of ΔD_2 is clearly shown between $\Delta n_s = 0.04$ and 0.06.

The value of ΔD_2 reaches the maximum $0.16\mu m$ at $\Delta n_s = 0.05$. At $\Delta n_s = 0.022$, the device just manages to provide 20db in ER at both wavelengths. It will not be possible to have ER over 20 db at both wavelengths if Δn_s is less than 0.022.

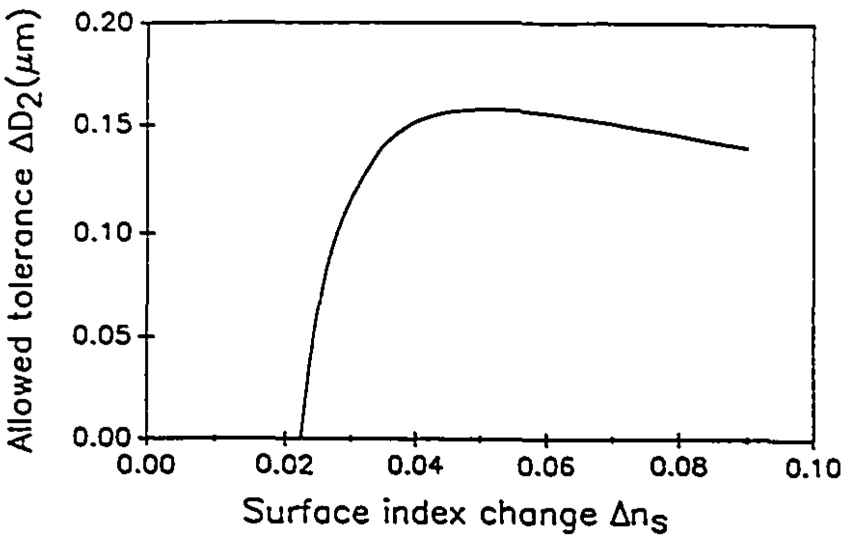

Figure 6.3: The allowed fabrication tolerance of D_2 versus the surface index change in the Ag^+ ion-exchanged waveguide for the ER over 20dB at both wavelengths, where $W_1 = W_2 = 5.0\mu m$, and $D_1 = 5.5\mu m$

6.3 The Optimized Design and the BPM Simulations

In our design, $\Delta n_s = 0.05$, corresponding to the maximum ΔD_2 in Fig.6.3, was chosen which results from approximately one percent $AgNO_3$ in the $NaNO_3$ solution [4]. D_2 was chosen to be $D_2 = \frac{1}{2}(D_2'' + D_2')$. $\Delta D_2 \approx 0.16\mu m$, corresponding to an allowable fabrication error of $\pm 0.08\mu m$ in D_2, allows an error about ± 24 seconds in the ion-exchange time, which can be controlled to within ±10 seconds. Hence, the fabrication tolerances on other parameters can also be relaxed. The final design gives $W_0 = W_1 = W_2 = 5.0\mu m$, $D_1 = 5.5\mu m$, $D_2 = 1.9\mu m$, and $\theta = 0.005 rad$.

Fig.6.4 shows the dispersion curves of two infinitely separated branches of the device. The intersection of these two curves are clearly seen between $\lambda_2 = 1.31\mu m$ and $\lambda_1 = 1.55\mu m$. By BPM simulations as shown in Fig.6.5 for the TM polarization, the design provides ER=28 dB for $\lambda_1 = 1.55\mu m$ and ER=25 dB for $\lambda_2 = 1.31\mu m$. The device losses are 0.20db and 0.10db at λ_1 and λ_2 respectively.

We have also calculated the effective indices of the two individual branch waveguides for the TE polarization for this device already optimized for the TM polarization. The intersection of two dispersion curves occurs outside the wavelength region ($\lambda_2 < \lambda < \lambda_1$). No demultiplexing will occur for the TE polarization for this optimized device. For a TE polarization, the surface index change of K^+ ion-exchange is much smaller than that for a TM polarization. However, the index change formed by Ag^+ ion-exchange is basically isotrcpic. Thus, if the design is for TM, it may not work for TE unless the birefringence of K^+ ion-exchange can be reduced. This is beyond the scope of this work.

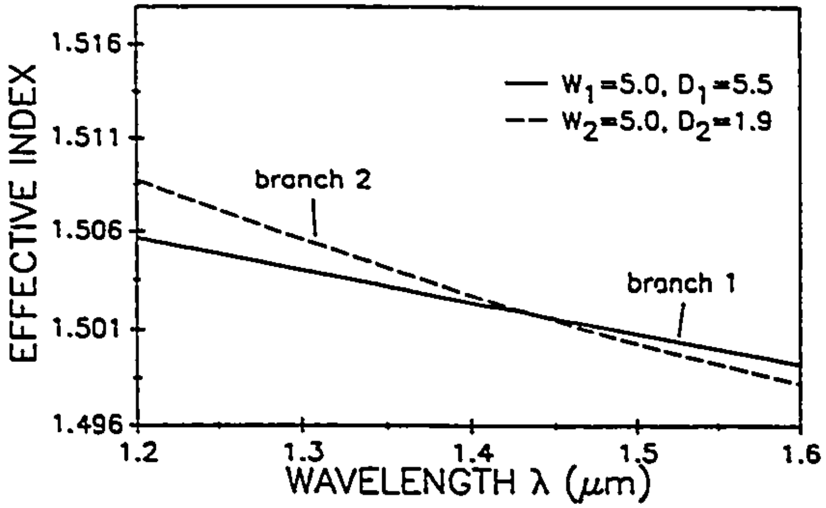

Figure 6.4: Dispersion curves for both individual arms with $W_1 = W_2 = 5.0\mu$m, $D_1 = 5.5\mu$m, and $D_2 = 1.9\mu$m.

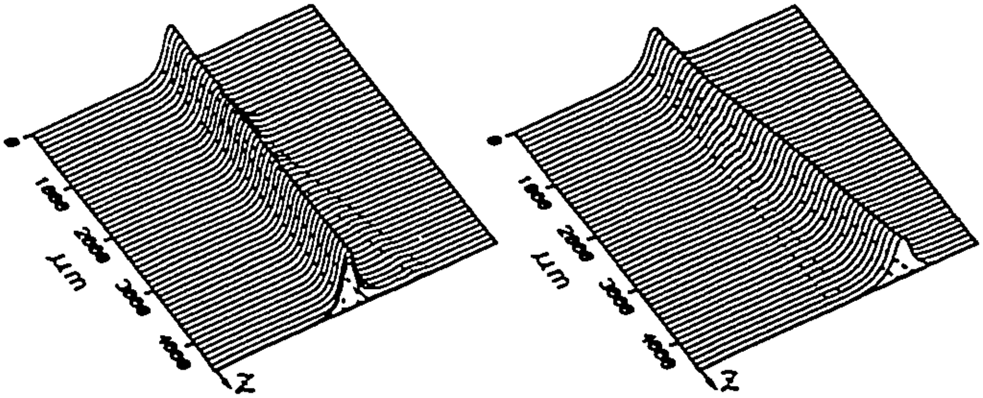

$\lambda_2 = 1.31\mu m$ $\lambda_1 = 1.55\mu m$

Figure 6.5: Results of BPM for the TM polarization, ER=28 dB at $\lambda_1 = 1.55\mu m$ and ER=25 dB at $\lambda_2 = 1.31\mu m$ for $W_1 = W_2 = 5.0\mu$m, $D_1 = 5.5\mu$m, and $D_2 = 1.9\mu$m.

6.4 Device Fabrication

To fabricate the device, two photo-masks are needed. One is for K^+ ion-exchange and the other is for Ag^+ ion-exchange. Both should be aligned accurately. The two masks are the same as the first two masks for the Al_2O_3 loaded demultiplexer shown in Figs.5.10 and 5.11. The first K^+ ion-exchange was carried out at T=385^{0}C for 474 minutes (Ref. Section 4.3) to form the main branch (branch 0) and the first branch.

To make a Ag^+ ion-exchanged channel waveguide, an Al-mask can not be directly used. Ag^+ will be driven underneath the Al mask due to the existence of an electrochemical potential difference between Al and Ag^+ [5] to form a Ag^+ concentration pattern much wider than the expected one. Fig.6.6 shows a top view of a channel waveguide made by Ag^+ ion-exchange through an untreated aluminum mask.

We believe that the bright lines forming at the edges of the waveguide are due to the deposition of the Ag^+. A similar observation was also reported in [5]. No guided light can be seen from the Ag^+ ion-exchanged waveguides after many attempts.

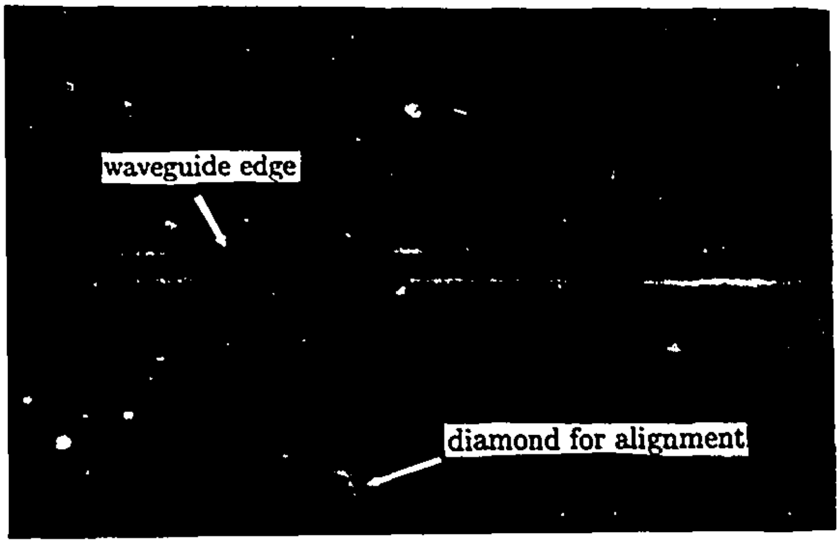

Figure 6.6: A top view of a channel waveguide made by Ag^+ ion-exchange through an untreated aluminum mask.

There are two ways, at least as we know, to overcome this electrochemical potential problem. The first one is to use a K^+ ion-exchange to make a shallow K^+ mask in which K^+ ions on a substrate surface act like a barrier preventing the Ag^+ ions from diffusion into the substrate except the waveguide part where there is no K^+ [6]. To make a K^+ ion mask will certainly affect the exsisting K^+ ion-exchanged waveguides and the whole device. It is, hence, not suitable for our device fabrication. The second is to use aluminum anodization [7] through which the aluminum mask becomes a <u>dielectric</u> mask and, thus, the potential difference is eliminated.

The Al-mask was made with an open window for branch 2 and each of those diamonds after the fabrication process step 15 in Fig.5.9. Hence, it is a negative of the mask shown in Fig.5.11 before anodization. The anodization set-up together with the anodization conditions [7] are shown in Fig.6.7. The anodization lasted about 1 to 3 minutes, depending on the thickness of the Al layer. The current, whose value is dependent on the metal area exposure to the anodization solution, should be monitored during the process. The completion of the anodization is indicated by an abrupt drop of current. The sample was soaked in acetone for a few minutes after a brief rinse in DI water. After anodization, the mask (mostly Al_2O_3 [8]) was transparent although there were some Al metal residues which were unavoidable according to our experiences.

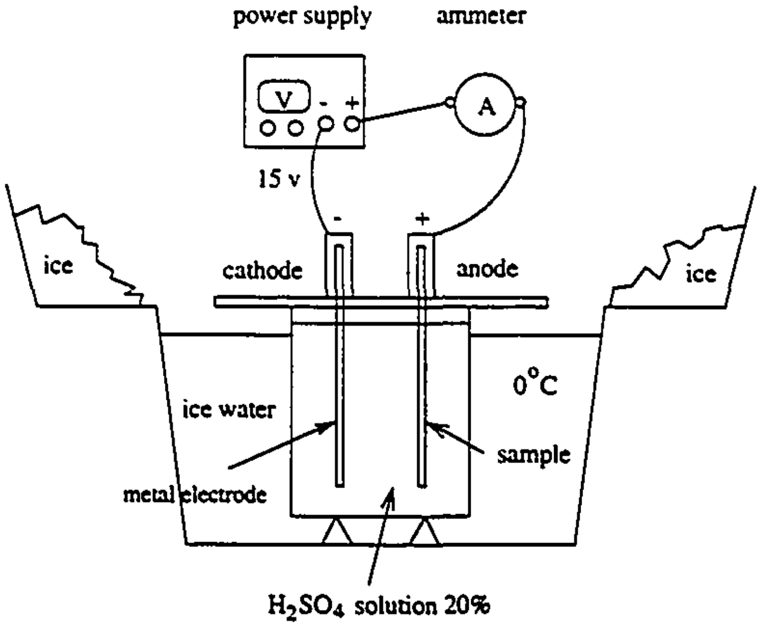

Figure 6.7: The Al-mask anodization set-up.

Then, Ag^+ exchange was carried out at T=325^0 for 3 minutes and 19 seconds. The anodized Al-mask (now becoming Al_2O_3 mask) could be removed by immersing the sample in a commonly used etching solution mixed with H_3PO_4, HNO_3, CH_3COOH, and water at room temperature. The fabrication process is described as follows after Step 15 in Fig.5.9 and the flow chart is summarized in Fig.6.8.

16 Photoresist coating

The sample was coated by photoresist as in Step 2 in the sub-section 5.4.1. The photoresist on the top of the Al-mask windows and their vincinity was, then, wiped out with a cotton tip wetted with acetone. The parts uncovered would be anodized later.

17 Al anodization as described in the second previous paragraph.

18 Photoresist removal, same as Step 6 in the sub-section 5.4.1.

19 Ag^+ ion-exchange as described in the previous paragraph.

20 Cutting the sample

The cutting positions can be conveniently located before the Al-mask (parts of the Al-mask was Al_2O_3) was completely etched away. Otherwise, the device could not be seen clearly once the Al-mask was removed.

21 Etching Al and Al_2O_3 as in Step 23 in the sub-section 5.4.1.

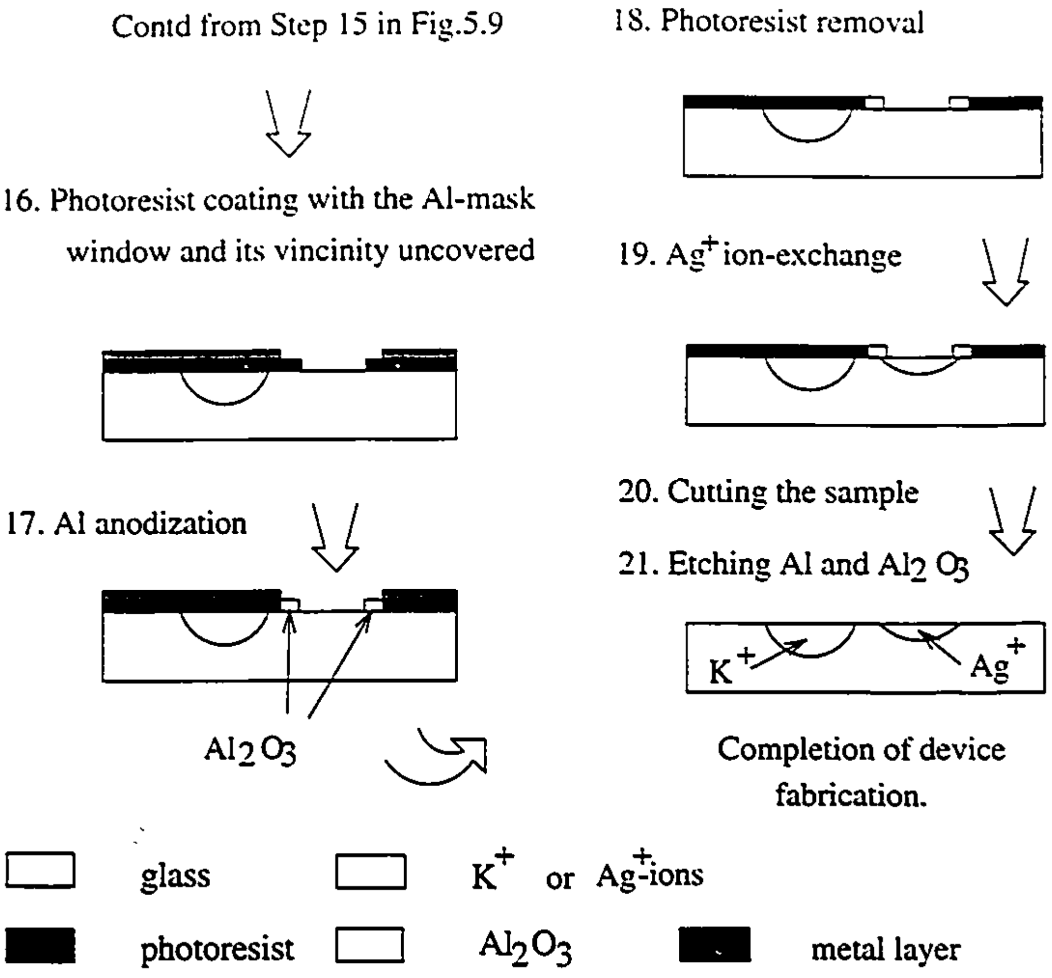

Figure 6.8: Fabrication process for making branch 2 by Ag^+ ion-exchange.

6.5 Measurement Results and Discussions

A fabricated device has $W_1 = 5.0 \pm 0.4\mu m$, $W_2 = 5.7 \pm 0.4\mu m$, $D_1 = 5.5 \pm 0.1\mu m$(474 min. K^+-ion exchange), and $D_2 = 1.9 \pm 0.1\mu m$ (3 min. and 19 sec. Ag^+-ion exchange). The measured extinction ratios are 18db and 23 db at λ_1 and λ_2 respectively. Fig.6.9 shows the near-field output light spots at the end facet. The oscilloscope pictures shown in Fig.6.10 indicate the amplitudes of the output field intensities at both wavelengths.

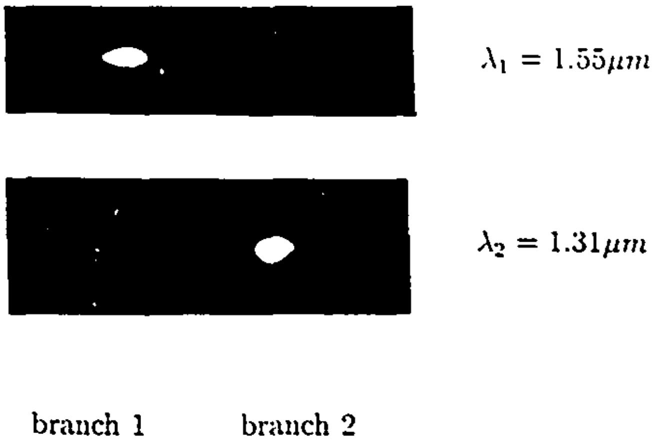

Figure 6.9: Near-field output spots at the end facet for a K^+ and Ag^+ ion-exchanged DM, $W_1 = 5.0\pm0.4\mu$m, $W_2 = 5.7\pm0.4\mu$m, $D_1 = 5.5\pm0.1\mu$m, and $D_2 = 1.9\pm0.15\mu$m.

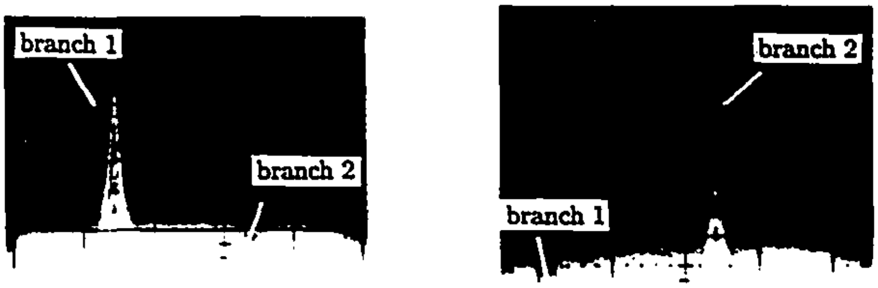

$\lambda_1 = 1.55\mu$m $\lambda_2 = 1.31\mu$m

Figure 6.10: Near-field output field amplitudes for a K^+ and Ag^+ ion-exchanged DM. The device parameters are given in Fig.6.9.

In comparison with the BPM results, 25db and 24db at λ_1 and λ_2 respectively, there are still discrepancies in the measured extinction ratios from the BPM results.

We believe that the discrepancies may be mainly due to the width uncertainty and Ag^+-ion exchanged depth uncertainty. The waveguide widths were obtained by measuring the waveguide mask window widths before ion-exchange. The measurement method (slot diffration pattern measurement see Section 5.4) yielded about $\pm 0.4\mu$ uncertainty. The Ag^+ ion-exchange depth uncertainty might have been caused by the error in controlling the diffusion time and in the diffusion coefficient from our experimental characterization [4] where it is mostly based on the data from multi-mode waveguides. In addition, the device index structure used in the BPM simulations was idealized. The side diffusions of both K^+- and Ag^+-ions, photomask mis-alignment, non-uniformity of waveguide widths, and so on have all been neglected in the calculations. These may be the reasons that the extinction ratios obtained by BPM are higher than those measured.

There are several ways to improve the device. First, a smaller branch angle, for example $\theta = 0.003$, can be used to increase the ER values as we have discussed in Chapter 5. Secondly, an increase of the surface index change by Ag^+ ion-exchange, for example $\Delta n_s = 0.06$, may help to enhance the branch asymmetry, and, therefore, the ER values. The drawback lies in the reduced fabication tolerance. In a future design, the side-diffusions of both K^+ and Ag^+ ions should be considered for more accurate modelling.

In summary, Ag^+ ion-exchanged waveguides have been successfully made after the Al-masks were anodized. The experiment results show that the device by a two-step ion-exchange process is feasible and can provide high ER values. The results presented are still preliminary. There are several ways to improve the device performances which merit further investigation.

Bibliography

[1] G. Stewart and P.J.R. Laybourn,"Fabrication of ion-exchanged optical waveguides from dilute silver nitrate melts", IEEE J. Quantum Elec., vol.QE-14, pp.930-934, 1978.

[2] G. Stewart, C.A. Millar, P.J.R. Laybourn, C.D.W. Wilkinson, and R.M. Delarne,"Planar optical waveguides formed by silver-ion migration in glass", IEEE J. Quantum Elec., vol.QE-13, pp.192-200, 1977.

[3] G.E. Rindone and W.A. Weyl,"Glasses as electrolytes in galvanic cells: silver glasses", J. Amer. Ceram. Soc., vol. 33, pp. 91-95, (1950).

[4] F. Xiang, K.H. Chen, and G.L. Yip,"The application of an improved WKB method to the characterization of diluted silver ion-exchanged glass waveguides in the near infrared", SPIE conference proceedings, vol.1794, pp.40-47, 1992.

[5] G. Chartier, P. Collier, A. Guez, P. Jaussaud, and Y. Won,"Graded-index surface or buried waveguides by ion exchange in glass", Appl. Opt., vol. 19, No.7, pp.1092-1095, April 1980.

[6] G. Chartier, P.J.R. Laybourn, and A. Girod, "Masking process for double-ion-exchanged glass optical waveguides", Elecron., Lett., vol.22, pp.925-926, 1986.

[7] R.G. Walker, C.D.W. Wilkinson, and J.A.H. Wilkinson," Integrated optical waveguiding structures made by silver ion-exchange in glass. I: The propagation

characteristics of stripe ion-exchanged waveguides: a theoretical and experimental investigation". Appl. Opt., vol.22, No.12, pp. 1923-1928, (1983).

[8] S. Wernick and R. Pinner, *Surface Treatment of Aluminum*, vol.1, Robert Draper, Ltd., Teddington, U.K., 1972.

Chapter 7

Proposals and Designs: Mach-Zehnder Wavelength DMs

7.1 Introduction

Although a two-ion exchange Y-branch WDM simplifies the fabrication process for a strip loaded one, it still requires two masks and many fabrication steps to fabricate. Many other structures can be used to form a wavelength demultiplexer(WDM), such as a X-branch [1]-[2] and directional coupler [3]. Only one mask will be needed for these devices and their fabrication processes are much simpler. However, their required lengths are greater and fabrication tolerances low. Recently, it has been reported that a Mach-Zehnder interferometer [4] can be used to form a WDM with high extinction ratios and less sensitivity to fabrication parameters. The device also requires only one photomask for fabrication.

Fig.7.1 shows the configuration of a Mach-Zehnder interferometer DM. It consists of a 3-db power divider which splits the input power into two interferometer arms. A 4-port hybrid coupler, formed by a symmetric converging section (a 3-db combiner) and an asymmetric Y-branch mode splitter, is located at the end of the interferometer. The two arms of the interferometer are designed to be asymmetric such that a phase delay will be realized in one arm at the end. Conventionally, one arm (arm 1 in Fig.7.1) is made longer (ΔL) to achieve a phase delay but with an equal arm width ($W_1 = W_2$). This kind of structures is insensitive to the propagation constant, hence making the fabrication relatively easy if the device mask is accurately made. However, on the other hand, the device design does not allow any adjustment if the mask contains some fabrication defects. For a weakly guiding structure, for example, K^+ ion-exchanged device in a glass substrate, the WDM device needs to be quite long to reduce the bending loss. Further, the device can only demultiplex certain pairs of wavelengths (if two wavelengths are to be demultiplexed) since two phase match conditions have to be satisfied simultaneously with only one adjustable variable ΔL. Besides the contribution from the arm length difference ΔL, the phase delay can also arise from the propagation constant difference $\Delta\beta$ due to the width difference between the two arms. Thus, ΔL can be reduced, even completely eliminated, leading to a shorter device.

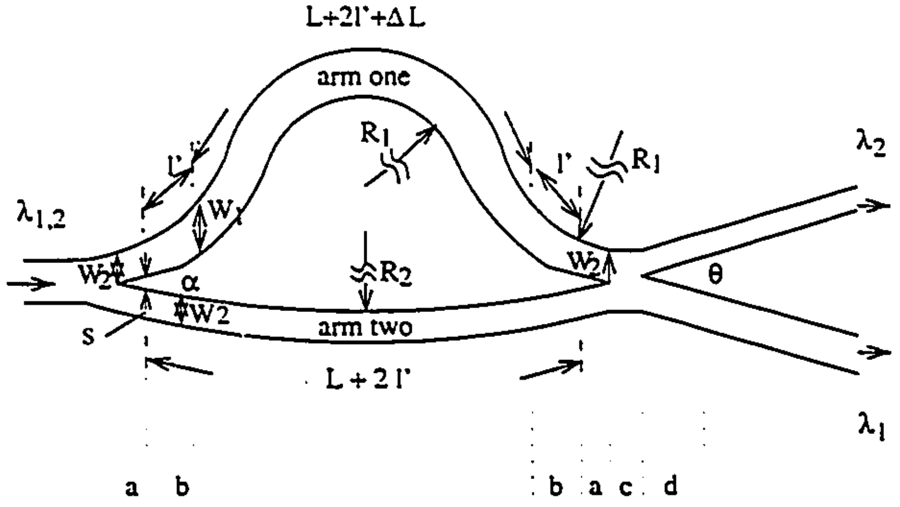

Figure 7.1: Configuration of a Mach-Zehnder DM, a: power divider or combiner, b: taper region, c: two-mode region, and d:mode splitter.

If two arm widths are different, eg. $W_1 > W_2$, we need two tapered waveguides with length l' (see Fig.7.1) at the two ends of the first arm (width W_1) to provide a smoother transition for arm 1 ($W_2 \rightarrow W_1 \rightarrow W_2$) and eliminate the excitation of high order-modes.

Since there are two adjustable variables ΔL and $\Delta\beta$ in design, the phase match conditions can be satisfied more easily. Thus, a three-wavelength DM is also feasible by using the Mach-Zehnder structure, in which three phase match conditions have to be satisfied. It is almost impossible, if the asymmetry comes only from the length differnece between the two arms of the interferometer. The drawbacks are that the device and its design become more complicated and the sensitivity to the fabrication parameter changes is increased. However, the difficulty in design can be eased with the help of the well-developed beam propagation method (BPM). The fabrication sensitivity may not be a serious problem either if it can be controlled within an acceptable range.

In this chapter, we apply this concept to propose and design two two-wavelength and a three-wavelength DMs in the following separate sections. The designs were carried out by using mainly the BPM and FD-BPM. Their performances will also be presented.

7.2 Mach-Zehnder Two-Wavelength DMs

7.2.1 Principle of operation

Consider the two wavelengths to be demultiplexed as λ_1 and λ_2 ($\lambda_1 > \lambda_2$) and assume arm 1 of the interferometer to be wider ($W_1 > W_2$) and longer by ΔL. The two branches of the asymmetric Y-branch at the output have different widths. With a small branch angle, the wider branch will accept the local fundamantal mode and the other the local second-order mode (ref. Chapter 3). The incoming light with a shorter wavelength (λ_2) will excite the local second-order mode at the 4-port hybrid coupler junction and enter the narrower branch, while the light with a longer wavelength (λ_1) will excite the local fundamental mode and enter the wider branch. The illustrations of the wave propagation machinism through the 4-port hybrid coupler are shown in Fig.7.2 for both the wavelengths.

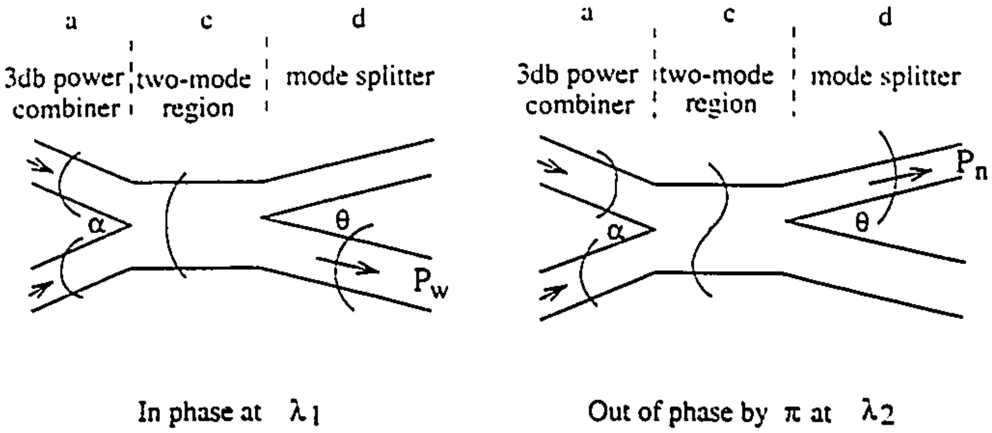

Figure 7.2: Illustrations of the wave propagation mechanism through the 4-port hybrid coupler for both the wavelengths.

The total phase delay by arm 1 with respect to arm 2 can be written as

$$\phi = (\beta_1 - \beta_2)L + \beta_1 \Delta L + 2l'(\overline{\beta_1} - \beta_2) \tag{7.1}$$

and the output powers are given [4] by

$$P_w(\text{wider branch}) = P_0(1 + cos\phi)/2 \tag{7.2}$$

$$P_n(\text{narrower branch}) = P_0(1 - cos\phi)/2 \tag{7.3}$$

where the subscript in β indicates the arm number, $\bar{\beta}_1$ the average propagation constant over the tapered region l' in arm one, and P_0 the input power. The phase match conditions for the two wavelengths at the end of the interferometer can be written as

$$\phi(\lambda = \lambda_1) = 2M\pi \tag{7.4}$$

$$\phi(\lambda = \lambda_2) = (2N + 1)\pi \tag{7.5}$$

where $M \leq N$ and $M, N = 1, 2, \cdots$. Thus, at the shorter wavelength λ_2 (see Eqs.(7.1) and (7.5)), since the lights with equal power from the two interferometer arms are out of phase by 180° at the output end, a second-order mode will be excited in the junction waveguide of the 4-port hybrid coupler. At the longer wavelength λ_1, since they are in phase (see Eqs.(7.1) and (7.4)), a fundamental mode will be excited. It can be clearly seen in Eq.(7.1) that the total phase delay can mainly arise from either the waveguide propagation constant difference between the two arms, given by the first term of Eq.(7.1) or the arm length difference in the second term since the third term is very small. If the two arms are identical in width, both the first and third term vanish, yielding the device reported in [4]. Another limit is to set ΔL to zero so that the phase delay will all come from the difference in β. Since the error in the phase delay caused by the error in the propagation constants is approximately proportional to L (see Eq.(7.1)), L should be kept short to reduce fabrication sensitivities of the device.

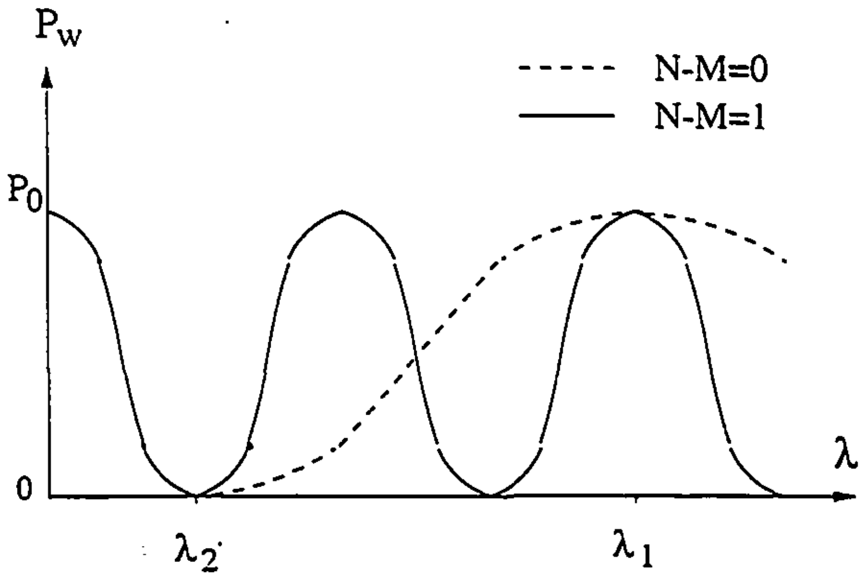

Figure 7.3: Light power from the wider branch versus light wavelength.

When the wavelength λ increases from λ_2 to λ_1, the output power P_w (see

Eq.(7.2)) will go through $2(N - M) + 1$ time oscillations between zero and P_0 as shown in Fig.7.3. The same conclusion can also be drawn on P_n. Therefore, to obtain the widest bandwidth possible, M and N should be chosen equal for only one oscillation between λ_1 and λ_2 (the dashed line in Fig.7.3). As we can see in the phase match conditions, a small phase delay generally requires a short L. M and N should also be kept small to reduce fabrication sensitivities of the device.

For a device with an identical arm width, there is one variable ΔL and two integer variables M and N in two phase match conditions Eqs.(7.4) and (7.5). Only certain pairs of wavelengths λ_1 and λ_2 can satisfy the two phase match conditions simultaneously. However, if the difference in the propagation constants between the two arms also contributes to the phase delay, β_1 (W_1), β_2 (W_2), and L are the additional variables adjustable to satisfy the two phase match conditions. Thus, the wavelengths to be demultiplexed can be chosen more freely in this device.

7.2.2 Devices and their performances

The first device has both its arms equal in length, $\Delta L = 0$, as a special example. The second device has a phase delay in arm 1 due to both ΔL and $\Delta\beta$. Usually, symmetric Y-branches are needed at both the beginning (first) and the end (second) of the Mach-Zehnder interferometer as shown in Fig.7.1, which act as a 3db power devider and a 3db power combiner, respectively. It is understandable that, between the two output branches of a Y-branch, one receives more power if its width is wider but less power if it is bent outward with larger angle. In device two, by balancing the bending (i.e. adjusting R_1) and widening (adjusting l') of the branches connected to arm 1, we can design to have an equal power output from the two branches at a distance l' away from the first Y-branch apex and hence also an equal power input into the two branches at the second Y-branch apex. In other words, the taper regions (region b in Fig.7.1) function not only as adiabatic transition ($W_2 \rightarrow W_1 \rightarrow W_2$) but also a 3db divider and a 3db combiner (region a in Fig.7.1). Thus, the symmetric Y-branches (region a) are not needed (s=0) and the length of the device can be shortened.

To achieve the difference in β, we have chosen different widths for the two arms but kept their depths equal for single-step fabrication. By choosing different values of ΔL,L,W_1,W_2, and waveguide depth D in Eqs.(7.1), (7.4), and (7.5), we can have many combinations of solutions. The parameters should be chosen to meet the requirements for small M and N values, a shorter device, small bending loss, being away from mode cutoffs, low sensitivity to parameter variations, and so on.

$\lambda_1 = 1.55$ and $\lambda_2 = 1.31$ have been chosen to be the two wavelengths to be demultiplexed. The waveguide structure used for testing the device concept is to be made by K^+-Na^+ ion-exchange in a soda-lime glass substrate at temperature T=385° [5] and [6]. The index profile in the depth direction is Guassian-like with 0.01 as the maximum index change on the waveguide surface for both wavelengths. n_b=1.5011 and 1.4982 have been taken as the glass indices at wavelength λ_2 and λ_1, respectively. Any side diffusion in the fabrication process has been neglected in the design. The designs were performed for the TM polarization with respect to the waveguide surface. The depths of K^+ ion-exchanged waveguides are given by the effective depths defined in Chapter 4.

For the first device, an ion-exchange depth D=4.5μm (ion-exchange time t = 284 min.), W_1=8.2μm, W_2=4.0μm, ΔL=0, L=2430.0μm, the branch separation at the end (or the beginning) of symmetric Y-branch power divider (or combiner) s=17.5μm, M=N=1, the waveguide bending radius R=64.7143mm for both arms were chosen, and the calculated extinction ratios are 34.41db at λ_1 and 31.56db at λ_2, respectively. For the second device, D=5.5μm (t = 341 min.), W_1=10.09 μm, W_2=3.8μm,

$\Delta L=0.42\mu m$, $L=1183.6\mu m$, $s=0$, $M=N=2$, $R_1=18.5$mm for arm 1 and $R_2 = 56.8252$ mm for arm 2 were chosen, and the calculated extinction ratios are 37.41db at λ_1 and 33.09db at λ_2, respectively. $l'=400\mu m$, $\alpha = 0.035$ rad, and $\theta = 0.005$ rad were chosen for both devices.

The BPM simulations for device one and two are shown in Fig.7.4 and Fig.7.5, respectively. Plotting the extinction ratios obtained by the BPM simulations versus the wavelength of the input light, we get Figs.7.6 and 7.7 for both devices near $\lambda_1 = 1.55$ and $\lambda_2 = 1.31\mu m$.

It is found that the bandwidth for the extinction ratios over 20db in each figure is about 30nm. Figs.7.8 and 7.9 show the curves of extinction ratios versus fabrication errors Δt in the diffusion time for the first and second device, respectively. Both devices can provide extinction ratios over 20db if the diffusion time can be controlled within ±10 min, which is at least twice the time deviation a X-branch WDM can tolerate [2].

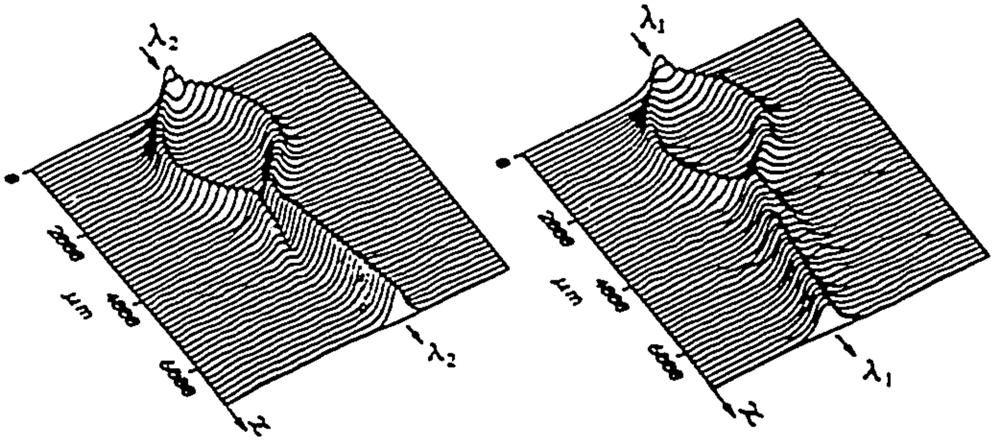

Figure 7.4: BPM simulation for device 1.

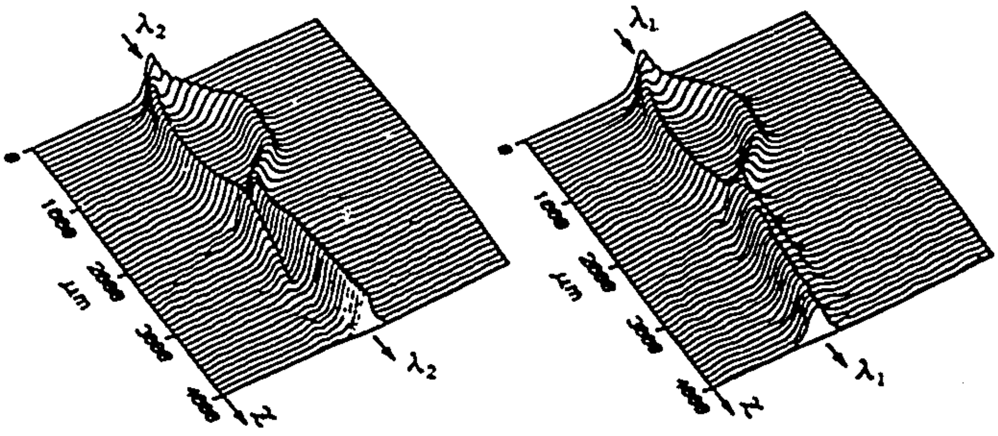

Figure 7.5: BPM simulation for device 2.

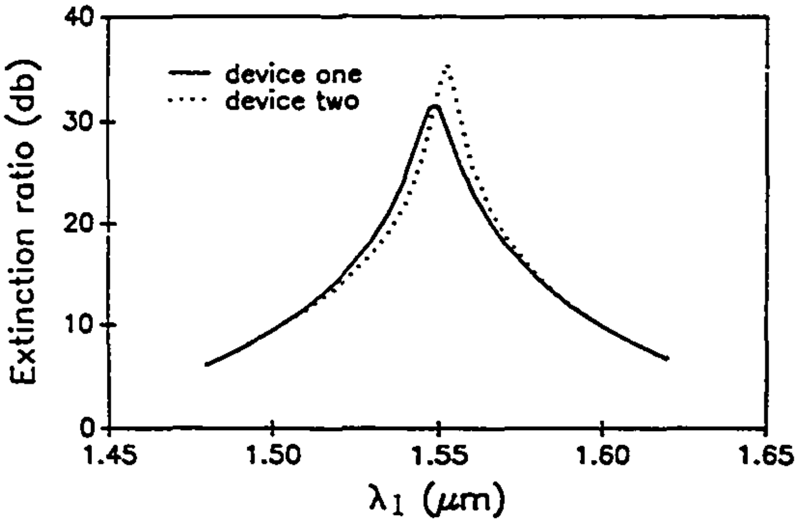

Figure 7.6: Curves of extinction ratio versus the input wavelength λ_1 for both devices.

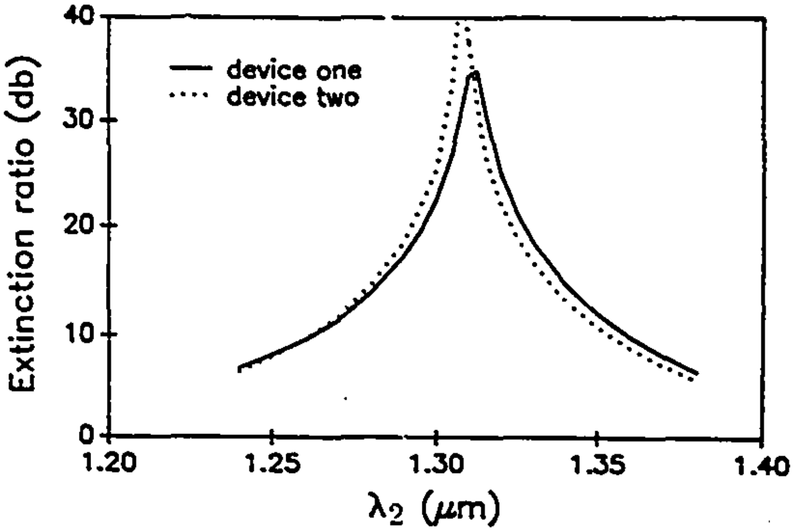

Figure 7.7: Curves of extinction ratio versus the input wavelength λ_2 for both devices.

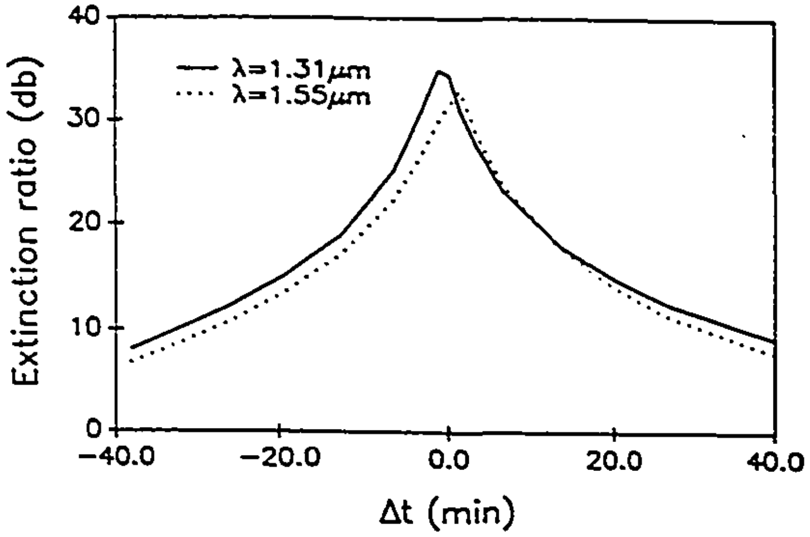

Figure 7.8: Curves of extinction ratio versus the error in diffusion time for device one. The designed ion-exchange time is 284.5 minutes.

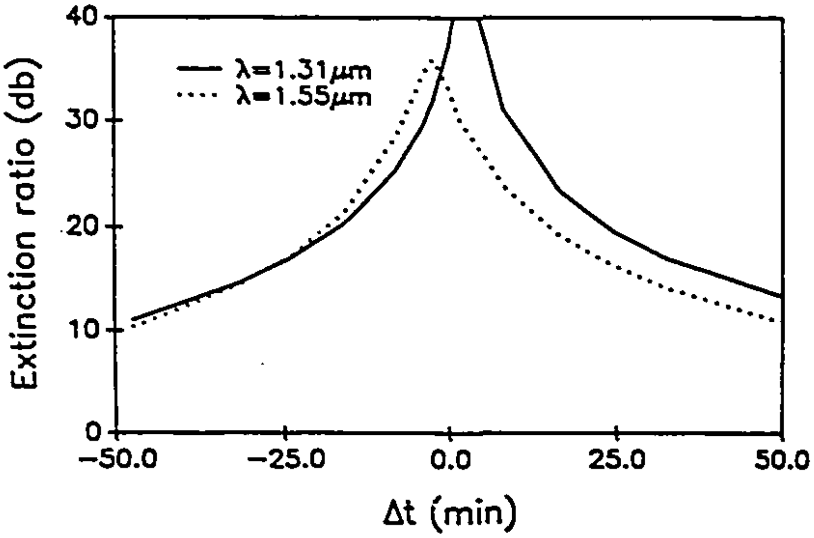

Figure 7.9: Curves of extinction ratio versus the error in diffusion time for device two. The designed ion-exchange time is 431.4 minutes.

The devices are sensitive to an error Δw in the waveguide width as shown in Figs.7.10 and 7.11 for the first and second device, respectively, assuming the same ΔW in both arms. $\Delta W = \pm 0.10\mu$m at $\lambda_1 = 1.31\mu$m and $\pm 0.19\mu$m at $\lambda_1 = 1.55\mu$m for the first device which are about 30 percent larger than those tolerable in X-branch WDM. However, for the second device, the sensitivities, $\Delta W = \pm 0.07\mu$m at $\lambda_2 = 1.31\mu$m in both arms and $= \pm 0.11\mu$m at $\lambda_1 = 1.55\mu$m in both arms. are about the same as those in a X-branch WDM. On the other hand, the reduced extinction ratios due to the fabrication error in width can be improved by adjusting the waveguide depth after the width error is detected. For example, if the width is 0.15μm less than designed and its extinction ratios are 12.26db at $\lambda_2 = 1.31\mu m$ and 16.70db at $\lambda_1 = 1.55\mu m$ for the second device as shown on the left side of the dashed curve in Fig.7.12, both extinction ratios can be increased over 20db by shortening the diffusion time about 30 minutes.

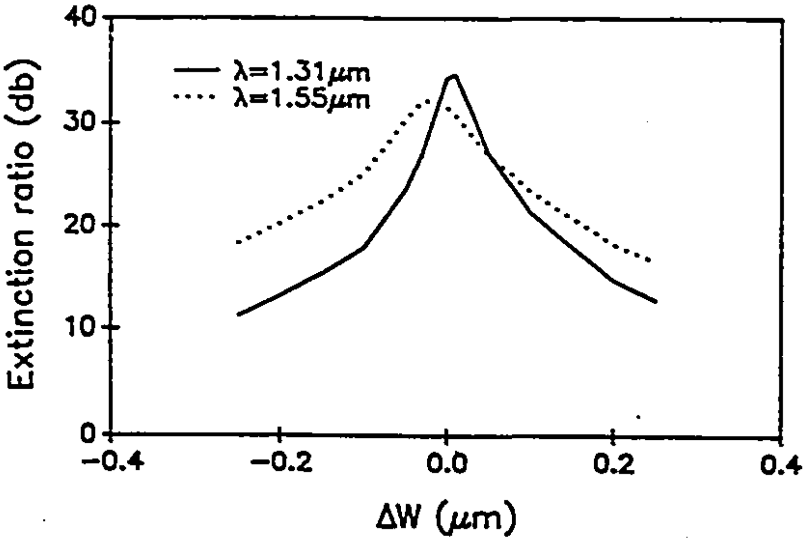

Figure 7.10: Curves of extinction ratio versus the error in waveguide width for device one. The value of ΔW is assumed to be the same for all waveguides in the device.

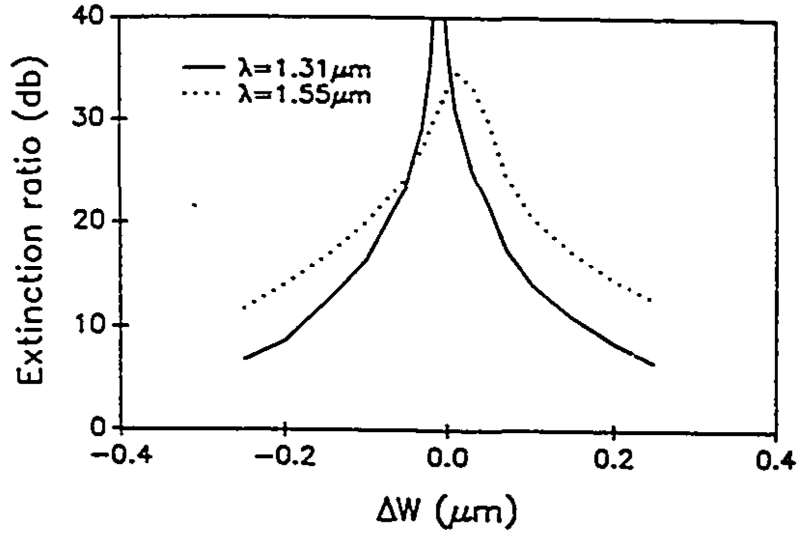

Figure 7.11: Curves of extinction ratio versus the error in waveguide width for device two. The value of ΔW is assumed to be the same for all waveguides in the device.

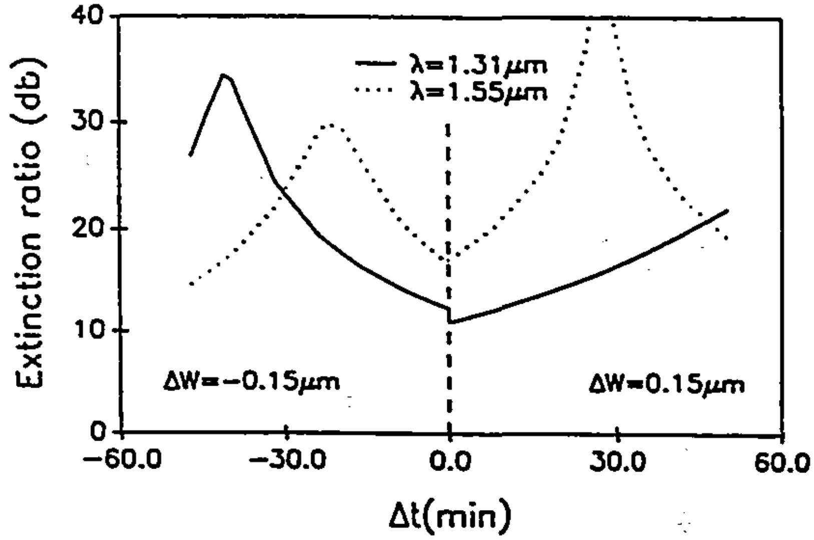

Figure 7.12: Curves of extinction ratio versus the change in diffusion time for device two, when a width error has been detected. Curves on the left side of the dashed line are for ΔW=-0.15μm and those on the right side are for ΔW=0.15μm.

Similar results have also been obtained for the first device. The devices are also tested by BPM simulations for the TE polarization with lower ER's, and found to be polarization dependent due to the birefringence of the K^+ ion-exchanged waveguide in a glass substrate. The optimization for TE operation should be pursued separately.

7.2.3 Discussions

As presented in the previous subsection, the working lengths L (L+l' to be more precise) of waveguide which contribute to the phase delay in arm one are 2430 μm and 1184 μm in the first and second device, respectively. In comparison with that in a X-branch WDM, it is shorter, especially in the second one. A shorter L together with small M and N values (M,N=4-6 in a X-branch WDM [2]) in Eqs.(7.4) and (7.5) are the reasons why the devices reported here have less fabrication sensitivities. The width sensitivity of the second device has not been improved over that of a X-branch WDM because the narrowed waveguide width of arm two increases the sensitivity and weighs against the improvement due to a shorter L and small M and N. The fabrication sensitivities in both the width and depth can be further reduced by increasing the phase delay contribution from ΔL in branch 1 which, however, will increase the device length. If the separation of the output branches is assumed to be $10 \mu m$, the total lengths of the second device presented here, an X-branch WDM [2], and a M-Z WDM without the difference in β between its two arms are about 4mm, 7mm, and 7mm. The new device is almost half of the others in length. Our second device can be further shortened by reducing the width of the second arm if the width sensitivity is not a problem.

7.3 Three-wavelength Mach-Zehnder DM

A third wavelength may also be incorporated into a fiber optical communication system either to increase the capacity or to serve as a pump wave to amplify an existing light wave. Here, we present a Mach-Zehnder type three wavelength DM.

As shown in Fig.7.13, the device consists of two cascaded Mach-Zehnder interferometers. Each Mach-Zehnder interferometer has the same structure as that for two wavelengths. The wavelength $\lambda = 0.98\mu m$ is taken as a third wavelength besides the two wavelengths used in the last section. The three wavelengths are defined in the order of $\lambda_1 = 1.55\mu$m, $\lambda_2 = 1.31\mu$m, and $\lambda_3 = 0.98\mu$m. The first interferometer separates 0.98μm from the other two. The remaining two wavelengths are in turn demultiplexed by the second interferometer which has been discussed in the previous section. To achieve a phase delay in one interferometer arm relative to the other arm, not only the arm-length difference but also the propagation constant difference have been used, which greatly reduces the device length. This phase delay is wavelength dependent. It is designed to be $2M\pi$ at λ_1, $2N\pi$ at λ_2, and $(2K + 1)\pi$ at λ_3 for the first interferometer where M, N, and K are integers.

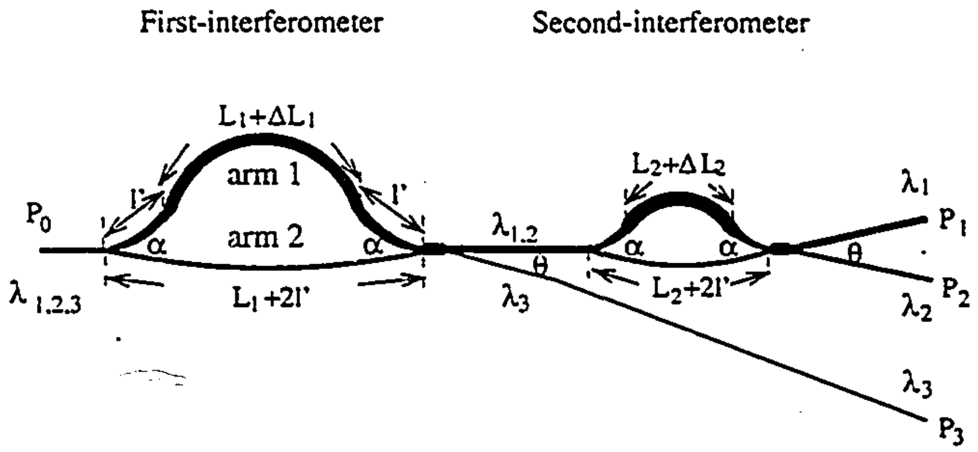

Figure 7.13: Configuration for a three-wavelength Mach-Zehnder DM.

Thus, a second-order mode will be excited at the end of the first interferometer (see Fig.7.14) and enter the narrower branch of the following mode splitter at λ_3. On the other hand, the first-order mode will be excited at the end and enter the wider branch of the mode splitter at both λ_2 and λ_1 (see Fig.7.14). A proper combination of the device parameters, such as the arm lengths, widths, and depth, are chosen to satisfy the phase conditions for each wavelength at the end of each interferometer. The depth of the two interferometers are chosen to be equal so that only one-step waveguide fabrication is needed.

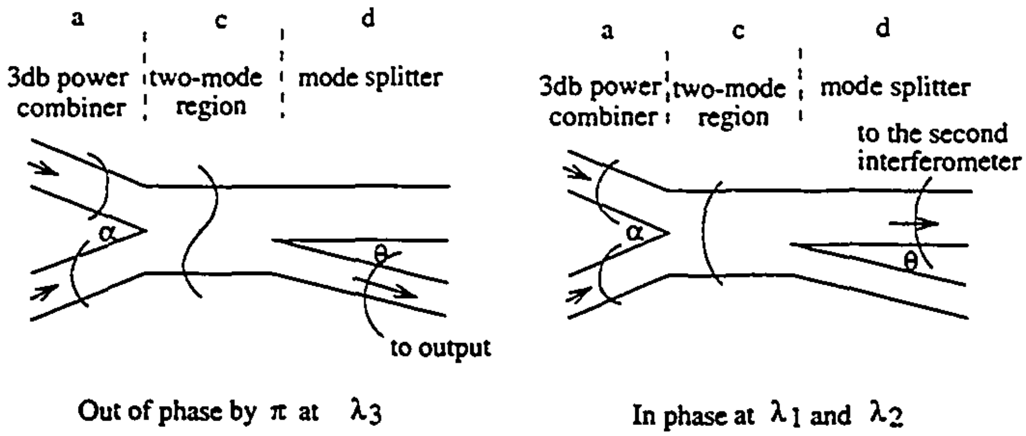

Out of phase by π at λ_3

In phase at λ_1 and λ_2

Figure 7.14: Illustrations of the wave propagation mechanism through the 4-port hybrid coupler in the first interferometer.

7.3.1 Principle of operation

The second interferometer acts as a two-wavelength demultiplexer which has been discussed. Its design is much simpler than the first interferometer and will not be discussed in detail here. The following discussions are mainly for the first interferometer if not indicated as such. The symmetric Y-branch power divider and combiner for both interferometers will not be used. The branches connected to the wider arms start bending and widening right after the branch apexes in both interferometers

As shown in Fig.7.13 for the first interferometer. there are two tapered waveguide with a length l' at the two ends of the first arm which have the same function as we had pointed out for the two-wavelength DM. In this work, $l' = 400\mu m$ is chosen for both interferometers. Assume arm 1 to be wider ($W_{11} > W_{12}$, where the first subscript indicates the order of the interferometer and the second is for the order of the interferometer arm) and longer by ΔL_1 than arm 2. The total relative phase delay in arm 1 compared with arm 2 can be written as

$$\phi(\lambda_i) = (\beta_{i1} - \beta_{i2})L_1 + \beta_{i1}\Delta L_1 + 2l'(\overline{\beta_{i1}} - \beta_{i2}), \quad \text{i=1,2,3} \tag{7.6}$$

where i indicates the order of the wavelength. The output powers can still be expressed by Eqs.(7.2) and (7.3). The phase match conditions for the three wavelengths at the end of the first interferometer are given by

$$\phi(\lambda = \lambda_1) = 2M\pi \tag{7.7}$$

$$\phi(\lambda = \lambda_2) = 2N\pi \tag{7.8}$$

$$\phi(\lambda = \lambda_3) = (2K + 1)\pi \tag{7.9}$$

where $M < N \leq K$ and $M, N, K = 1, 2, \cdots$. Thus, at the shortest wavelength λ_3 (see Eqs.(7.6) and (7.9), since the lights with equal power from the two interferometer arms are out of phase by 180° at the end of the interferometer, a second-order mode will be excited in the junction waveguide of the 4-port hybrid coupler (see Fig.7.14). At the other wavelengths λ_1 and λ_2, since they are in phase (see Eqs.(7.6), (7.7), and (7.8)), a fundamental mode will be excited. L_1 should be kept short to reduce fabrication sensitivities of the device. Eliminating L_1 and ΔL_1 in the three phase conditions together with Eq.(7.6) we have a nonlinear equation given by [Appendix 7.4.1]

$$\frac{n_{11}N\lambda_2 - 2l'n_{11}(\overline{n_{21}} - n_{22}) - n_{21}M\lambda_1 + 2l'n_{21}(\overline{n_{11}} - n_{12})}{n_{11}(n_{21} - n_{22}) - n_{21}(n_{11} - n_{12})}$$

$$- \frac{n_{11}(K + 1/2)\lambda_3 - 2l'n_{11}(\overline{n_{31}} - n_{32}) - n_{31}M\lambda_1 + 2l'n_{31}(\overline{n_{11}} - n_{12})}{n_{11}(n_{31} - n_{32}) - n_{31}(n_{11} - n_{12})} = 0 \quad (7.10)$$

where n_{ij} indicates the arm j's effective index $(\beta_{ij}2\pi/\lambda_i)$ at the i th wavelength. The adjustable parameters in Eq.(7.10) are W_{11}, W_{12}, the waveguide depth D, M, N, and K. The values of M, N, and K are restricted by $M < N \leq K$ for the reason of $\lambda_3 < \lambda_2 < \lambda_1$ and are required to be small for a reasonable device length. Also, some combinations of M, N, and K are beyond the possibility of satisfying Eq.(7.10). There are about only 4 or 5 combinations of M, N, and K values for this example that can be chosen for the design. After M, N, and K are chosen and W_{11} and W_{12} are initially chosen between 3.0μm and 10.0μm ($W_{12} < W_{11}$), D can be solved from Eq.(7.10) by a root-searching technique. ΔL_1 and L_1 can then be found by Eqs.(7.14) and (7.15). The solution may not be proper, such as the device being too long, waveguide too deep, and so on. New branch widths or the M, N, and K combinations have to be tried until a proper solution is reached. For this example, M=3, N=4, K=5, $L_1 = 2800\mu$, $\Delta L_1 = 1.54\mu$m, $D = 4.7\mu$m, $W_{11} = 7.0\mu$m and $W_{12} = 4.0\mu$m.

7.3.2 BPM simulations

The phase delay given in Eq.(7.6) is for straight waveguides. The interferometer arms are curved all the way from beginning to the end of each interferometer. The propagation constant of a straight waveguide is different from that of a curved waveguide. This will result in phase mismatches at the end of each interferometer for the three given wavelengths. The performance of the device can be simulated by the BPM. The effective index method was used to reduce the three dimensional problem into two dimensional problem. The device is also assumed to be made in a glass substrate by a purely thermal K^+ ion-exchange. The glass index is given by n_b=1.5053 at $\lambda = 0.98\mu$m. Fig.7.15 shows a two-dimensional effective index profile of the device with the effective waveguide depth D=4.7μm with t=346 minutes diffusion time.

At the beginning, the simulations of two interferometers were done separately. The phase mismatches are corrected by changing the arm lengths or arm length differences (L_1 or ΔL_1 for the first interferometer) until good results (ER≥25db) for all three wavelengths are achieved. Thus, the new arm length and length difference of the first interferometer are $L_1 = 2864.0\mu$m and $\Delta L_1 = 1.52\mu$m. The bending radius of the first arm R_{11} is 23097.71μm where the first subscript indicates the order of the interferometer and the second is for the arm order (see Fig.7.1). The bending radius of the second arm R_{12} is 104685.71μm.

For the second interferometer, the chosen parameters are D=4.7μm, $L_2 = 1880.0\mu$m, $\Delta L_2 = 0.90\mu$m, $W_{21} = 10.0\mu$m, $W_{22} = 5.5\mu$m, $R_{21} = 19146.14\mu$m, and $R_{22} = 76628.57\mu$m. The branch angles α and θ (see Fig.7.13) are 0.035 rad and 0.005 rad respectively.

The BPM simulations for the whole device are carried out by a more efficient FD-BPM since the length of the whole device is quite long. The results are shown in Figs.7.16, 7.17, and 7.18 for λ_1, λ_2, and λ_3 respectively. The extinction ratios are given in Table 7.1 where P_i, i=1,2, or 3, is the power from the device output branch i as shown in Fig.7.13. The extinction ratios are relative to the power out from the designed output branch. For example, at λ_1, the designed output branch is branch 1 and the extinction ratio is given by

$$ER = 10log_{10}\frac{P_1}{P_i}, \quad \text{i=1, 2, or 3.}$$

The total length of the device is about 1.5cm which is relatively shorter than a directional-coupler version 1.8-2.0cm in [7]. Again, the device for TE polarization has to be pursued separately.

db	P_1	P_2	P_3
λ_1	0	> 30	28
λ_2	27	0	25
λ_3	> 30	29	0

Table 7.1: Extinction ratios

7.3.3 Discussions

Here, we have presented a three-wavelength Mach-Zehnder wavelength demultiplexer. The device concept has been demonstrated by BPM simulations. The device can be made by using only one photo-mask and by a single-step waveguide fabrication. It can provide high extinction ratios for all three wavelengths and can also be relatively shorter than a directional-coupler version. The work presented here is only preliminary. It can be further improved and its feasibility should be tested out by experiements.

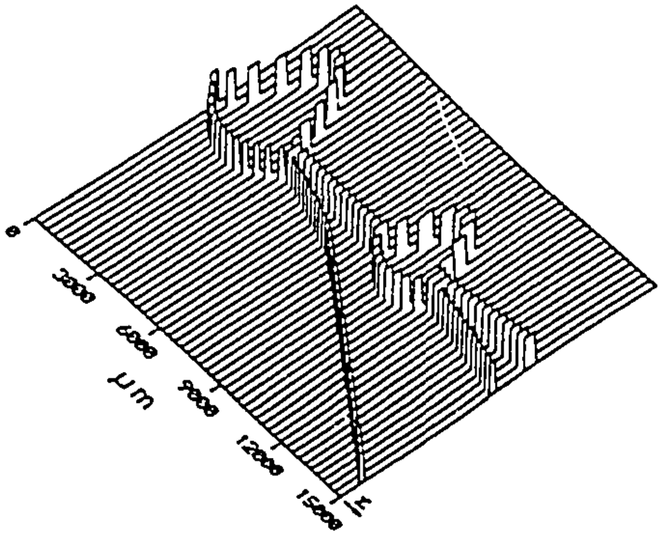

Figure 7.15: The device's lateral effective index profile used for BPM simulation.

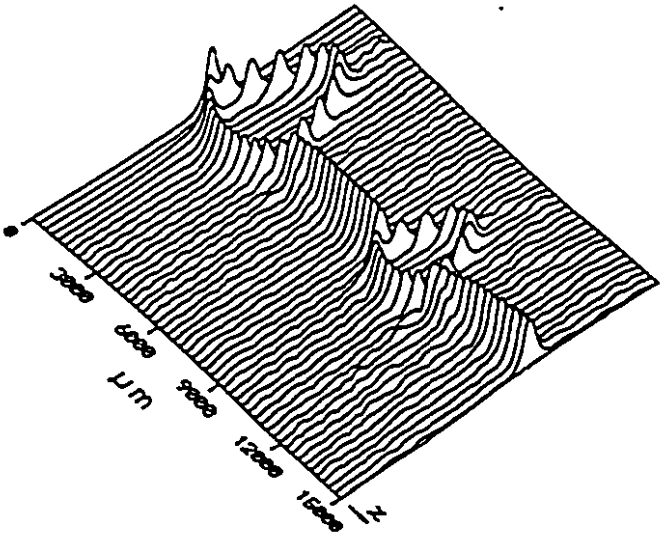

Figure 7.16: BPM simulation of the whole device for $\lambda_1 = 1.55\mu$m.

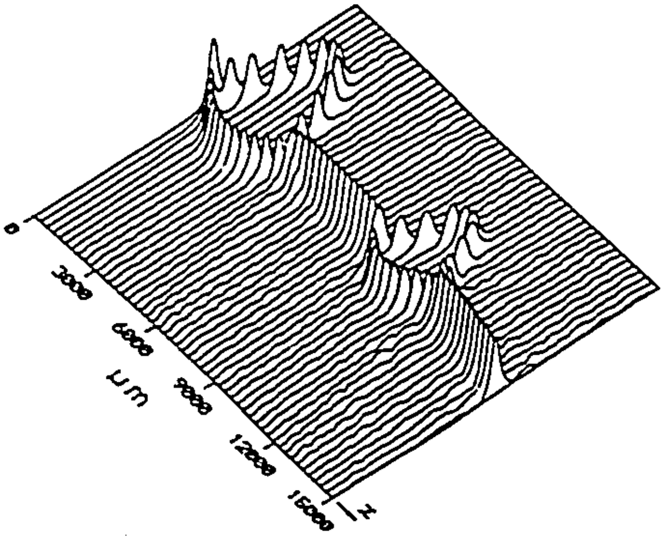

Figure 7.17: BPM simulation of the whole device for $\lambda_2 = 1.31\mu m$.

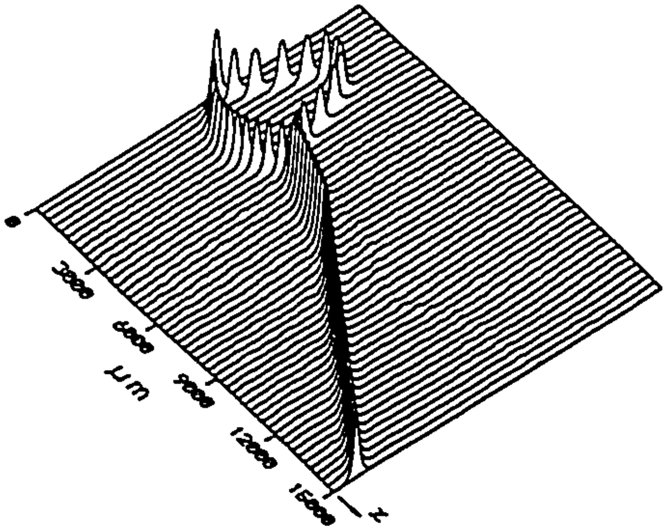

Figure 7.18: BPM simulation of the whole device for $\lambda_3 = 0.98\mu m$.

7.4 Appendix

7.4.1 Derivation of Eq.(7.10)

Substituting the equations of (7.6) at λ_1, λ_2, and λ_3 into Eqs.(7.7), (7.8), and (7.9) respectively, we have the following equations

$$\begin{aligned}(n_{11} - n_{12})L_1 + n_{11}\Delta L_1 + 2l'(\overline{n_{11}} - n_{12}) &= \lambda_1 M &(7.11)\\ (n_{21} - n_{22})L_1 + n_{21}\Delta L_1 + 2l'(\overline{n_{21}} - n_{22}) &= \lambda_2 N &(7.12)\\ (n_{31} - n_{32})L_1 + n_{31}\Delta L_1 + 2l'(\overline{n_{31}} - n_{32}) &= \lambda_3(K + 1/2). &(7.13)\end{aligned}$$

ΔL_1 is then solved from Eq.(7.11) given by

$$\Delta L_1 = [\lambda_1 M - (n_{11} - n_{12})L_1 - 2l'(\overline{n_{11}} - n_{12})]/n_{11}. \qquad (7.14)$$

By substitution of ΔL_1 in both Eq.(7.12) and (7.13) by Eq.(7.14), we can solve L from both the equations which are given by

$$L = \frac{n_{11}N\lambda_2 - 2l'n_{11}(\overline{n_{21}} - n_{22}) - n_{21}M\lambda_1 + 2l'n_{21}(\overline{n_{11}} - n_{12})}{n_{11}(n_{21} - n_{22}) - n_{21}(n_{11} - n_{12})} \qquad (7.15)$$

and

$$L = \frac{n_{11}(K + 1/2)\lambda_3 - 2l'n_{11}(\overline{n_{31}} - n_{32}) - n_{31}M\lambda_1 + 2l'n_{31}(\overline{n_{11}} - n_{12})}{n_{11}(n_{31} - n_{32}) - n_{31}(n_{11} - n_{12})}, \qquad (7.16)$$

respectively. Thus, equating the above two equations leads to Eq.(7.10).

Bibliography

[1] A. Neyer, "Guided-wave devices based on two-mode interference", SPIE Proceedings, vol. 993, pp.68-75, Sept., 1988.

[2] G.L. Yip and L.J. Babin, "BPM design of a widened X-branch demultiplexer in a glass sustrate by K^+ ion exchange for $\lambda = 1.31\mu m$ and $\lambda = 1.55\mu m$", IEEE-OSA Integrated Photonics Research Proceedings, vol. 10, pp.72-75, March, 1993.

[3] H.C. Cheng and R.V. Ramaswamy, "Symmetric directional coupler as a wavelength multiplexer-demultiplexer: theory and experiement", IEEE J. of Quantum Electron., vol.QE-27, No.3, pp.567-574, 1991.

[4] A. Tervonen, P. Poyhonen, S. Honkanen, and M. Tahkokorpi, "A guided-wave Mach-Zehnder interferometer structure for wavelength multiplexer", IEEE Photonics Tech. Let., vol.3, No.6, pp.516-518, 1991.

[5] G.L. Yip, K. Kishioka, F. Xiang, and J.Y. Chen, "Characterization of planar optical waveguides by K^+-ion exchange in glass at 1.152 and 1.523 μm", SPIE Proceedings, vol.1583, pp.14-18, Sept., 1991.

[6] G. L. Yip and J. Albert, "Characterization of planar optical waveguides by K^+-ion exchange in glass", Opt. Lett., vol. 10, no.3, pp. 151-152, 1985.

[7] K. Kishioka and G.L. Yip, "A novel Three-wavelength demultiplexer utilizing the two- and three-guide couplers", IEEE J. Lightwave Technol., vol. LT-11, no.2, pp. 234-240, 1993.

Chapter 8

Conclusions

The goal of this thesis has been to investigate the design and fabrication of the optical wavelength multi/demultiplexers made by ion-exchange in glass substrate. The two main wavelengths to be demultiplexed are 1.31 and 1.55 μm. Since the glass fibers are of the lowest loss at these two wavelengths, most of optical communication systems based on single-mode fibers are now working at these two wavelengths. A wavelength multi/demultiplexer for these two wavelengths allows a single-mode fiber communication system to be able to work at both the wavelengths simultaneously, and hence, increases the system capacity.

The devices' structures are mainly based on the Y-branch mode splitter. The principle of the Y-branch mode splitter has been discussed in Chapter 3. The key requirements of a Y-branch mode splitter are a small branch angle and a large asymmetry of the two branches. The results were confirmed later on by BPM simulations in Chapter 5.

Starting from the wave equation, the WKB method, modified WKB method, BPM, FD-BPM, and effective-index method were presented in Chapter 2. They cover all the necessary numerical methods for the device simulation and design.

A newly developed multi-sheet Brewster angle substrate index measurement method together with the index values at infrared wavelengths were presented in Chapter 4. The method has been proved to be simple and relatively accurate. Based on the measured results, the dispersion of a soda-lime glass has been found quite similar to a BK7 glass at wavelengths of interest here. The study of Al_2O_3 sputtering, Al_2O_3 cladded waveguide properties, and the refractive index of the cladding layer has been conducted in detail. The results show that the substrate surface will be damaged if the sputtering power is high. Without annealing the sample after sputtering, the Al_2O_3 cladded layer can be used as a waveguide only when the sputtering power is less than a certain value. Its refractive index is approxmately proportional to the sputtering power. However, the index value is very large compared with the glass index even when the sputtering power is low enough to allow the cladding layer to guide light with an insignificant loss. Waveguide characterizations were also carried out before the design and fabrication at the infrared wavelengths for both K^+ ion-exchange and Ag^+ ion-exchange. The surface index changes for both the ion-exchanges at the infrared wavelengths basically agree with those at $\lambda = 0.6328\mu m$ reported earlier. At the infrared wavelengths, it was found that the Gaussian profile is the best fit to a K^+ ion-exchanged waveguide, while the second-order polynomial the best fit to a Ag^+ ion-exchanged waveguide.

With all the necessary data made available, the design and fabrication of the devices were carried out as discussed in the following chapters. The first device studied is the Y-branch made by K^+ ion-exchange with one branch loaded by an Al_2O_3 cladding strip. According to the BPM simulations of the device, the input power has a tendency to stay in branch 1 at the output if the out-ward bending angles of both the branches are the same with respect to the input branch. As a result, the ER at λ_1 is always higher than that at λ_2 if their effective index differences $\Delta n_{e1,2}$ are equal. To balance their ER values, branch 2 was straightened in line with the input branch (branch 0) so that the input power can be more easily coupled into branch 2 which has a much shallower waveguide depth compared with that of branch 0 or 1. The BPM simulations show that the branch angle has to be at most 0.008rad or less to have the ER values over 20db at both wavelengths. Consequently, $\theta = 0.005$ rad was chosen as the branch angle of the device. Once the branch angle is fixed, the performance of this DM device is mostly dependent on the effective-index differences between the two infinitly separated branches. Usually, the higher the value of the difference, the higher the ER. Again based on the BPM simulations, two criteria of the effective-index difference for two wavelengths ($\Delta n_{e1} > 0.00033$ and $\Delta n_{e2} > 0.00057$) were established for getting the ER values over 20db, which are roughly independent of other parameters such as the waveguide widths, depths, and the cladding thicknesses. The effective-index differences between the two branches were then calculated for the devices with combinations of different waveguide widths, depths, and cladding thicknesses. Based on these two criteria, the device with certain combinations of waveguide parameters can be determined whether it has ERs over 20db. The device optimization was then carried out to obtain the maximum fabrication tolerances for those three parameters. The device was found to be not very sensitive to the waveguide widths and depths. However, it is very sensitive to the cladding thickness which is about $\Delta f \leq \pm 0.01 \mu m$.

In the initial fabrication process, the same Al-mask used for the second K^+ ion-exchange was used again to form the Al_2O_3 sputtered strip. Little power was observed from the Al_2O_3 cladded branch at the device output. The Al_2O_3 cladded waveguide was very lossy. We believe that there were two main reasons responsible for the Al_2O_3 cladded waveguide's high loss. One was the strip edge scattering loss due to the edge roughness caused by wet-etching of Al-mask window edges. The other was the surface damage of the K^+ ion-exchanged waveguide due to the bombardment of Al_2O_3 molecules with high power during sputtering. Besides the high loss, the sputtered Al_2O_3 thickness was also less than what it was designed for, which may be the other reason that little power came out from branch 2 at λ_2. In the last process of etching the Al-mask after the sputtering, the etching solution also dissolved Al_2O_3 to a certain extent if the cladding did not have any protection. although the etching was much slower than that done to Al.

To reduce the surface damage, low sputtering power was used instead of annealing the device at a high temperature after the sputtering because a high temperature would anneal the K^+ ion-exchanged waveguides also. To reduce the rough edge scattering loss, a third photo-mask was introduced to perform the Al_2O_3 sputtering. This third photo-mask was a negative of the second photo-mask but with the window width twice as wide as W_2. Thus, the rough strip edges were far away from the center of light wave in the waveguide. As a result, the light intensity has much decayed when it reached the edges with little power left to be scattered. A fourth photo-mask was needed to coat a photoresist layer on the top of the Al_2O_3 strip to prevent it from being etched. This mask should be the negative of the third mask. The performance of the device made through the modified fabrication process has been much improved. The loss in the Al_2O_3 cladded waveguide has been much reduced. The measured ERs are about 20db at both the wavelengths. Further improvements can be expected if the branch angle is reduced according to the BPM results already discussed in Chapter 5.

The second device investigated is similar to the first one but with its branch 2 made by Ag^+ ion-exchange and without a cladding strip. Ag^+ ion-exchange can provide a higher surface index change (up to 0.09) which is high enough to produce a large branch asymmetry for the demultiplexing. With no cladding strip, the fabrication process can be simplified although another additional anodization process is necessary. The depth D_2 of Ag^+ ion-exchange branch two is the most sensitive parameter. The design optimization was mainly carried out by chosing $AgNO_3$ dilution and Ag^+ ion-exchange waveguide depth to maximize the fabrication tolerance of D_2. The initial testing result shows that the Al-mask is not suitable for making a Ag^+ ion-exchanged channel waveguide due to the existance of a chemical potential between Al and Ag^+, which tends to drive Ag^+ to the underside of the Al-mask. To overcome this, the Al-mask was anodized before the Ag^+ ion-exchange. This turned out to be working well. The experimental results have demonstrated that the device works well. Increasing the surface index change in the Ag^+ ion-exchanged waveguide and reducing the branch angle are two possible options if higher ER values are required.

Since birefringence exists in K^+ ion-exchanged glass waveguides but the sputtered Al_2O_3 cladding and Ag^+ ion-exchanged waveguide are isotropic, the optimization obtained in a design for one polarization will be destroyed for another polarization since the dispersion curves of the two branches are different for the two polarizations. The devices we have studied employing K^+ ion-exchange are polarization dependent. It is possible that the Y-branch WDM can be polarization independent if the birefringence in a K^+ ion-exchanged waveguide can be eliminated.

As we have discussed in Chapter 3 and 5, in order to make the above two devices work as WDMs, the branch angle has to be very small, the branch strongly asymmetric, and also the two dispersion curves of the two independent branches should intersect at a wavelength (λ_0) between the two wavelengths demulutiplexed. This wavelength divides two wavelength regions, one is shorter and the other is longer. The input light with the shorter wavelength ($< \lambda_0$) will have most of its power guided into one branch (branch 2 in this work) but the light at the longer wavelength ($> \lambda_0$) will be guided into the other branch (branch 1 in this work). Thus, as we can see, the device can demultiplex two groups of input wavelengths which is quite a unique property.

To simplify the fabrication further, we proposed DM devices formed by Mach-

Zehnder interferometers and Y-branch mode splitters in Chapter 7. It was the first time, to our knowledge, that a width difference between two interferometer arms is used to provide a phase delay at the end of the interferometer. It adds another adjustable value for the device optimizatoin and makes the device workable for a three-wavelength DM. The BPM simulations show that the devices, either two-wavelength or three-wavelength, work well under the assumptions made in the computations. Since phase matching in interferometer is the key working condition of the device, the Mach-Zehnder interferometer considered here is polarization dependent.

The work done covers only a small part of the WDM and has been pursued only to a limited depth. The devices studied and fabricated here are not perfect yet. There is room for the further improvement. Those devices, nevertheless, have their unique and interesting properties which should make them very attractive for applications in single-mode fiber communication systems in the near future.